MAREES TERRESTRES

BULLETIN D'INFORMATIONS

INTERNATIONAL CENTER FOR EARTH TIDES
CENTRE INTERNATIONAL DES MAREES TERRESTRES

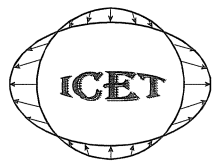

Federation of Astronomical and Geophysical Data Analysis Services
(FAGS)

International Association of Geodesy - International Gravity Field Service
(IAG – IGFS)

Publié avec le soutien de l'Observatoire Royal de Belgique

BIM
1 4 1

15 AOÛT 2006

Editeur: Dr. Bernard DUCARME
Observatoire Royal de Belgique
Avenue Circulaire 3
B-1180 Bruxelles

BIM 141
15 août 2006

Workshop

on

Analysis of Data from Superconducting Gravimeters and Deformation Observations regarding Geodynamic Signals and Environmental Influences

The workshop which took place in Jena (Germany) end of March 2006 brought together different scientific groups that are closely related. The meeting was within the new framework of the IAG, covering IC-P3 (GGP) which is an inter-commission project of Commission 2 (Gravity Field) and Commission 3 (Earth Rotation and Geodynamics), and WG 3.1.3, a special study group under the Earth Tide Subcommission 3.1 dealing with the 'Analysis of Environmental Data for the Interpretation of Gravity Measurements'. Additionally a meeting of the new working group on 'High precision Tidal Prediction' and a GGP business meeting were held. Altogether 37 scientists from 17 countries participated, 45 papers were presented. Topics of the workshop were

- precise computation of earth tides and ocean loading for different geodynamic components;
- presentation of new analysis techniques, observatories, and instruments;
- effects on air pressure variations on gravity and their reduction;
- hydrological signals in gravity;
- application of geodynamic observations to hydrology;
- combination of gravity observations derived from different instrumentations;
- application of gravity and deformation observations to the monitoring of dynamic processes and the study of properties of the earth's body.

Details of the GGP business meeting can be found in the GGP Newsletter #17. Part of the workshop was also a visit to the Geodynamic Observatory Moxa which is located 30 km south of Jena.

Papers related to the presentations given during the workshop as well as some of the abstracts (in place of full papers) are published in this and the next issue of the 'Bulletin d'Information des Marées Terrestres'. ICET has kindly agreed to let their journal once again be the forum in which to publish the proceedings of a 'Jena' workshop.

Finally on behalf of the local organizing committee I would like to thank all participants for coming to Jena and also many thanks for their commitment which resulted in a very productive meeting. It was a pleasure to have you all in Jena and we would be pleased to have you back. A good opportunity for this will be the next Earth Tide Symposium, which will be held in Jena, September 1-5, 2008.

Corinna Kroner, Gerhard Jentzsch

Comparison of some tidal prediction programs and accuracy assessment of tidal gravity predictions

B. Ducarme

Research Associate NFSR, Royal Observatory of Belgium, Av. Circulaire 3, B-1180Brussels, Belgium

1. Introduction

The strongest precision requirements concerns tidal gravity prediction. It is a reason why we shall investigate this tidal component. The comparison work is not exhaustive as we did not include the VAV (Venedikov and Vieira, 2004) or the BAYTAP-G (Tamura et al., 1991) approaches.

Two main approaches will be compared here:

- PREDICT (Wenzel, 1996) and T-soft (Van Camp and Vauterin, 2005);
- MT80w and MT80Tw (ICET, http://www.astro.oma.be/ICET/).

We shall follow the different steps required to obtain an accurate gravity tides prediction from the simple case of the astronomical tides to the tides on the real Earth

The accuracy of the tidal prediction will depend on the number of terms used in the Tidal Potential development. We shall see that other refinements are also required.

The tidal potential development have been computed with an increasing complexity: Doodson (1921) 378 terms, Cartwright-Edden (CTE505, 1973) 505 terms, Buellesfeld (1985) 656 terms, Tamura (TAM1200, 1987) 1,200 terms, Xi-Qin-Wen (1989) 2,933 terms, Roosbeek (1996) 6,499 terms and Hartmann-Wenzel (HW95, 1995) 12,935 terms. Recently Kudryatsev (2004) proposed a tidal potential development KSM03 with 28,806 terms.

PREDICT is the most versatile application and can use all the existing tidal potentials from Doodson up to Hartmann-Wenzel HW95. T-soft uses the same programming as PREDICT but is restricted to the TAM1200 tidal potential.

The MT80w is restricted to the CTE505 potential and MT80Tw can use TAM1200 and CTE505.

We shall compare the results of the different software for the station Hannover (λ=9°.7144E, φ= 52°.3868N, h=110m) during the year 1990. The peak to peak amplitude of the gravity tides reaches 2,200nms^{-2}. We shall call it the "tidal range" (TR)

To compare different tidal predictions we generally fit a linear regression between the results to obtain a scale factor and a RMS error. We can also give the range of the differences.

2. The astronomical tides

The first step is the precise evaluation of the direct influence of the Moon, the Sun and the planets, generally called the "astronomical tides". It is based on the developments of the tidal potential (Melchior, 1978). To derive a tidal prediction we have to consider a scale factor often referred as "Doodson" constant, a geometrical part depending on the position at the surface of the Earth (geodetic coefficients), which is different for each tidal component, and the harmonic part, which is a sum of sinusoidal terms. The development of the tidal potential provides for each term a normalised amplitude and an argument which is a linear combination of the astronomical arguments of the celestial bodies.

Only 6 arguments are required for the Luni-solar tides. The fundamental variables chosen by Doodson are

$\dot{\tau}$ = 14.49205 (period of 24h50m) for the mean lunar time τ

The orbital motion of the Moon requires 3 supplementary variables i.e.

$\dot{s}$ = 0.544902 (period of 27.321 days) s defines the position of the Moon on its orbit. It corresponds to the variation of the declination of the Moon (tropic month)
$\dot{p}$ = 0.00464 (period of 8.847 years) associated to the revolution of the mean lunar perigee.
$\dot{N}$ = (period of 18.613 years) corresponding to the retrograde revolution of the lunar node.

As the mean solar and lunar times (t et τ) are linked to the sidereal time t' by the relation

$\dot{t}' = \dot{t} + \dot{h} = \dot{\tau} + \dot{s}$
The solar terms will be expressed through the relation $\dot{t} = \dot{\tau} + \dot{s} - \dot{h}$

The apparent motion of the Sun is expressed by
$\dot{h}$ = (period of 365.25 days) tropic year
$\dot{p}_s$ = (20,940 years) period of rotation of the perihelion of the terrestrial orbit.

The Doodson variables are expressed as polynomial functions of the elapsed time, expressed in fraction of Julian century, since an initial epoch which is now J2000.0 corresponding to "Julian" date 2451545.0. The moment of the tidal prediction is thus converted in fraction of julian century since J2000.0. The amplitude of the main tidal terms is also changing slowly with time and since Tamura the main tidal constituents are given with a linear trend.
Some care should be taken when computing the Doodson arguments.
τ is not directly accessible but is computed by the relation
$\tau = 15°.t + \alpha_m - s + \lambda$
where t is the hour in UT and α_m is the right ascension of an fictitious object defining UT, and λ the longitude. The tidal prediction is thus expressed in UT at the point of longitude λ.
α_m replaces h because we want to use the "true" position of Moon and Sun and not the "apparent" one when we compute the hour angle $\alpha - \alpha_m$ of a celestial body of right ascension α.
We consider thus that the gravitational attraction is acting instantaneously. The difference corresponds to the aberration term of 20".5 i.e. a phase shift of 0°.01 for the semi-diurnal waves or, at mid latitude, a global error that can reach 0.25nms^{-2} or 10^{-4} of the tidal amplitude.
One should use the dynamical time t_D, which is a linear time scale, in all arguments except α_m where the universal time t_u is used.
The universal time t_u is not a linear time scale and in practice one uses the UTC which is a linear time scale periodically readjusted on t_u.
The difference between t_d and UTC is given by an initial offset plus the sum of all the "leap" seconds applied to UTC since its instauration.
In the equation of τ we have still to correct t for the residual difference between t_u and UTC as the leap second jumps are already taken into account in α_m. This correction is always smaller than one second and will also affect the tidal prediction at the 10^{-4} level.
Concerning the planetary influences, Tamura was the first to introduce tidal terms coming from Jupiter and Venus.
Roosbeek and Hartmann-Wenzel introduced additional arguments for Mars, Mercury and Saturn to arrive to a total of 11 astronomic elements.

2.1 The planetary terms in Tamura and Wenzel

A direct comparison of the Tamura's formula with Wenzel ones for the planetary terms is not easy as the two authors are not using the same arguments to define the Jupiter and Venus positions.
Tamura argument f_7 is referring to Jupiter's opposition and f_8 to Venus superior conjunction.

Wenzel argument k_{10} is the mean longitude of Jupiter and k_8 the mean longitude of Venus. It is easy to convert from one system to the other as

$$f_8 = 180° - (h - k_8)$$

and

$$f_7 = h - k_{10}$$

where h is the mean longitude of the sun.
For Jupiter there is no difficulty but there is a contradiction for Venus

From the first order expression in PREDICT with origin in JD 2451545.0

$h = 280°.47 + 360007.70*DTM$
$k_8 = 181°.98 + 585192.13*DTM$
we get
$f_8 = 81°.51 + 225184.4*DTM$

In Tamura, 1987 we have

$f_8 = 81°.5 + 22518.44*TD$
with DTM=TD/10
We see that at the first order in TD the definition is identical. It should be noted that an initial phase of 180° is equivalent to a change of sign of the term. It will matter only for terms where the argument k_8 is multiplied by an odd number. Among the few terms generated from Venus only term 984 has an odd argument (-1) for k_8. Its sign should be changed with respect to original Tamura work, when the program PREDICT is used (Ducarme and Xi, 2006).

2.2 Intercomparison of the softwares with a same tidal development

Comparison of PREDICT and MT80Tw with TAM1200:
extrema $-0.01/+0.02 nms^{-2}$ ($< 10^{-5}$ TR)
scale factor 0.9999869
RMS error $0.0028 nms^{-2}$

Comparison PREDICT and MT80Tw with CTE505
extrema $-0.15/+0.2 nms^{-2}$ ($< 10^{-4}$ TR)
scale factor 0.9998970
RMS error $0.0487 nms^{-2}$

Comparison PREDICT and MT80w with CTE505
extrema $-0.2/+0.4 nms^{-2}$ ($< 210^{-4}$ TR)
scale factor 1.0000030
RMS error 0.1610 nms^{-2}

2.3 Intercomparison of the tidal developments for a same software

Comparison of HW95 and TAM1200 with PREDICT:
Extrema $-0.4/+0.4 nms^{-2}$ ($< 210^{-4}$ TR)
scale factor 1.0000044
RMS error $0.0799 nms^{-2}$

Comparison of TAM1200 and CTE505 with MT80Tw
Extrema $-1.5/+1.5 nms^{-2}$ ($<7.10^{-4}$ TR)
scale factor 0.9996702
RMS error 0.3347 nms^{-2}

2.4 Conclusions

The programming with TAM1200 is perfectly equivalent in PREDICT and MT80Tw. Even the old versionMT80w referred to J1900.0 is still valid to much better than 10^{-3}TR.
If we consider that HW95 is the most precise tidal development we see clearly the reduction of the precision with TAM1200 at the level of 2.10^{-4}TR (0.5nm/s^2) and CTE505 at the level of 7.10^{-4} TR (1.5nm/s^2).
The choice of the software and tidal development will thus depend of the required precision of the tidal gravity prediction around 10nms^{-2} for field work and better than 1nms^{-2} for absolute gravity measurements, for which special attention has to be paid to the LP part of the spectrum which can easily produce systematic errors. On the contrary for field differential measurements LP tides will cancel.

3. Elastic response of the Earth (the Earth tides)

Astronomical tides are only valid for a rigid Earth. For an elastic Earth it is necessary to take into account the deformation of the Earth and the additional change of potential induced by this deformation. For tidal gravity predictions this amplitude factor is called δ. The rigid Earth corresponds to $\delta = 1$. The computations are made under the assumption that all the waves inside a tidal "group" have one and the same δ factor. Tidal groups are formed by the waves in the vicinity of the main tidal constituents. The number and the limits of the groups are quite arbitrary for tidal prediction but for tidal analysis the Rayleigh criterion of commensurability of the periods on the time interval covered by the data set put constrains on the number of groups that one can consider.
The fundamental tidal potential W_2 is an harmonic function of degree 2. Doodson introduced already terms deriving from W_3 and since Tamura the potential W_4 is included. Each potential of degree n produces terms of order k with $0 \leq k \leq n$. The order fixes the frequency of the corresponding harmonic terms i.e. the tidal "families": 0 (LP), 1 (D), 2 (SD), 3 (TD), 4 (QT),....As a consequence in the LP tides one can find terms coming from W_2^0 , W_3^0 , W_4^0 ,... and in the ter-diurnal band terms from W_3^3 , W_4^3 ,...
As the Earth response will be different for each degree and order, it will be necessary to carefully separate the different degrees in each tidal family.
Finally attention should be paid to the fact that in the diurnal band the elastic response is not constant but that there exists a resonance, due to the liquid core (NDFW), close to the sidereal frequency, corresponding to wave K_1. For gravity the response is diminished of 2% for K_1 and increased by 10% on ψ_1. This fact is indeed included in the models.
Finally there is a permanent tide called M_0S_0 which requires a specific treatment. Tidal gravity corrections should apply the so called "zero tide" convention defined by IAG. It means that we can only correct the corresponding astronomical tide by applying a tidal factor equal to 1. This is automatically the case for the MT80 programs but for PREDICT and T-soft it is necessary to define a special tidal group M_0S_0 with $\delta = 1$
We shall investigate three questions:

- discrepancies between the different elastic models;
- influence of the LP, D and SD terms associated with W_3 and W_4;
- liquid core resonance

3.1 Comparison of the Earth response models

PREDICT is using latitude dependent tidal parameters for an elliptical, rotating, inelastic and oceanless Earth computed from the Wahr-Dehant-Zschau model (Dehant, 1987).

MT80Tw can be used with the model DPREMZ, Wahr-Dehant-Zschau, Dehant, 1987) and the DDW, Dehant-Defraigne-Wahr (Dehant et al., 1999) models, either hydrostatic (HYDR) or non-hydrostatic and inelastic(NHYDR).
The comparisons are made with the TAM1200 potential.

Comparison of NHYDR and HYDR:

Extrema $-2./+1.\text{nms}^{-2}$ ($< 10^{-3}$ TR)
scale factor 1.0015464
RMS error 0.1718

Comparison of NHYDR and DPREMZ

Extrema $-2./+1.\text{nms}^{-2}$ ($< 10^{-3}$ TR)
scale factor 1.0014897
RMS error 0.202

Comparison of DPREMZ and HYDR

Extrema $-0.3./+0.4\text{nms}^{-2}$ ($< 210^{-4}$ TR)
scale factor 1.0000565
RMS error 0.1156

The fit shows that the model NONHYDR differs significantly from the two others at the level of 0.15%. After the fit the discrepancies are reduced to $-0.5/+0.5\text{nms}^{-2}$. HYDR and DPREMZ are very close except for the LP tides , with $\delta = 1.157$ for HYDR and $\delta = 1.154$ for DPREMZ.

3.2 Treatment of W_3^k ($0 \leq k < 2$) and W_4^J ($0 \leq j < 3$) terms

These terms are very weak and, except for W_4^3, are mixed up inside the main LP, D and SD groups. However their amplitude factors differ systematically from these of the W_2 potential: $\delta_2 \cong 1.155$ (LP), 1.15 (D) outside the resonance or 1.16 (SD) while $\delta_3 \cong 1.07$ $\delta_4 \cong 1.04$.
The W_4^3 terms will appear kept inside the ter-diurnal family.
To take into account this systematic difference it is conventionally accepted to multiply these terms by the ratio δ_3/δ_2 or δ_4/δ_2 between the tidal factor corresponding to their harmonic degree and the tidal factor corresponding to the main wave of their group. For what concerns the elastic response of the Earth this procedure is indeed perfectly correct.
Neglecting this correction will introduce systematic effects at the level of $\pm 1.\text{nms}^{-2}$ ($0.5\ 10^{-3}$ TR) and a RMS error of 0.61nms^{-2}.
Due to oceanic loading the problem of the LP, D and SD terms deriving from W_3 and W_4, becomes also more complicated. The oceanic loading effects are much lower on these constituents than on the tides excited by W_2. The analysis of the terms generated by W_3^1 and W_3^2 performed on the long records of superconducting gravimeters provided amplitude factors close to 1.07 and very small phase differences. Using as reference the modeled tidal factors δ_m, it is thus more correct to multiply the terms coming from $W_{3,4}^1$ and $W_{3,4}^2$ by $\delta_{3,4}/\delta_m$. If observed tidal factors are available it is necessary to check how they were obtained. Most of the tidal analysis programs include a correction of the terms generated by W_3^1 and W_3^2. Their amplitude in the tidal potential is multiplied by the ratio δ_3/δ_2 or δ_4/δ_2. It is thus better to use the same normalization in the tidal prediction. A more correct procedure, used in the program VAV, is to treat these terms as a separate group mixed up inside the wave groups generated by W_2^1 or W_2^2. Then the observed tidal factors δ_{obs} are free from any influence of the $W_{3,4}$ terms and it is better to apply in the tidal prediction the ratio $\delta_{3,4}/\delta_{obs}$ to the terms coming from $W_{3,4}^1$ and $W_{3,4}^2$.

For example a difference of 20% on the tidal amplitude factor of the SD waves used as reference to normalize the $W_{3,4}^{1,2}$ will produce a peak to peak difference of 2.10^{-4}TR ($0.4 nms^{-2}$).

3.2 Influence of the NDFW in the diurnal band

The liquid core resonance is taken into account in the different models of the Earth response to the tidal forces, but with slightly different resonance parameters. It is concentrated on π_1, P_1, K_1 on one side of the resonance and ψ_1 and φ_1 on the other one. K_1 amplitude factor is reduced of 2% and ψ_1 is amplified of 10%.
As a first comparison one can enter the same model $\delta = 1$ on all the waves
Comparison of PREDICT and MT80Tw:

Extrema $-0.1/+0.1 nms^{-2}$ ($< 0.5\ 10^{-4}$ TR)
scale factor 0.9999269
RMS error 0.0518

The differences are concentrated around ψ_1 and are due to the fact that a different ratio $\delta_{TD}/\ \delta_D$ is used in PREDICT and MT80Tw.
However generally for a tidal prediction we have only parameters for the main tidal groups i.e Q_1, O_1, P_1, K_1, N_2, M_2, S_2, K_2. In this case ψ_1 and φ_1 are mixed up with K_1 and will receive the same tidal parameters as the main wave of this group. However due to the resonance the effective amplitude factor of ψ_1 is higher by more than 10% and 3% for φ_1. It is thus useful to introduce the resonance by multiplying the amplitude inside by the theoretical resonance factors $\delta_{\psi 1}/\delta_{K1}$ or $\delta_{\varphi 1}/\delta_{K1}$. This correction is effectively implemented in PREDICT, T-soft and MT80Tw. Neglecting this correction will produce residues at the level of $\pm 0.6 nms^{-2}$ (3.10^{-4}TD) and a RMS error of $0.322 nms^{-2}$.
The intercomparison of the results when the K_1 group is not split but the theoretical resonance is introduced is given below.
Comparison of PREDICT and T-soft

Extrema $-0.05/+0.05 nms^{-2}$ ($< 0.2\ 10^{-4}$ TR)
scale factor 0.9999899
RMS error 0.0220

Comparison of PREDICT and MT80Tw

Extrema $-0.2./+0.2 nms^{-2}$ ($< 10^{-4}$ TR)
scale factor 0.9999268
RMS error 0.0518

It is clear that PREDICT and T-soft are based on the same models and formula. However most of the remaining discrepancy is concentrated in the TD and QD bands, where on the contrary there is no power left in MT80Tw. MT80Tw and PREDICT agree within 10^{-4}TD. Most of the discrepancy arises in the vicinity of ψ_1 where the reference models for the resonance have a significant difference.

3.3 Magnitude of the different effects

	Error	RMS (nms^{-2})
1. Choice of the elastic model	10^{-3}TR	0.1 to 0.2
2. Influence of W_3 and W_4 on LP, D and SD	$5.\ 10^{-4}$TR	0.610
3. Without considering resonance on ψ_1	$3.\ 10^{-4}$TR	0.322

residual effect on the difference between PREDICT and MT80Tw after correction of the effects 2 and 3, due to the discrepancy between the reference models used for the correction.

Effects 2 & 3	1.010^{-4}TR	0.085
Effect 2 only	0.510^{-4}TR	0.052

The conclusion is that the programs PREDICT and MT80Tw agree at the level of 10^{-4}TR for the computation of the gravity tides on an elastic Earth.

4. Tidal gravity prediction on the real Earth

The main problem for tidal gravity prediction is that the Earth tides are strongly perturbed by the influence of the oceanic tides which modify the tidal parameters distribution at the surface of the Earth. The oceanic tides produce a direct attraction due to the moving water masses, a flexure of the crust and an additional change of the potential due to the mass redistribution.
The ocean tides models of the main tidal constituents are given over a grid and each cell is characterized by its amplitude and phase. The tidal loading is evaluated according to a convolution of the ocean tide model with the Green's functions derived by Farrell (Farrell, 1972). The result called the load vector $\mathbf{L}(L,\lambda)$, where λ characterize the phase difference between the oceanic effect an the Earth tides vector for each wave (Figure 1). It is also possible to compute the equivalent tidal parameters δ_m, α_m that will be introduced in the tidal prediction program: $\mathbf{A}_m(\delta_m.A_{theo}, \alpha_m) = \mathbf{R}(R,0) + \mathbf{L}(L,\lambda)$, with the notations of Fig. 1.

The effect can reach up to 10% of the Earth body tides, but is generally at the level of a few percent. The uncertainties and contradictions between different ocean tides models are such that the dispersion of the corresponding modeled tidal parameters δ_m, α_m is generally at the level of a few tenths of a per cent. In coastal areas it can easily exceed 1%. To demonstrate it we computed modeled tidal factors using 9 different ocean tides models (SCW80, ORI96, CSR3, CSR4, FES95, FES02, NAO99, GOT00 and TPX06). The standard deviation on the amplitude factors σ_δ and the phase differences σ_α is given in the table 1 for three regions: Siberia between 83° and 143° east longitude, Atlantic coast of France, Southern and Eastern Europe.
From Table 1 it is clearly seen that the standard deviation of one model is lower than 0.15% on the diurnal waves.
In the semi-diurnal band the standard deviation is lower than 0.2% inside Siberia and slightly larger close to the Pacific coast. The standard deviation is the same on the in phase and out of phase components and thus in amplitude and phase. In West Europe stations located at 100km from the Atlantic coast of France have standard deviations close to 1% for the out of phase component and thus on the phase. For Mordelles, located in Britanny, the errors are even larger than 1% on both components. For Etna which is far from the Atlantic Ocean the standard deviation is lower than 0.15%. It is clear that the use of the mean of the 9 models will be affected by a RMS error three times lower. It should be necessary to study systematically all the continents in order to identify areas where the contradiction between models are larger. In these regions some models are probably more suitable. For example

along the Atlantic coast of France, Timofeev et al. (2006) recommend the use of CSR3, CSR4 or FES02 on the basis of tidal gravity observations.

Table 1: standard deviation of the tidal factors modelled by 9 different ocean tides models

STATION	O_1		K_1		M_2	
	σ_δ	σ_α	σ_δ	σ_α	σ_δ	σ_α
Novosibirsk	0.00112	0.049°	0.00096	0.045°	0.00180	0.094°
Talaya	0.00100	0.068°	0.00083	0.036°	0.00151	0.076°
Khabarovsk	0.00139	0.095°	0.00078	0.039°	0.00157	0.101°
Y.Sakhalinsk	0.00121	0.095°	0.00057	0.058°	0.00230	0.120°
Menesplet (F)	0.00115	0.068°			0.00186	0.404°
Chize (F)	0.00116	0.067°			0.00212	0.357°
Mordelles (F)	0.00141	0.077°			0.01194	0.776°
Etna	0.00128	0.065°	0.00117	0.073°	0.00136	0.068°
Pecny (9 maps)	0.00099	0.047°	0.00099	0.055°	0.00168	0.042°
(8 maps)					0.00084	0.022°

We can expect that, except in very unfavorable conditions, the standard deviation of the modeled tidal factors is at the level of 0.2%. The use of the mean of several models will increase the precision up to 0.1%.
If we take into account the disagreement between the different models of the elastic response of the Earth at the 0.1% level, we obtain an error budget close to 0.15% of the TR.

A better solution is indeed to perform tidal gravity observations to determine the quantities δ_{obs}, α_{obs}. However the calibration of the best instruments are also questionable at the level of 0.1% and very often calibration errors still exists at the level of 0.2%, even in the GGP network (Ducarme et al., 2002). Moreover to be able to separate the main tidal components a minimum of six months to one year of observations is required.
To summarize, without special care, it is very difficult to ensure an accuracy better the 0.2% of the TR.

5. Conclusions

It is rather easy to insure an accuracy of $1 nm/s^2$ for the prediction of the astronomical tides and all the tested software can achieve it.
For an elastic Earth, it is essential to introduce the effect of the liquid core resonance (0.03%) on one hand and the difference of elastic response for the terms deriving from the potentials of degree 3 and 4 (0.05%) on the other hand. These errors can be corrected with a precision better than 0.01%. However there are still discrepancies at the level of 0.1% between Earth models, according to the underlying hypotheses, such as hydrostatic or non-hydrostatic, elastic or anelastic.
On the real Earth the main perturbation is the ocean tides loading and attraction effect. Using the most recent ocean tides models and avoiding coastal areas, one can expect a precision of 0.1% of the tidal loading computations. Keeping in mind the two main error sources (Earth response and ocean loading) we reach an error budget of 0.15% of the TR, as a minimum. It is a reason why accurate tidal gravity observations can still be useful. However a determination

of the tidal parameters is difficult to achieve with accuracy better than 0.2% and the 0.1% level is exceptional (Francis, 1997; Palinkas, 2006).
For the while an accuracy of 0.2% of TR seems to be accessible either by direct observation of the tidal parameters or by modeling of the ocean tides loading and attraction effects.

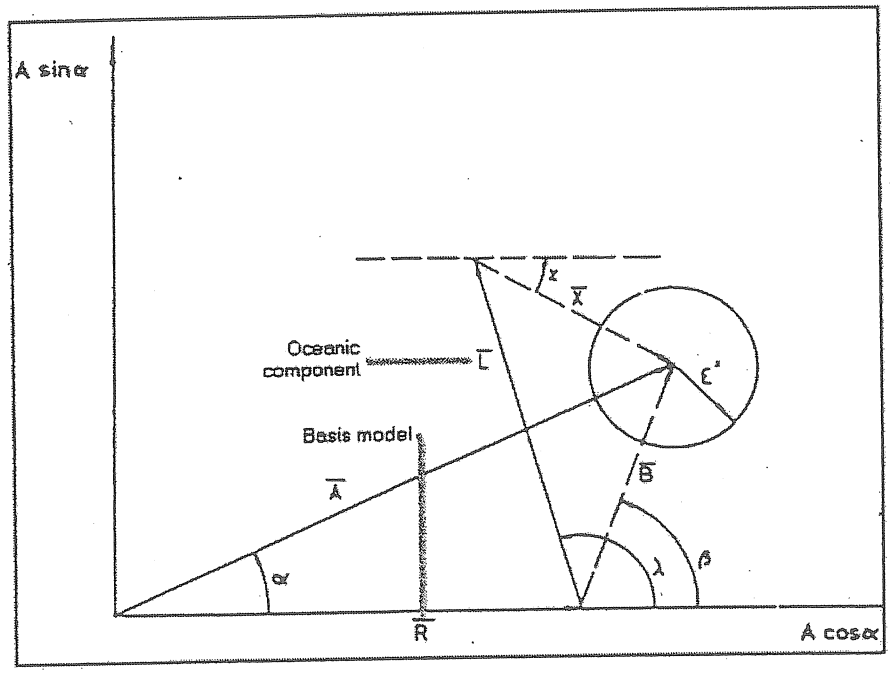

Fig. 1: Relationship between the observed tidal amplitude vector $\mathbb{A}(A,\alpha)$, the Earth model $\mathbb{R}(A_{theo}\delta_{theo},0)$, the computed ocean tides load vector $\mathbb{L}(L,\lambda)$, the tidal residue $\mathbb{B}(B,\beta)$ and the corrected residue $\mathbb{X}(X,\chi)$:

$$\mathbb{B}(B,\beta) = \mathbb{A}(A_{theo}\delta_{obs},\alpha) - \mathbb{R}(R,0)$$

$$\mathbb{X}(X,\chi) = \mathbb{B}(B,\beta) - \mathbb{L}(L,\lambda)$$

A_{theo} is the astronomical tidal amplitude, δ_{obs} is the observed tidal amplitude factor, α is the observed phase difference.

Bibliography

Buellesfeld, F.-J., 1985: Ein Beitrag zur harmonischen darstellung des gezeitenerzeugenden potentials. Deutsche Geodätische Kommission, Reihe C, 314

Cartwright, D.E. and R. J. Tayler, 1971: New computations of tide generating potential. Geophysical Journal, 23, 1.

Cartwright, D.E., Edden, A.C., 1973: Corrected tables of tidal harmonics. Geophysical Journal, 33, 3.

Dehant V., 1987: Tidal parameters for an inelastic Earth. Phys. Earth Planet. Int., 49, 97-116.

Dehant, V., Defraigne, P. and Wahr, J., 1999: Tides for a convective Earth. J. Geophys. Res., 104, B1, 1035-1058.

Doodson, A.T., 1921: The harmonic development of the tide generating potential. Proceedings of the Royal Society, A100, 306-328.

Ducarme, B., Sun, H.P., Xu, J.Q., 2002: New investigation of tidal gravity results from GGP network. Proc. GGP Workshop, Jena, March 11-15, 2002. Bull .Inf. Marées Terrestres, 136, 10761-10776.

Ducarme, B., Xi Qinwen, 2006. A Problem with the Venus terms in the ETERNA software. Bull. Inf. Marées Terrestres, 141.
Farrell, W.E., 1972: Deformation of the Earth by surface load. Rev. Geophys., 10, 761-779
Hartmann, T. and Wenzel H.-G., 1995: Catalogue HW95 of the tide generating potential. Bull. Inf. Marées Terrestres, 123, 9278-9301.
Francis, O., 1997: Calibration of the C021 superconducting gravimeter in Membach (Belgium) using 47 days of absolute gravity measurements. Int. Ass. of Geodesy Symposia Vol 117: Segawa et al.(eds.), Gravity, Geoid and Marine Geodesy, Springer Verlag, 212-219.
Kudryavtsev, S.M., 2004: Improved harmonic development of the Earth tide generating potential. J. of Geodesy, 77, 229-838.
Melchior, P., 1978: The tides of the planet Earth. Pergamon Press, 609pp.
Palinkas, V., 2006: Precise tidal measurements by spring gravimeters at the station Pecny. Proc. 15th Int. Symp. On Earth Tides, Journal of Geodynamics, 41, 15-22.
Roosbeek, F., 1996: RATGP95: A harmonic development of the tide generating potential using an analytical method. Geoph. Journal Int., 126, 197-204.
Tamura Y., 1987: A harmonic development of the tide-generating potential. Bull. Inf; Marées Terrestres, 99, 6813-6855.
Tamura,Y., T.Sato, M.Ooe and M.Ishiguro, 1991: A Procedure for Tidal Analysis with a Bayesian Information Criterion, Geophysical Journal International, 104, 507-516.
Timofeev V.Y., van Ruymbeke M., Woppelmann G., Everaerts M., Zapreeva E.A., Gornov P.Y., Ducarme B., 2006: Tidal gravity observations in Eastern Siberia and along the Atlantic coast of France. Proc. 15th Int. Symp. On Earth Tides, Journal of Geodynamics, 41, 30-38
Van Camp, M. and Vauterin P., 2005: Tsoft: graphical and interactive software for the analysis of time series and Earth tides. Computers & Geosciences, 31, 631-640.
Venedikov, A.P., Vieira, R., 2004: Guidebook for the practical use of the computer program VAV – version 2003. Bull. Inf. Marées Terrestres, 139, 11037-11102.
Wenzel, H.-G., 1996: The nanogal software: Earth tide data processing package ETERNA 3.30. Bull. Inf. Marées Terrestres, 124, 9425-9439.
Xi Qinwen, 1989: A new complete development of the tide-generating potential for the epoch J2000.0. Bull. Inf. Marées Terrestres, 99, 6766-6812.

A Problem with the Venus terms in the ETERNA software

Bernard Ducarme* , Qinwen Xi**

* *Research Associate NFSR, Royal Observatory of Belgium, Av. Circulaire 3, B-1180Brussels, Belgium*

** *Institute of Seismology, Chinese Seismological Bureau, Beijing*

A large peak is found in the spectrum of the differences (Fig. 1) between the tidal prediction program MT80TW (ICET, http://www.astro.oma.be/ICET/), based on the original Tamura's formula (BIM99, 6813-6855, 1987), and PREDICT (H.G.Wenzel, 1996). It is located inside the T_2 group. It is well known that some constituents, derived from Jupiter and Venus (Fig. 2), are located in this group (waves 978, 979, 983 and 984).

A direct comparison of the Tamura's formula with Wenzel (1994) ones is not easy as the two authors are not using the same arguments to define the Jupiter and Venus positions.

Tamura argument f_7 is referring to Jupiter's opposition and f_8 to Venus superior conjunction.

Wenzel argument k_{10} is the mean longitude of Jupiter and k_8 the mean longitude of Venus.

It is easy to convert from one system to the other as

$f_8 = 180° - (h - k_8)$

And

$f_7 = h - k_{10}$

where h is the mean longitude of the sun.

From the first order expression in PREDICT with origin in JD 2451545.0

$h = 280°.47 + 360007.70*DTM$

$k_8 = 181°.98 + 585192.13*DTM$

we get

$f_8 = 81°.51 + 225184.4*DTM$

In Tamura, 1987 we have

$f_8 = 81°.5 + 22518.44*TD$

with DTM=TD/10

We see that at the first order in TD the definition is identical. It should be noted that an initial phase of 180° is equivalent to a change of sign of the term. It will matter only for terms where the argument f_8 is multiplied by an odd number. Among the few terms generated from Venus in Tamura development only the term 984, located in the group T_2, has an odd argument (-1) for f_8. Its sign should thus be changed with respect to original Tamura work when the Wenzel formulation is used. It is not what has been done by Wenzel.

One will find in Table 1 a comparison of the Venus terms 979 and 984 (T_2 group) with angular speed 29°.94862323 and 29°.97431161 in the original Tamura (1987), TamuraHW (Wenzel normalisation) and Hartmann-Wenzel (HW95) tidal developments:

In HW95 potential (variant c) the sign of the terms corresponding to 984 is effectively reversed to introduce the 180° initial phase in the definition of the argument, but it is not so in the transposition of the Tamura development (TamuraHW). PREDICT is always using the Wenzel convention for TamuraHW as well as for HW95. The result is thus not correct using TamuraHW and a fictitious wave with a peak to peak amplitude close to 0.015nms^{-2} is created (Fig 1.). The associated RMS errors is 0.0057nms^{-2}.

When the sign of term 984 is changed in TamuraHW the difference between PREDICT and MT80tw is comprised between -0.01nms^{-2} and +0.02nms^{-2} with a RMS error of 0.0028nms^{-2}.

Table 1

Comparison of the Venus terms in T2 group according to different authors

a) Tamura amplitudes expressed in Doodson's convention

b) Tamura amplitude expressed in fully normalised harmonics following Wenzel in TamuraHW.

c) HW95

VE: direct Venus potential, SU: indirect effect (perturbation term)

	τ s h	f_8	k_8			
For term 979						
a)	979 2 2 -2 0 0 0 0 -2			29.94862323	-.000021 .00000	SU
b)	979 2 2		-2	29.94862323	-285595. 0.	SU
c)	9916 2 2 0		-2	29.94862322	-283878 -1879.	SU
	9917 2 2 0		-2	29.94862322	12598. -2537.	VE
For term 984						
a)	984 2 2 -2 0 0 0 0 -1			29.97431161	.000013 .000000	SU
b)	984 2 2 -1		-1	29.97431161	176797. 0.	SU
c)	9992 2 2 -1		-1	29.97431161	-181048. 334.	SU
	9993 2 2 -1		-1	29.97431161	-20551. 3020.	VE

For the tidal analysis this error can affect the determination of the T_2 wave (term 982), a rather weak constituent next to the incriminated term 984. This can only be tested on a very good data set such as the superconducting gravimeter C034L at Moxa for which the standard deviation on the unit weight is 0.576nms^{-2}.

The analysis has been performed on 1302 days between 2000/01/01 and 2003/08/31 with program ANALYZE, PERTZEV filter and Tamura or HW95 developments. The first column is the result before the correction, the second one the result after the correction and the third one HW95 with 3,268waves (treshold 1.10^{-6}).

The tidal analysis results are slightly modified in the vicinity of T_2 as shown below in Table 2. The differences are concentrated on T_2. L_2 which has the same theoretical amplitude is practically not modified. The results become closer to the results of HW95. The difference is well below the associated errors even on T_2. It is thus not necessary to reprocess all previous analyses.

Bibliography

Tamura Y., 1987: A harmonic development of the tide-generating potential. Bull. Inf; Marées Terrestres, 99, 6813-6855.

Hartmann, T., Wenzel, H.-G., 1994: Catalogue of the Earth tide generating potential due to the planets. Bull. Inf. Marées Terrestres, 119, 8847-8880.

Wenzel, H.-G., 1996: The nanogal software: Earth tide data processing package ETERNA 3.30. Bull. Inf. Marées Terrestres, 124, 9425-9439.

Table 2
Tidal analysis results around the group T2 where the term 984 is located

		TamuraHW previous		TamuraHW corrected		HW95	
RMS error on unit weight (nms^{-2})		0.576		0.575		0.572	
	$A_{th}(nms^{-2})$	δ	α	δ	α	δ	α
LAMBDA2	2.2284	1.18179	1°.2593	1.18174	1°.2593	1.18208	1°.3334
		±.00466	±.2261	±.00468	±.2267	±.00473	±.2294
L2	8.5416	1.17387	1°.6332	1.17387	1°.6325	1.17331	1°.5706
		±.00136	±.0666	±.00137	±.0668	±.00138	±.0676
T2	8.2191	**1.18840**	**0°.3550**	**1.18817**	**0°.3595**	**1.°18778**	**0°.3613**
		±.00128	**±.0618**	**±.00128**	**±.0619**	**± .00130**	**±.0627**
S2	140.5965	1.18354	0°.3860	1.18355	0°.3862	1.18352	0°.3914
		±.00008	±.0037	±.00008	±.0037	±.00008	±.0038

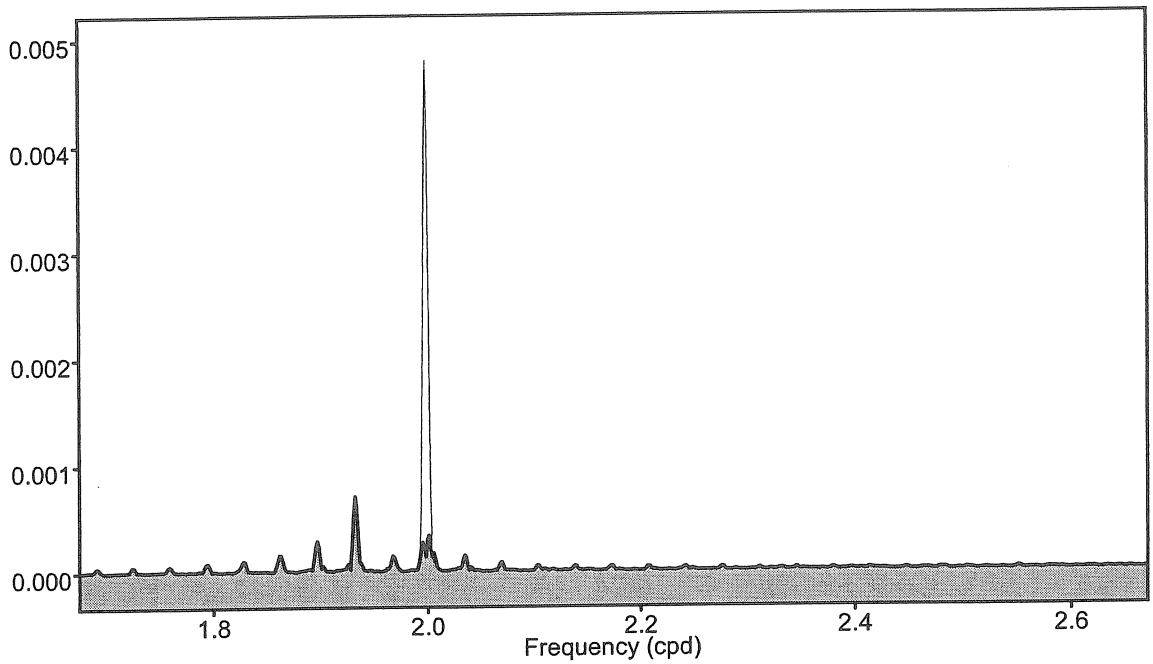

Fig. 1: Difference between MT80tw and PREDICT before and after correction of wave 984 sign in TAMURAHW.DAT.

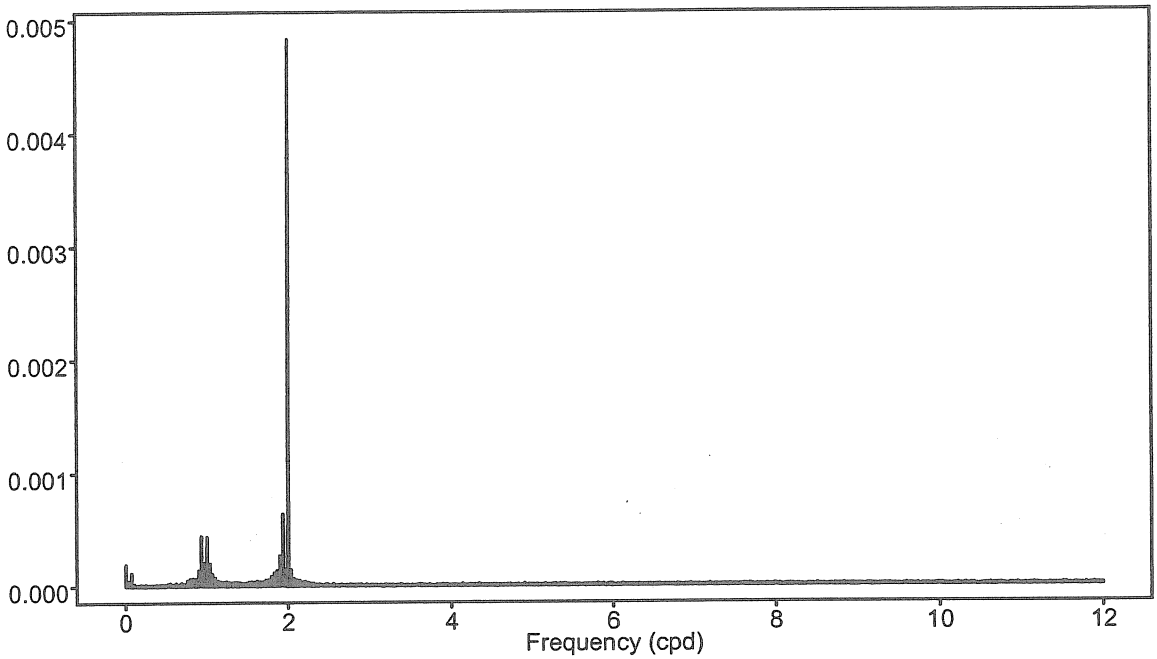

Fig 2: Spectrum of the Venus terms in Tamura development

Estimation of the precision by the tidal analysis programs ETERNA and VAV

B. Ducarme*, L. Vandercoilden*, A.P. Venedikov**

* Royal Observatory of Belgium, ducarme@oma.be
** Geophysical Institute, Bulgarian Academy of Sciences, venedikov@yahoo.com

Abstract

A comparison between the algorithms, used by the programs ETERNA and VAV for estimation of the precision is made. It is shown that the algorithm of ETERNA does not use the principles of the least squares method, because it does not use sum of squares of residuals. VAV uses sum of squares of residuals of filtered numbers in a time/frequency domain. However, the variant of the algorithm used till now does not take into account the deviation of the noise from the normal distribution. In a new version of VAV a test of normality is included and a further development of the analysis method by applying weight of the filtered numbers.

1. Introduction.

The initial intention of this paper was to present results of comparative analyses of Superconducting Gravimeters (SG) data by the programs ETERNA (Wenzel, 1994) and VAV (Venedikov et al., 2001, 2003, 2004, 2005, Ducarme et al., 2004, 2005, 2006a,b). The aim was, by using the estimates of the precision, to make conclusions about the advantages of one or another of the programs.

In this connection we have carefully studied, actually for the first time, the algorithm used by ETERNA for the computation of the root mean square errors (RMS). It was surprising to establish that the RMS of ETERNA are not Least Squares (LS) estimates, i.e. they are not root mean square errors.

In these circumstances the comparison between the RMS of ETERNA and VAV has lost its sense. Thus the paper had been reoriented to compare the algorithms of the programs used for the estimation of the precision.

In this connection we would like to recall a fundamental principle of the LS estimation of the precision.

The precision is estimated through the root mean square errors (RMS) of the data and the estimated unknowns. In all cases the RMS are to be determined through the sum of squares of residuals (SSQR) of the data. The theoretical reason is that SSQR is expected to have the Pearson χ^2 distribution. Then an expression like $x = 1.182 \pm 0.002$, where 0.002 is the RMS of x has the meaning of a confidence interval with confidence probability 62%. On the basis of the expression $x = 1.182 \pm 0.002$ we can conclude that the true value of x, actually its mathematical expectation E(x), will be

$$\mathrm{E}(x) \in \text{ to the confidence interval } \left(1.182 - t \times 0.002,\ 1.182 + t \times 0.002\right) \qquad (1)$$

where t is the coefficient of Student, depending on a chosen confidence probability. E.g. for probability 95% and a great number of data $t = 1.96$.

If the RMS 0.002 is not computed according to the LS rules through the SSQR, the expression $x = 1.182 \pm 0.002$ has not any concrete statistical meaning.

SSQR can be directly used in this way provided the data are charged by a white noise (WN). This is not the case of the tidal data. Both ETERNA and VAV solve the problem by using frequency dependent RMS of the data, but this is made in completely different ways.

2. Estimation of the precision by ETERNA.

We shall follow how ETERNA determines the RMS $\sigma_{ET}(\delta_g)$ of the amplitude factor δ_g of a tidal group g in one of the main tidal families at f = 1, 2, 3 or 4 (cycles/day) cpd. For revealing the algorithm used we had to decipher it in the FORTRAN code of the program.

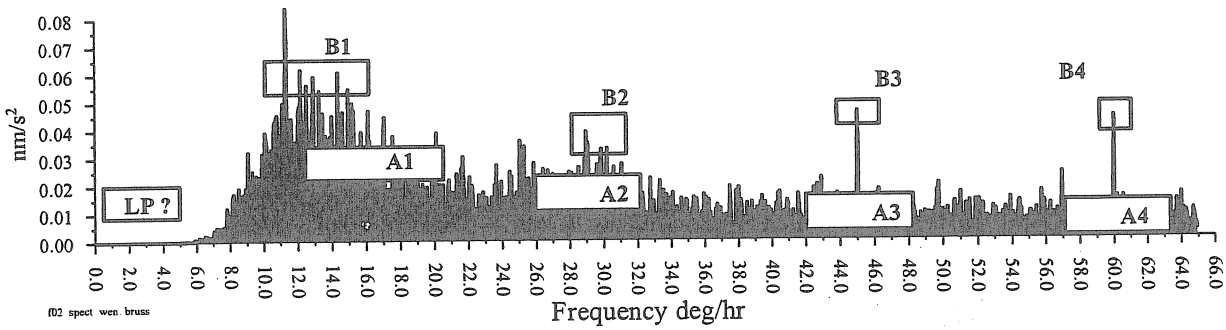

Figure 1. SG data Brussels, ETERNA spectrum of the residuals, obtained with application of the Pertsev filter. The average noise levels $L(f)$ at the frequencies f = 1, 2, 3 & 4 cpd (cycles/day) are determined as arithmetic means of the amplitudes in the intervals, given in Table 1 and indicated in Figure 1 by A1, A2, A3 & A4 respectively.

Table 1. Frequency ranges for the determination of the average noise levels $L(f)$.

Name	Tidal family (cpd)	Angular speed (deg/hr)	
		From	To
L(1)	f = 1	12.0	17.9
L(2)	f = 2	26.0	31.9
L(3)	f = 3	42.0	47.9
L(4)	f = 4	57.0	62.9

The colored character of the noise is taken into account through the spectrum of the residuals of the hourly filtered numbers. It uses the so called "average noise levels" $L(f)$ at frequency f, which are arithmetic means of the amplitudes, as shown by Figure 1 and Table 1.

It also uses the RMS for unit weight σ_0, called in the output "Standard deviation" and computed according to LS under the condition of WN. Then ETERNA determines the so called "Average noise level" at "white noise" L(wn) through

$$L(\text{wn}) = \sigma_0\sqrt{\pi / n}\,, \text{ where } n \text{ is the number of the hourly data.} \qquad (2)$$

It does not correspond to the description of the program ANALYZE in "Manual ETERNA3.3.hlp", where it is stated that L(wn) is "*the estimated Fourier amplitude of the white noise in the frequency band 0-6cpd*". It seems that L(wn) is intuitively computed as the square root of the energy in the basic frequency interval π/n, as σ_0^2 is the total spectral energy.

Further ETERNA determines the RMS $\sigma_{WN}(\delta_g)$ of δ_g, again for the case of WN, as

$$\sigma_{WN}(\delta_g) = C_g.\sigma_0 \qquad (3)$$

where C_g is a coefficient, obtained through the matrix of the LS normal equations.

Finally, ETERNA determines the colored RMS of δ_g as

$$\sigma_{ET}(\delta_g) = \sigma_{WN}(\delta_g)\frac{L(f)}{L(\mathrm{wn})} = C_g \frac{\cancel{\sigma_0} L(f)}{\cancel{\sigma_0}\sqrt{\pi/n}} = C_g . L(f)/\sqrt{\pi/n} \qquad (4)$$

With a good enough approximation $C_g \approx 1/\left(h_g\sqrt{n/2}\right)$, where h_g is the min theoretical amplitude in the group g. By using this we get

$$\sigma_{ET}(\delta_g) \approx L(f)/\left(h_g\sqrt{\pi/2}\right) \qquad (5)$$

In a similar way we get, for the RMS of the phase lag α_g of ETERNA

$$\sigma_{ET}(\alpha_g) \approx L(f)/\left(h_g\sqrt{\pi/2}.\delta_g^2\right) \text{ in radians} \qquad (6)$$

It is strange, that σ_0, which is obtained through the SSQR, finally disappears in these expressions. Also strange is the presence of the $\sqrt{\pi}$ in the definition of L(wn), without any theoretical explanation. The expressions look as intuitive ones, which had been adapted empirically, e.g. by including the term $\sqrt{\pi} = 1.7724$, until ETERNA gets some reasonably looking values.

Further remarks to this way of estimation of the precision are the following.

(i) The RMS σ_{ET} are not LS estimates because they use arithmetic means $L(f)$ of amplitudes instead of SSQR, i.e. the RMS are actually not root mean square errors.

(ii) The levels $L(f)$ depend on how the intervals A are chosen. If we do not obey to the dogmatic definition by ETERNA of the intervals (Table 1), this can be done in many different ways. E.g., if A in Figure 1 are replaced by B, we may get different values of $L(f)$.

(iii) As shown by the example in Section 3 hereafter, in particular cases of the noise ETERNA can provide completely disorientating estimates of the precision.

(iv) The spectrum is computed with a fixed frequency step of 0.05 deg/hr, which is too coarse for long series of data. E.g. for Brussels the frequency step should be 0.0022 deg/hr, i.e. the spectrum looses 90% of the information in the residuals. Possibly, the large step 0.05 deg/hr has been chosen in order to save computer time, which was important earlier, when ETERNA has been developed.

(v) The spectrum is computed till frequencies at 4 cpd, may be again in order to save computer time. Thus it does not allow to obtain $L(f)$ values at higher frequencies, e.g. for the shallow water tides. ETERNA is not prepared for analysis of the ocean tides.

(vi) The precision of the multi-channel analysis is estimated under WN assumption only. Unlike in VAV, these coefficients are not frequency dependent.

3. Estimation of the precision by the VAV program

The main algorithm of VAV, is based on the partition of the data into N intervals $I(T)$ of equal length ΔT and central epochs $T = T_1, T_2, \ldots T_N$. As shown by Figure 2, the intervals are generally without overlapping. If there is a gap, it should remain between the corresponding neighboring $I(T)$. In the case of a gap VAV allows an overlapping of the $I(T)$ in order to avoid loosing data. When a moving filtration is used, as in the method of Chojnicki/ETERNA, every gap brings a loss of data of one length of the filter used.

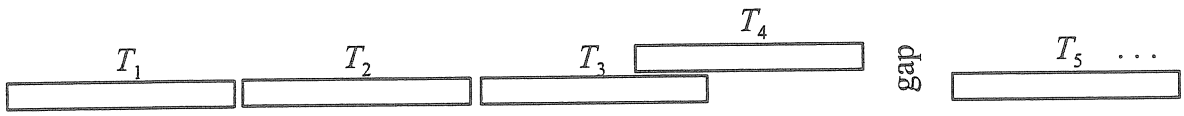

Figure 2. Scheme of the organizing of the intervals $I(T)$ used by VAV.

Figure 3 shows details of an $I(T)$.

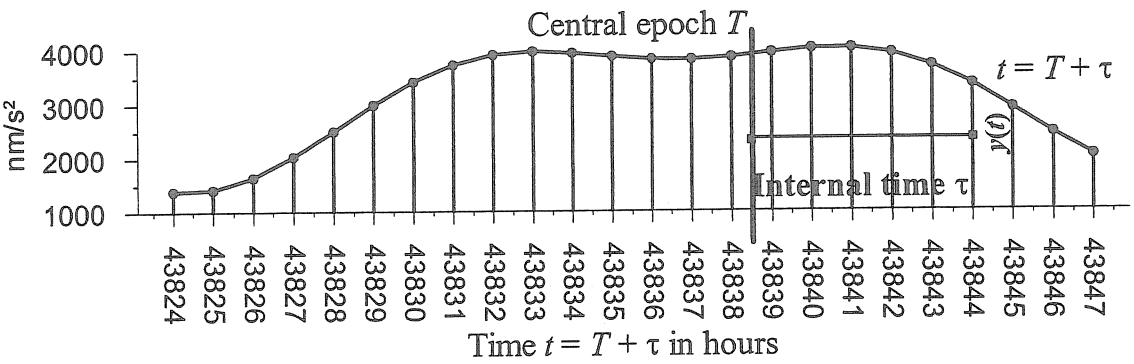

Figure 3. Example of an interval $I(T)$ with $\Delta T = 24$ h.

The drift is represented independently in all $I(T)$ by polynomials of power K_d, i.e. by polynomials having arbitrarily different coefficients in the different $I(T)$.

Our recent experiments have shown that the case of $K_d = 0$ is a very efficient one, especially for $\Delta T = 24^h$, provided the analysis includes the determination of the LP tides in parallel with the shorter D, SD, ... tides (Ducarme et al., 2004). The variant $K_d = 0$ means that the drift is represented by a stepwise function, remaining a constant in every given $I(T)$, which is allowed to freely change between the neighboring $I(T)$.

In this section we shall consider only the case of $K_d = 0$ and $\Delta T = 24^h$ & 48^h, because the general case of these parameters needs sophisticated explanations.

In a first stage of VAV the hourly data $y(t)$ in every $I(T)$ are transformed through filtration into even and odd filtered numbers (u,v), as shown by (6):

$$\left(u_f(T), v_f(T)\right) = \sum_{\tau=-\theta}^{\theta} F_f(\tau) y(T+\tau), \text{ where } \theta = \left(\Delta T - 1\right)/2, \text{ i.e. } 11.5 \text{ or } 23.5 \qquad (7)$$

The filtration is made by using a set of orthogonal filters $F_f(\tau)$, which are complex functions of the internal time τ. For the case considered here

$$F_f(\tau) = \sqrt{2/\Delta T}.\mathrm{Exp}\left(\frac{2\pi f}{24^h}\tau\right) \text{ which amplifies the frequency } f \text{ cpd} \qquad (8)$$

The filters $F_f(\tau)$ eliminate an arbitrary constant, i.e. a polynomial of power $K_d = 0$.

We have a full set of (u,v) quantities, when the (u,v) used are

$$\begin{aligned} &\text{For } \Delta T = 24: \left(u_f(T), v_f(T)\right) \text{at frequencies } f = 1,2, \ldots \mu = 12 \text{ cpd} \\ &\text{For } \Delta T = 48: \left(u_f(T), v_f(T)\right) \text{at frequencies } f = 0.5, 1.0, 1.5, 2, \ldots 11.5, \mu = 12.0 \text{ cpd} \end{aligned} \qquad (9)$$

Due to the orthogonality of $F_f(\tau)$ the full set of (u,v) in (9) is a legal transformation of the hourly data $y(t)$ from the time domain in a time/frequency domain in the following sense. Let LS is applied on $y(t)$ with corresponding observation equations. We shall get identical results through the application of LS on (u,v) by using the same observation equations, modulated by the filters. The transformation remains practically legal, if some of the frequencies, at which useful signals do not exist, are omitted. E.g., if some high frequencies are omitted, i.e. if the highest frequency is $\mu < 12$ cpd.

Following this possibility, VAV applies LS on (u,v) as if (u,v) are the observations. As a result it provides the estimates of the unknowns, in which we are interested, the adjusted $(\tilde{u},\tilde{v})$ of the observed (u,v) and the residuals

$$\Delta u_f(T) = u_f(T) - \tilde{u}_f(T) \;\&\; \Delta v_f(T) = v_f(T) - \tilde{v}_f(T) \text{ for all values of } T \text{ and } f. \qquad (10)$$

If we had data with WN, all u_f & $v_f, f = 1,\ldots\mu$ would have one and the same standard deviation. Then it would be estimated by the RMS for unit weight

$$\sigma_0 = \sqrt{\sum_{f=1}^{\mu}\left(\sum_T \Delta u_f^2(T) + \sum_T \Delta v_f^2(T)\right) \Big/ (2N\mu - m)} \qquad (11)$$

where m is the number of the unknowns.

In fact, the data are charged by "Colored Noise" (ColN), i.e. the standard deviation of u_f & $v_f, f = 1,\ldots\mu$ is dependent on the frequency f, usually increasing with decreasing f (red noise). In the same time we have established, that the sequence

$$\left(u_f(T_1), v_f(T_1)\right), \left(u_f(T_2), v_f(T_2)\right), \ldots \left(u_f(T_N), v_f(T_N)\right) \text{ for a fixed frequency } f \qquad (12)$$

can be reasonably accepted as non-correlated.

On the basis of this VAV solves the problem of the ColN by using separately the residuals $(\Delta u_f, \Delta v_f)$ for getting the RMS $\sigma_v(u,v)$, as an estimate of the standard deviation of (u_f, v_f). Namely, we use the RMS of the data at frequency f computed through

$$\sigma_f(u,v) = \sqrt{\left(\sum_T \Delta u_f^2(T) + \sum_T \Delta v_f^2(T)\right) \Big/ (2N - m_f)} \qquad (13)$$

where m_f is the number of unknowns, whose determination is mostly depending on $\left(u_f, v_f\right)$.

4. An extreme case of a parallel application of ETERNA and VAV programs.

As said above, the quantities (u,v) are a legal transformation of the data $y(t)$. If this is neglected and (u,v) are examined at only one fixed frequency f, it seems that VAV uses a decimation of the data with a time step ΔT. Thus for $\Delta T = 48^h$, earlier used by MV66 (Venedikov, 1966), the Nyquist frequency becomes 0.25 cpd, which is an extremely large frequency. Then, if e.g. the tide O1 with frequency ν(O1) is considered, the waves

$$\begin{aligned} &\text{A1 with frequency } f(\text{O1}) - 0.5 \text{ cpd} \\ &\text{\& A2 with frequency } f(\text{O1}) + 0.5 \text{ cpd} \end{aligned} \qquad (14)$$

are aliases of O1 which cannot be separated from O1 and which may affect the results for O1.

Under such assumptions, Schüller (1978) has shown that if the waves A1 and A2 are added to a series of data the MV66 results for O1 are strongly affected.

It has been shown (Venedikov, 1979) that A1 and A2 can be separated from O1 and thus they are not aliases of O1. Nevertheless, on the basis of the result of Schüller, Wenzel (1997) has declared that MV66 (and thus VAV now) "violates the sampling theorem". It is strange that this severe critic has been made on the basis of the effect of A1 & A2 on MV66 only, but it has not been shown, what is the effect of the same A1 & A2 on other programs, in particular on ETERNA.

In order to avoid confusions we have made a similar experiment, somewhat extended (Table 2), but this time testing both VAV and ETERNA.

Table 2. Variants of testing ETERNA and VAV. The amplitudes of all waves are 38 μgal.

Variant 0: Original SG data Brussels without added waves	
Variant 1: SG data Brussels 1987 – 2000 with added A waves:	
A1 with frequency f(O1) – 0.5 cpd	The "aliases" used by Schüller
A2 with frequency f(O1) + 0.5 cpd	
A3 with frequency f(O1) – 0.25 cpd	Two more waves, related with the supposed Nyquist frequency
A4 with frequency f(O1) + 0.25 cpd	
Variant 2: SG data Brussels 1982 – 2000 with added A waves:	
A1 with frequency f(O1) – 0.5 cpd	The "aliases" used by of Schüller
A2 with frequency f(O1) + 0.5 cpd	
A3 with frequency f(O1) + 1.0 cpd	Two more "aliases"
A4 with frequency f(O1) + 1.5 cpd	
A5 with period 7 hours	A wave, suggested by W. Zürn

VAV has been used with $K_d = 0$ & $\Delta T = 48^h$ and nearly full set of (u,v) in (9) with highest frequency $\mu = 11.5$ cpd.

Let δ_0 is the amplitude factor of a given tide, obtained by the analysis of the data in variant 0 (without A waves) and δ_A is the amplitude factor obtained by the analysis of the data, after the waves A are added. Then the effect of the waves A on the amplitude is naturally measured by the difference $\Delta = |\delta_A - \delta_0|$.

The result of the comparison is shown by Figure 4.

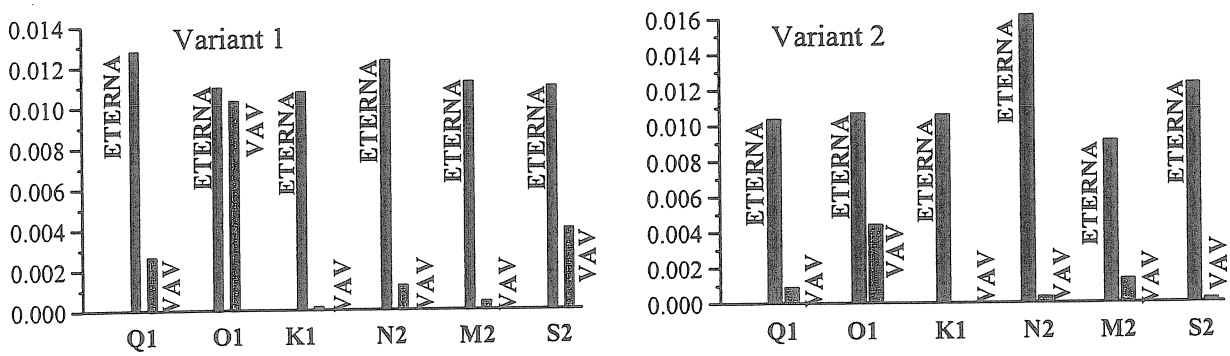

Figure 4. The effect $\Delta = |\delta_A - \delta_0|$ of the added waves A, variants 1 & 2.

Surprisingly or not, the effect of the A waves is, first, considerably higher for ETERNA and, second, it is expanded on all D and SD waves. There is a "third" item, also not in favor of ETERNA, concerning the effect of the A waves on the estimates of the precision.

Figure 5 shows that the effect of the A waves, variant 1, is the addition of a noise, completely deforming the tidal curve. Same is the situation with the data, obtained in variant 2. Obviously, a reasonable result should show a considerably lower precision, i.e. considerable higher RMS, when the data in variant 1 and 2 are analyzed.

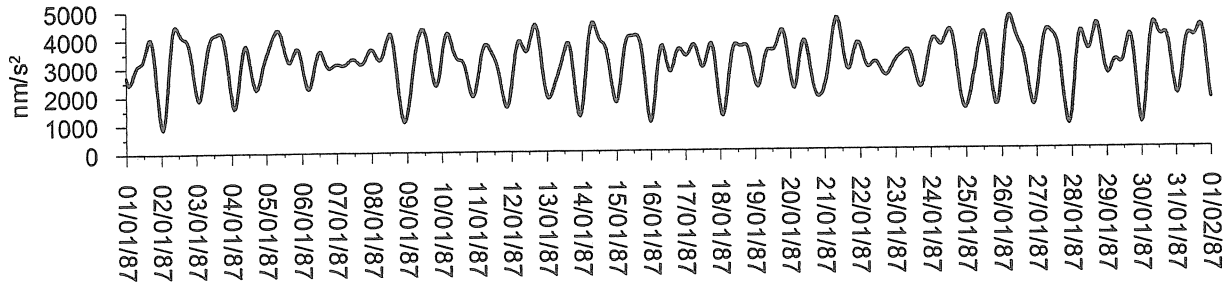

Figure 5. Sample of the data after adding the A waves, variant 1.

Indeed, as shown by Tables 3 and 4, the VAV analyses show considerably lower precision after adding the A waves. E.g. the RMS of δ(M2) in Table 3 is increased from ±.00005 to ±.00619, i.e. more than 120 times.

Table 3. RMS σ of the δ factor of the main D & SD tides of the original data (variant 0) and the data with added A waves (variant 1 in Table 2); SG data Brussels 1987 – 2000.

	Q1	O1	K1	N2	M2	S2
VAV, RMS σ_{VAV}						
Variant 0, No added waves	±.00043	±.00008	±.00006	±.00025	±.00005	±.00011
Variant 1 of added waves	±.03727	±.00713	±.00505	±.03214	±.00619	±.01374
ETERNA, RMS σ_{ET}						
Variant 0, no added waves	±.00037	±.00007	±.00005	±.00022	±.00004	±.00009
Variant 1 of added waves	±.00147	±.00029	±.00021	±.00022	±.00004	±.00009

Table 4. RMS σ of the δ factor of the main D & SD tides of the original data (variant 0) and the data with added A waves (variant 2 in Table 2); SG data Brussels 1982 – 2000.

	Q1	O1	K1	N2	M2	S2
VAV, RMS σ_{VAV}						
Variant 0, No added waves	±.00040	±.00008	±.00005	±.00023	±.00004	±.00010
Variant 2 of added waves	±.01086	±.00207	±.00148	±.00819	±.00157	±.00346
ETERNA, RMS σ_{ET}						
Variant 0, No added waves	±.00035	±.00007	±.00005	±.00022	±.00004	±.00009
Variant 2 of added waves	±.00041	±.00008	±.00006	±.01168	±.00226	±.00493

ETERNA in Table 3 shows only a weak increase of the RMS for the D tides, but absolutely NO changes in the RMS for the SD tides. In Table 4 ETERNA shows more important increase of the RMS for the SD tides, but almost no changes in the RMS of the D tides.

Thus generally, with the exception of the SD case in Table 4, ETERNA failed to notice the huge noise, added to the data.

The explanation of the anomalous estimates of the precision by ETERNA is the dependence of these estimates on the intervals in Figure 1 and Table 1. In the case their frequencies fall out of the intervals, their effect remains inappreciable. This is an exaggerated case but, anyway, it shows the dependence of the estimates of ETERNA on the choice of the intervals.

An attempt to escape from the situation has been made by returning to the option of ETERNA (Table 5) based on the assumption of WN, although this is a non-standard and non-recommended procedure for the D and SD tides. In such a way we have got indeed a considerable increase of the RMS for all tides, i.e. the strong noise became visible. However, the new RMS of ETERNA are still considerably different from VAV and they are strongly dependent on the filters used, which is somewhat strange.

Table 5. An attempt to find more reasonable estimates of the precision by applying ETERNA with the non-standard procedure under the assumption for WN, for variant 2 in Table 2.

	Q1	O1	K1	N2	M2	S2
ETERNA, Assumption of white noise, filter N60M60M2, 167 coefficients						
Variant 2 of added waves	±.03002	±.00633	±.00468	±.03239	±.00633	±.01350
ETERNA, Assumption of white noise, filter PERTSEV59, 51 coefficients						
Variant 2 of added waves	±.02603	±.00508	±.00358	±.02606	±.00504	±.01101

There are very few comparative analyses by ETERNA and VAV. Many of them (but not all of them) show a numerical agreement between σ_{VAV} and σ_{ET}, σ_{ET} always being lower than σ_{VAV} by some 10 to 20%. Such is the case of the RMS for the unperturbed data in Tables 3 & 4. The closeness, which appeared in most cases, should not be considered as universal and thus as a justification of the estimates of ETERNA. The results with the added waves are cases when the similitude completely disappears.

Something more! Let us accept that the similitude of $\sigma_{VAV}(Q1) = 0.00043$ and $\sigma_{ET}(Q1) = 0.00037$ means that $\sigma_{ET}(Q1) = 0.00037$ is a reasonable RMS. Then, since $\sigma_{ET}(Q1) < \sigma_{VAV}(Q1)$, we have also to accept that Q1 is better determined by ETERNA. Actually, since $\sigma_{ET}(Q1)$ is not an LS estimate, from the comparison of σ_{ET} and σ_{VAV} cannot be made anyone of the conclusions: neither "Q1 is better determined by ETERNA", nor "Q1 is better determined by VAV". Same is the situation if we had $\sigma_{VAV}(Q1) < \sigma_{ET}(Q1)$. The reality is that due to the uncertainty on $\sigma_{ET}(Q1)$ we do not know how well Q1 is estimated.

5. A new approach by the variant 2006 of the VAV program

The algorithm, described in Section 3 is used till now and is implemented in (Venedikov et al., 2004). Now we have introduced a further development of this algorithm, described hereafter.

In a discussion Dr. W. Zürn made the reasonable critical remark that VAV implies the assumption that the filtered numbers have a normal Gaussian distribution (ND) and this is actually not proven.

Indeed, the technique considered above is based on the assumption that the set of data $u_f(T), v_f(T), T = T_1, T_2, \ldots T_N$ at given frequency f has a ND. In this connection VAV has included a test of normality, based on the χ^2 criterion of Pearson.

VAV builds the observed or empirical distribution of the residuals $\Delta u_f(T), \Delta v_f(T), T = T_1, T_2, \ldots T_N$ for everyone of the frequencies f and the corresponding theoretical N(0, σ), i.e. central ND with standard deviation σ. The difference between the distributions is measured by the observed χ^2_{Obs} quantity. In the examples here the distributions are determined over 301 intervals with equal expected probability, so that χ^2_{Obs} has 300 degrees of freedom. The value of σ in N(0, σ) is found by making $\chi^2_{Obs} = \text{Min}$. The critical $\chi^2_{Crit} = 342.5$ of Pearson for testing the hypothesis for ND is corresponding to confidence probability 95%. The examples are obtained by the processing of the SG data Vienna 01.07.1997 – 31.12.2002

Figure 6A shows the distribution of the (u,v) at $f = 1$ cpd. In practice, such pictures are often accepted as a satisfactory approximation to a ND. However, according to χ^2_{Crit}, we have NOT an ND, because χ^2_{Obs} exceeds considerably χ^2_{Crit}.

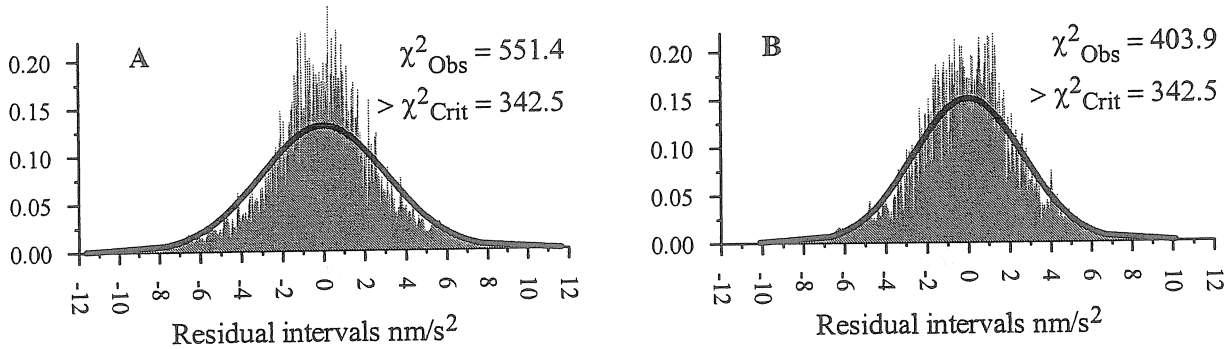

Figure 6. Observed density distribution of the residuals at $f = 1$ cpd (filed grey curve) and the corresponding ND (thick line). A: all residuals; B: eliminated large residuals (7.5% data).

Such is the case of most of the SG data we have tested. It appeared that one of the reasons for the deviations from the ND is that there is proportionally too many large residuals. Indeed, as shown by Figure 6B, when the option (Venedikov et al., 2004) of automatic elimination of data with big residual is applied, the difference between χ^2_{Obs} and χ^2_{Crit} is considerably reduced, although strictly considered, the inference is that the distribution remains not ND.

We came considerably closer to ND in the following new way of applying VAV.

VAV is run in two general loops A & B. In A VAV follows Section 3. In addition, it provides a separate determination of the RMS of u_f & v_f, instead of the common RMS (13). This is made through

$$\sigma_f(u) = \sqrt{\sum_T \Delta u_f^2(T) \Big/ \left(N - m_f\right)} \quad \& \quad \sigma_f(v) = \sqrt{\sum_T \Delta v_f^2(T) \Big/ \left(N - m_f\right)} \,. \tag{15}$$

The idea is to use these RMS in order to apply weights to the filtered (u,v) and thus make them all with (i) nearly normal distribution and (ii) nearly equal variances.

By accepting that a quantity with unit weight should have an RMS equal to the RMS for the WN σ_0, obtained by (11), the weights to be applied become

$$\text{for } u_f : (\sigma_0/\sigma_f(u))^2 \text{ and for } v_f : (\sigma_0/\sigma_f(v))^2 \tag{16}$$

Practically, these weights are introduced through the replacement of the filtered numbers $u_f(T)$ & $v_f(T)$ by what we call weighed filtered numbers

$$\bar{u}_f(T) = \sigma_0 . u_f(T) / \sigma_f(u) \;\; \& \;\; \bar{v}_f(T) = \sigma_0 . v_f(T) / \sigma_f(v) \tag{17}$$

Theoretically, for perfectly well determined RMS, the weighted quantities (17) become observations with equal precision and RMS approximately equal to σ_0.

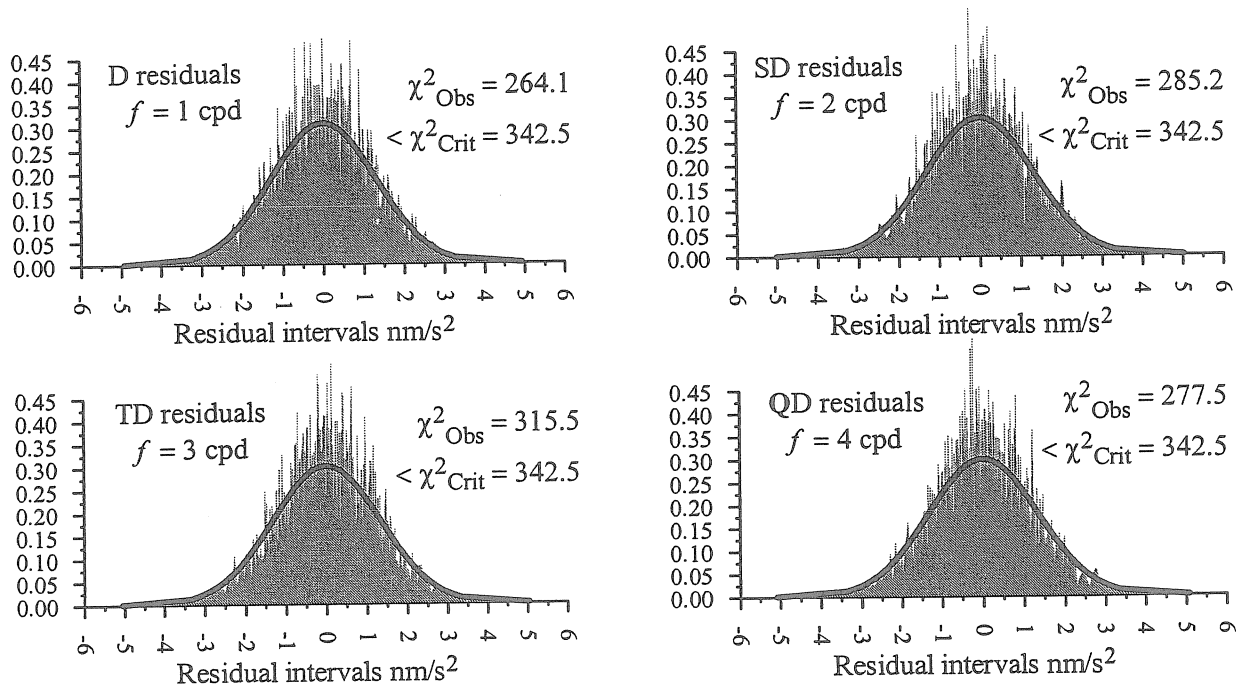

Figure 7 Observed density distribution of the residuals WITH APPLIED WEIGHTS and eliminated large residuals (6.2% of all data) with the corresponding ND.

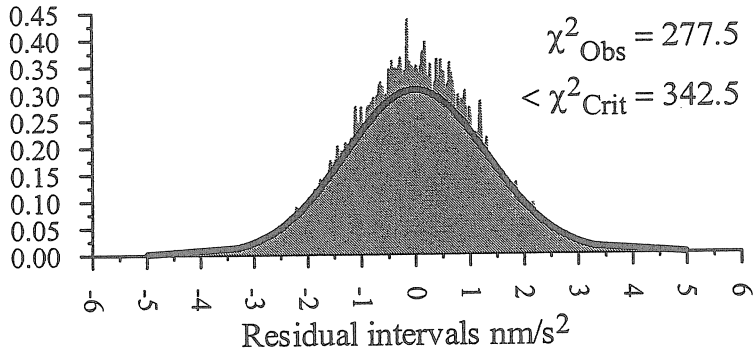

Figure 8 Distribution of the residuals $(\Delta\bar{u}_\nu, \Delta\bar{v}_\nu)$ for all $\nu = 1, 2, 3$ & 4 cpd WITH APPLIED WEIGHTS and eliminated large residuals (6.2% of all data).

Figure 7 shows the effect of the weights on the distribution of the residuals of the weighed quantities, separately for the main frequencies. In all cases we get a rather acceptable approximation to ND with χ^2_{Obs} clearly under the χ^2_{Crit}.

Very important is that the approximation of the ND of the residuals of all main frequencies together, as shown by Figure 8 is also satisfactory.

Unfortunately, the positive results in Figures 7 & 8 are obtained by applying an elimination of a considerable quantity of data (6.2%) with too high residuals. One of the sources of these big residuals may be due to the preprocessing of the data. ETERNA is based on a moving filtration of the data, which does not support a great number or gaps. Due to this the authors of the data are obliged to keep in the data obviously anomalous data, as well as to apply massive data reparations and interpolations, which operations introduce noise of very bad properties.

Conclusions.

We hope that this paper can attract the attention of the tidal community to the importance of the estimation of the precision. Actually, the result about a parameter x has to be represented by two numbers: the value of x and its RMS. The value without the RMS is as useless, as the RMS without the value. No need to say, that the RMS has to be determined according to the rules of the mathematical statistics, i.e. according to the LS rules. Otherwise, an incorrect RMS is equivalent to or worse than a missing RMS.

The analysis of the tidal data has to solve a difficult problem. In principle, now is firmly accepted, that the LS is perfectly suitable general method. The problem is that the data are correlated, i.e. they are charged by a colored noise. In the same time we do not dispose a priori by the covariance matrix, in order to correctly apply the MLS. The compromise, accepted by both ETERNA and VAV is to estimate the unknowns by creating the observation equations under the condition of WN. This does not affect seriously the values of the unknowns, because we always deal with very great number of data.

In the same time, since the colored noise has a frequency dependent effect, the colored character of the noise is taken into account through the estimation of the precision by frequency dependent RMS. Nevertheless, the RMS should observe the general LS principle to be determined through sums of squares of residuals, in order to be able to apply fundamental statistical tools, like the confidence intervals of Student.

It has been demonstrated that the RMS of ETERNA are, unfortunately, not LS estimates and they depend on some intuitive assumptions. Something more, there are cases in which these RMS can be completely disorientating. In addition to the extreme case, considered in Section 3, such is the doubtful case of the RMS of the parameters of the auxiliary channels in the multi-channel analysis. The case of LP waves is even more complicated and is treated in a separate paper (Ducarme et al. 2006c).

The paper has discussed the estimates of the precision, proposed by VAV. They are certainly not the ideal solution but, at least, they follow the LS principle to use the squares of the residuals. In the same time, as shown in Section 5, we have found a weak element in the RMS estimation, applied until now. Namely, it appeared that the distribution of the residuals, rigorously checked, deviates from the ND of Gauss. We have not hesitated to introduce corresponding improvement in VAV, which has brought the residuals nearly to the ND. In addition, it seems that the solution of the problem will generally improve the precision of the analysis results.

We believe that the decision to immediately modify VAV when a weak element is found is a good example of a scientific approach. In our opinion the researchers, tightly devoted to the use of ETERNA, should follow this example and critically reconsider the method of preprocessing and analysis they are currently using, especially in its options for the estimation of the precision.

Acknowledgements

The authors are grateful to Walter Zürn for his suggestions and to the members of the Global Geodynamics Project (Crossley et al., 1999), who provided the SG data.

References.

1. Chojnicki, T., 1972. Determination des parameters de marées par la compensation de observations au moyen de la méthode des moindres carrées. *Publications of the Institute of Geophysics, Polish Academy of Sciences, Marees Terrestres*, **55**, 43-80.
2. Crossley, D., Hinderer, J., Casula G., Francis O., Hsu, H.T., Imanishi, Y., Jentzsch G., Kääriäinen J., Merriam, J., Meurers B., Neumeyer J., Richter B., Shibuya K., Sato T., Van Dam T., 1999. Network of superconducting gravimeters benefits a number of disciplines. *EOS,* **80**, 11, 121/125-126
3. Ducarme B., Venedikov A.P., Arnoso J., Vieira R., 2004. Determination of the long period tidal waves in the GGP superconducting gravity data. *Journal of Geodynamics*, **38**, 307-324.
4. Ducarme B., Van Ruymbeke M., Venedikov A.P., Arnoso J., Vieira R., 2005. Polar motion and non-tidal signals in the superconducting gravimeter observations in Brussels. *Bulletin d'Informations des Marées Terrestres*, **140**, 11153-11171.
5. Ducarme B., Venedikov A.P., Arnoso J., Vieira R., 2006a. Analysis and prediction of the ocean tides by the computer program VAV. *Journal of Geodynamics*, **41**, 119-127.
6. Ducarme B., Venedikov A.P., Arnoso J., Chen X.D., Sun H.P., Vieira R., 2006b. Global analysis of the GGP superconducting gravimeters network for the estimation of the polar motion effect on the gravity variations. *Journal of Geodynamics*, **41**, 334-344.
7. Ducarme B., Vandercoilden L., Venedikov A.P., 2006c. The analysis of LP waves and polar motion effects by ETERNA and VAV methods. *Bulletin d'Informations des Marées Terrestres*, 141, 11201-11210.
8. Schüller K, 1978. About the sensitivity of the Venedikov tidal parameter estimates to leakage effects. *Bulletin d'Informations des Marées Terrestres*, **78**, 4635 4648.
9. Venedikov A.P., 1966. Une méthode d'analyse des marées terrestres à partir d'enregistrements de longueurs arbitraires. *Acad. Royal Belg., Bull. Cl. Sci.*, LII, **3**, also in *Commun. Observ. Roy. Belg., S. Géoph.*, 71, 463-485.
10. Venedikov A.P., 1979. The Nyquist frequency and the substitution of the hourly ordinates by filtered values in the Earth tidal analysis. *Bulletin d'Informations des Marées Terrestres*, **81**, 5011-5019.
11. Venedikov A.P., Arnoso J., Vieira R., 2001. Program VAV/2000 for Tidal Analysis of Unevenly Spaced Data with Irregular Drift and Colored Noise. *J. Geodetic Society of Japan*, **47**, 1, 281-286.
12. Venedikov A.P., Arnoso J.,Vieira R., 2003. VAV: A program for tidal data processing. *Computer & Geosciences,* **29**, 487-502.
13. Venedikov A.P., Vieira R., 2004. Guidebook for the practical use of the computer program VAV – version 2003. *Bulletin d'Informations des Marées Terrestres*, **139**, 11037-11102.
14. Venedikov A.P., Arnoso J., Vieira R., 2005. New version of program VAV for tidal data processing. *Computer & Geosciences,* **31**, 667-669.
15. Wenzel H.-G., 1994. Earth tide analysis package ETERNA 3.0. *Bulletin d'Informations des Marées Terrestres*, **118**, 8719-8721.
16. Wenzel H.-G., 1997. Analysis of Earth tide observations. *Lecture Notes in Earth Sciences,* **66**, Springer, 59-75.

The analysis of Long Period tides by ETERNA and VAV programs with or without 3D pressure correction

B. Ducarme*, J. Neumeyer**, L. Vandercoilden*, A.P. Venedikov***
* Royal Observatory of Belgium, ducarme@oma.be
** GeoForschungsZentrum Potsdam, Juergen_neumy@yahoo.de
*** Geophysical Institute, Bulgarian Academy of Sciences, vened@geophys.bas.bg

1. Introduction.

This paper follows the paper Ducarme & al. 2006c which presented a comparison of the programs ETERNA (Wenzel, 1994) and VAV (Venedikov et al., 2001, 2003, 2004, 2005; Ducarme et al., 2004, 2005, 2006a,b) for the diurnal and subdiurnal periods.

In this connection we have carefully studied, actually for the first time, the algorithm used by ETERNA for the computation of the MSD (mean square or standard deviations), i.e. for the estimation of the precision. Although this program is based on the LS (least squares) method, it was surprising to establish that its MSD are not LS estimates. It was found that ETERNA uses an intuitive computational scheme, without a statistical basis in order to approximate the colored noise characteristics of the residues, so that the results depend on subjective assumptions and parameters, imposed by the program (Ducarme et al., 2006c).

The situation is even more complicated for the Long Period (LP) tides. ETERNA based its evaluation of the MSD on a 1/f hypothesis for what concerns the average noise levels inside the LP band. This assumption is not verified at least with superconducting gravimeters.

Since its first version VAV splits the different tidal bands and evaluates separately the RMS errors in the different tidal bands, but improvements have been recently introduced (Ducarme et al., 2006c). For the evaluation of the LP waves, VAV splits the LP band in two parts: the groups from MSQM to MSM are evaluated together with the Diurnal waves, while Sa and Ssa are evaluated through a so called "zero" filter, i.e. daily mean of the data. ETERNA uses original unfiltered data and allows the representation of non-harmonic phenomena such as the drift by Tschebyscheff polynomials of order n, evaluated separately in each data block.

In the following sections we shall first compare the noise evaluation methods. As the polar motion, with its Chandler term at 430 days, is the main known source of noise close to the groups Sa and Ssa, we shall compare the reactions of the two analysis methods when the pole tide is subtracted or not.

Finally the 3D pressure correction model of Neumeyer et al. (2004 & 2006) is applied and the associated noise decrease is evaluated.

2. Estimation of the LP waves noise by ETERNA.

ETERNA uses the amplitude spectrum of the residuals, in order to determine the so called average noise levels L(i), $0 \leq i \leq 4$ cycles per day (cpd), as frequency dependent estimates of the precision (Table 1).

The average white noise level L(*wn*) is directly computed from the RMS error on the unit weight σ_0 and the number of observations n by the relation (Ducarme et al., 2006c)

$$L(wn) = \sigma_0 \sqrt{\pi / n} \qquad (1)$$

The average noise levels L(i) at the frequencies 1, 2, 3 & 4 cpd (cycles/day) are determined by the arithmetic means of the amplitudes in the intervals, given in table 1.
For D, SD, TD and QD waves the errors evaluated by Least Squares under the white noise assumption are directly scaled by the ratio L(i)/*L(wn)* with i=1,2,3,4

For LP waves the procedure is slightly different.
The noise at the tidal wave frequency *f* is estimated by

$$\text{noise}(f) = L(0) * f_0 / f \qquad (2)$$

f_0 = 0.1cpd, L(0) average noise level between 0.1°/h and 2.9°/h

Finally a scaling factor is given as

$$\text{Scale} = \text{noise}(f)/L(wn) \qquad (3)$$

The underlying assumption is that we have a colored noise in *1/f* in the LP band.

Table 1: frequency range for the determination of the average noise levels L(i) by ETERNA

Name	Tidal family (cycles/day)	Angular speed (degrees per hour)	
		from	to
L(0)	LP	0.1	2.9
L(1)	1	12.0	17.9
L(2)	2	26.0	31.9
L(3)	3	42.0	47.9
L(4)	4	57.0	62.9
L(wn	White noise		

We computed detailed amplitude spectra of the residues using Tsoft (Van Camp and Vauterin, 2005) and produced average values L(lp) in the frequency ranges given in Table 2 and corresponding to the different wave groups. Let us consider now the evolution of L(lp) inside the different LP groups, in order to check if it follows the *1/f* dependence. The increase of L(lp) is well correlated with the ratio f_0/f in the range covered by L(0) with r=0.98, but the regression coefficient is only 0.07. The mean value of L(0) for the three stations (0.202nm/s^2) corresponds to the frequency of MSF and not to the middle of the frequency range at 01cpd (Mstm group). It is normal as the dependence is in *1/f*.
For what concerns the Very Long Period (VLP) tides Ssa and Sa the observed noise is well below the value extrapolated using a *1/f* law, for which the noise level of VLP tides should be 12 or 25 times larger than the noise at Msf frequency.

It is thus not justified to apply this *1/f* correction and we recommend the use of the same formula for LP waves as for the other tidal families. To rescale the estimated errors it is only necessary to divide them by the factor f_o/f given in the last column of table 2.

Table 2 : Average Noise Level L(lp) evaluation of the residues for the LP groups.
Pole tide is subtracted. Local pressure correction is applied.

a) The spectral amplitudes are computed using Tsoft (Van Camp and Vauterin, 2005) and averaged in the frequency range indicated in columns 2 and 3.

Group	Low	High	Vienna 199707-200212	Strasbourg 199703-200305	Membach 199508-200306	Mean	f_o/f
	cpd	cpd	nm/s^2	nm/s^2	nm/s^2	nm/s^2	
Sa	.0025	.0041	1.193	3.820	1.837	2.283	36.606
Ssa	.0041	.0209	0.611	0.922	0.902	0.812	18.262
Msm	.0209	.0326	0.270	0.263	0.381	0.305	3.181
Mm	.0326	.0547	0.191	0.311	0.266	0.256	2.755
Msf	.0547	.0692	0.188	0.197	0.200	0.195	1.477
Mf	.0692	.0913	0.129	0.153	0.169	0.150	1.366
Mstm	.0913	.1055	0.154	0.169	0.140	0.154	.945
Mtm	.1055	.1228	0.159	0.143	0.114	0.139	.913
Msqm	.1228	.1450	0.110	0.134	0.118	0.121	.710
Mqm	.1450	.1830	0.104	0.115	0.098	0.106	.686

b) The spectral amplitudes are computed by ANALYZE with a fixed increment of 0..0033cpd (0.05°/hr).

L(0)	.0066	.1933	0.190	0.208	0.209	0.202	
L(00)	.0040	.0400	0.597	0.771	1.025	0.798	

However this solution is not optimal for the VLP tides Sa and Ssa. For these groups the L(lp) value is much higher than L(0).
It is not astonishing as the annual period and its harmonics are much perturbed by meteorological phenomena. Moreover the pressure correction based on local pressure observations is no more sufficient at periods larger than 50 days (Hu et al., 2006).
It could be possible to introduce in ETERNA program a quantity L(00) estimated between 0.0040cpd and 0.040cpd and thus centered at 0.022cpd. The lower frequency limit corresponds to 250 days in order to avoid the inclusion of the Chandler and annual periods. The higher frequency is inside the MM group. The frequency range has to be large due to the low resolution (0.05°/h) of the spectrum given in the output of the program ANALYZE. This L(00) noise level is 3 to 5 times larger than the L(0) one. It is compatible with the noise ratio between the VLP waves and Mm.

3. Determination of the RMS errors on LP waves by VAV.

The main algorithm of VAV, is based on the partition of the data into N intervals $I(T)$ of equal length ΔT and central epochs $T = T_1, T_2, \ldots T_N$.

In a first stage of VAV the hourly data $y(t)$ in every $I(T)$ are transformed through filtration into even and odd filtered numbers (u,v), as shown by (4):

$$\left(u_f(T), v_f(T)\right) = \sum_{\tau=-\theta}^{\theta} F_f(\tau) y(T+\tau) \quad (4)$$

For hourly data we can define 12 frequency bands $0 \le f \le 11$ cpd
VAV applies LS on (u,v) as if (u,v) are the observations. As a result it provides the estimates of the unknowns, in which we are interested, the adjusted $(\tilde{u},\tilde{v})$ of the observed (u,v) and the residuals

$$\Delta u_f(T) = u_f(T) - \tilde{u}_f(T) \;\&\; \Delta v_f(T) = v_f(T) - \tilde{v}_f(T) \text{ for all values of } T \text{ and } f\,. \quad (5)$$

If we had data with White Noise, all u_f & $v_f, f = 1,\ldots\mu$ would have one and the same standard deviation. Then it would be estimated by the RMS for unit weight

$$\sigma_0 = \sqrt{\sum_{f=1}^{\mu}\left(\sum_T \Delta u_f^2(T) + \sum_T \Delta v_f^2(T)\right) \Big/ (2N\mu - m)} \quad (6)$$

where m is the number of unknowns.
VAV solves the problem of the Colored Noise by using separately the residuals $(\Delta u_f, \Delta v_f)$ for getting the RMS $\sigma_f(u,v)$, as an estimate of the standard deviation of (u_f, v_f). Namely, we use the RMS of the data at frequency f computed through

$$\sigma_f(u,v) = \sqrt{\left(\sum_T \Delta u_f^2(T) + \sum_T \Delta v_f^2(T)\right) \Big/ (2N - m_f)} \quad (7)$$

where m_f is the number of unknowns in each frequency band.
For Sa and Ssa the RMS σ_{LP} at $f=0$ is evaluated from the residuals after application of the "zero filter", while for the other LP groups the value σ_D of the diurnal filters ($f=1$) is used.
It was found recently that the distribution of the residues $\Delta u_f(T), \Delta v_f(T), T = T_1, T_2, \ldots T_N$ was not a normal one. This problem was overcome by the introduction of a weight on the filtered numbers $u_f(T)$ & $v_f(T)$ (Ducarme et al., 2006c).
In section 5 we shall compare the results obtained with and without introduction of the weights.

4. Results obtained with ETERNA3.4 (program ANALYZE)

Table 3 shows the results obtained with the time series of the Superconducting Gravimeter (SG) C025 at Vienna between 1997/07/01 and 2002/12/31, with or without pole tide correction. The data set is subdivided in 3 blocks (1997/07/01-2002/08/28, 2002/08/30-2002/10/17, 2002/10/18-2002/12/31). A second degree Tschebyscheff

polynomial is adjusted on the first block. Local pressure correction is applied. The errors are estimated according to eq. 3 or directly under white noise assumption.

Table 3: estimation of the LP tidal factors at Vienna by ETERNA3.4 analysis program

Wave (ampl.)	no pole tide correction L(0)=0.1928,L(*wn*)=0.1553				pole tide corrected L(0)=0.1898,L(*wn*)=0.0700			
	1/f noise (eq. 3)		White noise		*1/f* noise (eq. 3)		White noise	
(nm/s^2)	δ	α	δ	α	δ	α	δ	α
Sa	3.0131	80.50	3.0131	80.50	2.3130	14.68	2.3130	14.68
(3.164)	±1.7888	±33.53	±.0395	±0.74	±1.7797	±45.64	±.0180	±0.46
Ssa	1.1636	-8.58	1.1636	-8.58	1.1647	-7.81	1.1647	-7.81
(19.928)	±.1436	±7.02	±.0063	±0.31	±.1414	±6.90	±.0029	±0.14
Msm	1.1000	4.43	1.1000	4.43	1.1346	4.61	1.1346	4.61
(4.327)	±.0218	±1.07	±.0271	±1.41	±.1052	±5.30	±.0122	±0.61
Mm	1.1499	0.51	1.1499	0.51	1.1486	0.77	1.1486	0.77
(22.624)	±.0182	±0.91	±.0053	±0.27	±.0179	±0.90	±.0024	±0.12
Mf	1.1484	0.22	1.1484	0.22	1.1460	0.19	1.1460	0.19
(42.826)	±.0055	±0.27	±.0032	±0.16	±.0054	±0.27	±.0015	±0.07
Mtm	1.1193	0.47	1.1193	0.47	1.1287	0.40	1.1287	0.40
(8.200)	±.0194	±0.994	±.0171	±0.88	±.0191	±0.97	±.0077	±0.39
Msqm	1.1914	-0.09	1.1914	-0.09	1.1807	-0.25	1.1807	-0.25
(1.309)	±.0931	±4.24	±.1057	±4.81	±.0916	±4.02	±.0476	±2.09
$\sigma_0(nm/s^2)$	19.21				8.66			

It is obvious that the error evaluation under white noise assumption is very sensitive to the presence of the pole tide. The error is double, following the increase of L(*wn*), which is proportional to the RMS error on the unit weight σ_0. Surprisingly it is not the case for the error expressed according to eq. 3. There is no change at all. It can be understood if one considers the fact that L(0) is not affected by the presence of the polar motion which is outside of the defined frequency range .0066-.0193.As explained in Ducarme et al., 2006c, eq. 5 and 6, the RMS error is directly proportional to L(*f*) and σ_0 is eliminated from the formula. It is thus necessary, when applying the ANALYZE program, to study the spectrum of the residues to check if the is no large peak outside the frequency bands defined in Table 1.

5. Estimation of the LP waves by VAV.

The computations have been made with 4 different options: with or without pole tide correction, with or without weight on the filtered numbers (Table 4). As explained above the VLP components Sa and Ssa are computed with the "zero filter", separately from the other LP groups, which are evaluated together with the diurnal waves. Local pressur correction is used.

We see indeed that the RMS error is always larger on Ssa than on Mm, although both waves have nearly the same amplitude. It corresponds to the results of table 2 showing the noise increase at very low frequency. Considering the "no weight" option, it is

interesting also to note that the pole tide is mainly affecting the error determination in the VLP groups. The RMS error on the unit weight in the diurnal band σ_D is not affected. The introduction of the weight rescales the RMS error on the unit weight. It slightly diminishes the associated RMS errors for the VLP groups and at periods below Mf for the other LP waves. The increase of the RMS errors on Mm and Msm is more pronounced if the pole tide is not corrected

Table 4: estimation of the tidal factors by VAV05 tidal analysis program

Wave (ampl.)	no pole tide corr. no weight		no pole tide corr. weight		pole tide corr. no weight		pole tide corr. weight	
(nm/s^2)	δ	α	δ	α	δ	α	δ	α
Sa	2.9976	88.85	3.1615	87.35	1.8899	12.42	1.9016	14.73
(3.164)	±.1923	±3.58	±.1869	±3.31	±.0886	±2.82	±.0880	±2.78
Ssa	1.2270	-6.12	1.2243	-5.80	1.1838	-5.62	1.1854	-5.55
(19.928)	±.0310	±1.45	±.0281	±1.32	±.0145	±0.70	±.0142	±0.69
$\sigma_{LP}(nm/s^2)$	197.0		59.1		92.0		31.0	
Msm	1.1628	2.79	1.1632	2.71	1.1621	4.26	1.1628	3.30
(4.327)	±.0218	±1.07	±.0449	±2.21	±.0218	±1.07	±.0380	±1.87
Mm	1.1495	0.31	1.14981	-0.10	1.1449	0.56	1.1484	0.09
(22.624)	±.0042	±0.21	±.0077	±0.38	±.0042	±0.21	±.0068	±0.34
Mf	1.1444	0.46	1.1442	0.41	1.1447	0.36	1.1443	0.40
(42.826)	±.0023	±0.12	±.0024	±0.12	±.0023	±0.12	±.0023	±0.12
Mtm	1.1282	0.41	1.1295	-0.06	1.1284	0.43	1.1296	-0.03
(8.200)	±.0105	±0.54	±.0086	±0.44	±.0106	±0.54	±.0085	±0.43
Msqm	1.1869	-1.16	1.1842	-0.83	1.2110	0.06	1.1861	-0.54
(1.309)	±.0573	±2.76	±.0419	±2.68	±.0573	±2.71	±.0415	±2.00
$\sigma_D(nm/s^2)$	32.7		58.7		32.7		30.7	

6. Comparison of the results obtained with ETERNA and VAV

The estimated tidal factors, given in Tables 3 and 4, generally agree within two times the associated VAV errors.

It is clear indeed that we cannot consider the errors determined by ETERNA as reflecting the real signal to noise ratio.

As explained in section 2 we tried to rescale the errors given by the program ANALYZE. In Table 5 we propose three different solutions:

- (1) the original evaluation through eq. 2 and 3;
- (2) a "colored" evaluation after suppression of the f_o/f factor;
- (3) the white noise solution.

For ETERNA, as pointed out in section 4, the white noise evaluation is the only one able to take into account the increase of noise when the pole tide is not corrected, but this increase affects all the spectrum, while it is mainly concentrated on Sa and Ssa with VAV.

When the pole tide is subtracted i.e. when all known error sources are removed, the frequency dependent evaluation (1) gives unrealistic error estimates on Sa and Ssa and increases artificially the RMS errors for frequencies lower than Mf.

Table 5: Comparison of the error determination on the amplitude factors for station Vienna

(1) original ETERNA formula (eq.3)
(2) frequency independent Scale=L(0)/*L(wn)*
(3) white noise

Wave (ampl.)	no pole tide corr. L(0)=0.1928, L(*wn*)=0.1553				pole tide corr. L(0)=0.1898, L(*wn*)=0.0700			
	VAV	ETERNA			VAV	ETERNA		
(nm/s^2)	(no weight)	(1)	(2)	(3)	(no weight)	(1)	(2)	(3)
Sa	0.1923	1.7888	.00490	0.0395	0.0886	1.7797	0.0488	0.0180
(3.164)			*0.2379				**0.1535	
Ssa	0.0310	0.1436	0.0079	0.0063	0.0145	0.1414	*0.0079	0.0029
(19.928)			*0.0382				**0.0243	
Msm	0.0218	0.1069	0.0336	0.0271	0.0218	0.1052	0.0331	0.0122
(4.327)								
Mm	0.0042	0.0182	0.0066	0.0053	0.0042	0.0179	0.0065	0.0024
(22.624)								
Mf	0.0023	0.0055	0.0040	0.0032	0.0023	0.0054	0.0040	0.0015
(42.826)								
Mtm	0.0106	0.0194	0.0212	0.0171	0.0106	0.0191	0.0209	0.0077
(8.200)								
Msqm	0.0573	0.0931	0.1312	0.1057	0.0573	0.0916	0.1290	0.0476
(1.309)								

* based on L(00)=0.937
** based on L(00)=0.597

VAV error determination, which is the only valid one in the LS sense, is generally comprised between the white noise estimation (1) and the estimation (2) "colored" through the ratio L(0)/L(*wn*). For the waves Sa and Ssa one should prefer the estimation based on L(00).

7. Local versus 3D pressure correction

The atmospheric pressure effect is composed of the attraction and elastic deformation terms. The deformation term can be modeled by the Green's function method, using surface pressure data only. For modeling the attraction term 3D data are required in order to consider the real density distribution within the atmosphere, as the same surface pressure may correspond to different density distributions (Neumeyer et al., 2004). From the European Centre for Medium-Range Weather Forecasts (ECMWF) 3D atmospheric pressure, humidity and temperature are now available on 60 height levels up to about 60 km, at an interval of 6 hours and with a spatial resolution of 0.5°x0.5°. Neumeyer et al. (2006) showed that a 1.5° radius is sufficient to evaluate correctly the 3D attraction term.

As the 3D pressure correction model is only available after January 2001, it was not possible to separate the pole tide signal from the Sa group. For station Vienna, the pole tide signal has been subtracted from the gravity data using the tidal factor 1.1526 computed in Ducarme et al., 2006b. The 3D results are compared with the local pressure admittance ones.
With ETERNA the error diminishes throughout the complete LP band when a 3D pressure correction is applied. (Table 6), while with VAV only the VLP groups Sa and Ssa show a diminution of the errors. This behavior has been confirmed in all the studied SG records.

Table 6: Comparison of the results based on the local pressure correction and on the 3D model of Neumeyer et al., 2006. Station Vienna from 2001.01.01 to 2004.12.31
Pressure admittance -2.755 nms^{-2}/hPa (ETERNA), -3.255 nms^{-2}/hPa (VAV diurnal)

a) amplitude factors

LP groups	SA	SSA	MSM	MM	MF
ETERNA*					
Local AP correction	3.2230	1.2121	1.1736	1.1407	1.1494
	±.0600	±.0099	±.0459	±.0087	±.0037
3D AP Correction	3.4551	1.2071	1.21476	1.1372	1.1469
	±.0483	±.0081	±.0375	±.0071	±.0030
VAV					
Local AP Correction	3.17539	1.09390	1.16094	1.15182	1.15062
	±.08330	±.01342	±.04305	±.00746	±.00186
3D AP correction	4.05966	1.09216	1.19928	1.14678	1.14984
	±.08104	±.01245	±.04830	±.00865	±.00247

b) phase differences

LP groups	SA	SSA	MSM	MM	MF
ETERNA*					
Local AP correction	70.307	-4.227	0.566	0.047	0.360
	±1.033	±.454	±2.245	±.437	±.183
3D AP Correction	49.604	-4.492	1.439	-0.080	0.319
	±0.792	±.374	±1.775	±.358	±.150
VAV					
Local AP Correction	28.023	-4.570	0.343	-0.038	0.337
	±1.452	±0.692	±2.124	±0.371	±0.093
3D AP correction	14.519	-5.211	2.339	0.292	0.233
	±1.061	±0.643	±2.309	±0.432	±0.123

* the RMS errors are computed without introduction of the 1/f dependence.

To check how the spectrum of the residues is improved by the 3D pressure correction scheme we compared the amplitude spectra obtained with ETERNA (Table 7a), computing mean values on sliding frequency intervals.

It is clear that the diminution of the noise reaches its maximum around the frequency 6°/h (2.5day), between LP and D tides, and covers the entire LP spectrum. For period shorter than 1.5day the local pressure correction is better. Inside the LP spectrum the averaged amplitude spectra show fluctuations and no clear tendency is appearing in the ratio 3D/local (Table 7b). For Sa the frequency range is probably too narrow to get significant results. We can thus consider that the noise reduction using 3D pressure correction is effective for all the LP groups.
The behaviour of ETERNA is thus normal. As VAV computes the LP tides with frequencies higher than Ssa together with the diurnal waves, the background noise is computed through σ_1 i.e. mainly in the frequency range of L(1). From table 7a it can be seen that there is no improvement in this band. It will thus be necessary to revise the scheme used by VAV for the computation these LP tides.

Table 7: Mean spectral amplitudes in nm/s^2 for different frequency bands

a) The spectral amplitudes are computed by ANALYZE with a fixed increment of 0..0033cpd (0.05°/hr).

Average Noise level	Frequency band °/h		Local pressure correction	3D pressure correction	Ratio 3D/local
L0	0.1	2.9	0.3731	0.3278	0.879
	2.0	6.0	0.1317	0.0925	0.702
	4.0	8.0	0.0885	0.0570	0.644
	6.0	10.0	0.0615	0.0469	0.762
	8.0	12.0	0.0451	0.0405	0.898
	10.0	14.0	0.0362	0.0386	1.066
L1	12.0	17.9	0.0323	0.0450	1.393

b) The spectral amplitudes are computed using Tsoft (Van Camp and Vauterin, 2005) and averaged in the frequency range indicated in columns 2 and 3.

Average Noise level	Frequency band °/h		Local pressure correction	3D pressure correction	Ratio 3D/local
Sa	0.0375	0.0615	2.3128	2.3365	1.010
Ssa	0.0615	0.3135	0.7560	0.6880	0.910
Msm	0.3135	0.4890	0.3564	0.3265	0.916
Mm	0.4890	0.8205	0.2722	0.2476	0.762
Msf	0.8205	1.0380	0.1997	0.1604	0.898
Mf	1.0380	1.3695	0.1507	0.1251	0.830
Mstm	1.3695	1.5825	0.1262	0.0878	0.696
Mtm	1.5825	1.8420	0.1070	0.0951	0.889
Msqm	1.8420	2.1750	0.1303	0.1128	0.866
Mqm	2.1750	2.7450	0.1114	0.0871	0.782

6. Conclusions

To get correct estimations of Sa and Ssa it is very important to eliminate or estimate the pole tide and build a correct polynomial representation of the non harmonic part of the signal.

As already pointed out in Ducarme et al., 2006c, the error estimation by ETERNA is not valid in the Least Squares sense. Moreover the error evaluation by ETERNA is biased by the noise outside the frequency band averaged by L(0), e.g. the pole tide signal, when it is not eliminated.

The users should suppress the $1/f$ dependence in the error estimation for LP tides according to the factors f_0/f given in Table 2 in order to define "colored" errors in a way similar to the short period tides. The true RMS errors are probably comprised between the white noise estimates and the "colored" ones. However, for the VLP tides Sa and Ssa L(0) is underestimating the noise level. The VAV analysis program should be preferred for its correct evaluation of the RMS errors.

The 3D pressure correction scheme is diminishing the background noise inside the entire LP spectrum and down to a period of 1.5 day. However the VAV computing scheme is not reflecting this improvement for LP tides with period lower than 6 months.

References.

1. Ducarme B., Venedikov A.P., Arnoso J., Vieira R., 2004. Determination of the long period tidal waves in the GGP superconducting gravity data. *Journal of Geodynamics*, **38**, 307-324.
2. Ducarme B., Van Ruymbeke M., Venedikov A.P., Arnoso J., Vieira R., 2005. Polar motion and non-tidal signals in the superconducting gravimeter observations in Brussels. *Bull. Inf. Marées Terrestres*, **140**, 11153-11171.
3. Ducarme B., Venedikov A.P., Arnoso J., Vieira R., 2006a. Analysis and prediction of the ocean tides by the computer program VAV. *Journal of Geodynamics*, **41**, 119-127.
4. Ducarme B., Venedikov A.P., Arnoso J., Chen X.D., Sun H.P., Vieira R., 2006b. Global analysis of the GGP superconducting gravimeters network for the estimation of the polar motion effect on the gravity variations. *Journal of Geodynamics*, **41**, 334-344.
5. Ducarme B., Vandercoilden L., Venedikov A.P., 2006c. Estimation of the precision by the tidal analysis programs ETERNA and VAV. *Bul. Inf. Marées Terrestres*, **141**, 11189-11200
6. Hu X.G., Liu L.T., Ducarme B., Hsu H.T., Sun H.P., 2006. Wavelet method determination of long period tidal waves in superconducting gravity data. *Accepted for publication in PEPI.*
7. Neumeyer J., Hagedorn J., Leitloff J., Schmidt T., 2004. Gravity reduction with three-dimensional atmospheric pressure data for precise ground gravity measurements. *Journal of Geodynamics*, **38**, 437-450.
8. Neumeyer J., Schmidt T., Stoeber C., 2006. Improved determination of the atmospheric attraction with 3D air density data and its reduction on ground gravity measurements. *Symp. G3on Earth Processes, Dynamic Planet 2005, Cairns, Australia, August 22-26 2005, Accepted for publication in Journal of Geodesy*
9. Van Camp, M. and Vauterin P., 2005. Tsoft: graphical and interactive software for the analysis of time series and Earth tides. *Computer & Geosciences*, **31**, 631-640.
10. Venedikov A.P., Arnoso J., Vieira R., 2001. Program VAV/2000 for Tidal Analysis of Unevenly Spaced Data with Irregular Drift and Colored Noise. *J. Geodetic Society of Japan*, **47**, 1, 281-286.
11. Venedikov A.P., Arnoso J.,Vieira R., 2003. VAV: A program for tidal data processing. *Computer & Geosciences*, **29**, 487-502.
12. Venedikov A.P., Vieira R., 2004. Guidebook for the practical use of the computer program VAV – version 2003. *Bul.Inf. Marées Terrestres*, **139**, 11037-11102.
13. Venedikov A.P., Arnoso J., Vieira R., 2005. New version of program VAV for tidal data processing. *Computer & Geosciences*, **31**, 667-669.
14. Wenzel H.-G., 1994. Earth tide analysis package ETERNA 3.0. *Bull.Inf. Marées Terrestres*, **118**, 8719-8721.

World Wide Synthetic Tide Parameters a promising tool for high precision tidal prediction

K.H.Zahran

National Research institute of Astronomy and Geophysics, Helwan, Cairo, Egypt

Computations of a synthetic Earth tide parameters by adding the body tide contribution to the ocean tide loading contribution (OTL) on a world wide regular grid is considered to be a promising tool for high precision tide prediction. The advantage of such computations is that the user of the synthetic parameters does not have to carry out the time-consuming OTL computations and that the final set of computed parameters may be used by tide specialists and non-specialists to predict Earth tide at any time every where for local regional or continental applications.

A synthetic Earth tide parameters (Zahran et al. 2005) have been developed on a world wide grid for gravity, vertical and horizontal displacements. Synthetic parameters have been computed using Wahr-Dehant model and different TOPEX/Poseidon ocean tide models. However, beside the Earth tide parameters synthetic ocean tide parameters are also given separately for many other applications.

The accuracy and the reliability of the synthetic tide parameters have been estimated by comparison with observed gravity and vertical displacement tide parameters with those interpolated from the presented synthetic model, which shows good agreement. Tests of the model shows small discrepancies with the observed tidal gravity parameters and a good agreement with tidal displacements parameters, estimated from long period VLBI and GPS observations.

An accuracy assessment study to the selected ocean tide models indicates that the selected models is still problematic in the coastal areas and shelf regions. However, recent generation of derived TOPEX/Poseidon ocean models shows better agreement in coastal area. Thus, the synthetic model has to replace a recent ocean tide model with higher resolution to fulfill the accuracy needed for precise gravity and space geodetic techniques.

.

BIBLIOGRAPHY

Zahran K.H., Jentzsch G., Seeber G. (2005): World-wide synthetic tide parameters for gravity and vertical and horizontal displacements. J. Geodesy, 79, 293-299.

An overview on wavelet multi-resolution decomposition compared with traditional frequency domain filtering for continuous gravity data denoising

Panepinto Stefano[1], Greco Filippo[2], Luzio Dario[3], Ducarme Bernard[1]

[1]*Royal Observatory of Belgium, Brussels, Belgium,* [2]*Istituto Nazionale di Geofisica e Vulcanologia Sezione di Catania, Italy,* [3]*Dipartimento di chimica e Fisica della Terra, University of Palermo, Italy*

Abstract: Continuous gravity recordings in volcanic area could play a fundamental role in the monitoring of active volcanoes and in the prediction of eruptive events too. This geophysical methodology is utilized, on active volcanoes, in order to detect mass changes linked to magma transfer processes and, thus, to recognize forerunners to paroxysmal volcanic events. Spring gravimeters are still the most utilized instruments for microgravity studies because of their relatively low cost and small size, which make them easy to transport and install. Continuous gravity measurements are now increasingly performed at sites very close to active craters, where there is the greatest opportunity to detect significant gravity changes due to a volcanic activity. Unfortunately, spring gravity meters show a strong influence of meteorological parameters (i.e. pressure, temperature and humidity), especially in the adverse environmental conditions usually encountered at such places. As the gravity changes due to the volcanic activity are very small compared to other geophysical or instrumental effects we need a new mathematical tool to get reliable gravity residuals susceptible to reflect the volcanic effect. In the following we present and discuss a preliminary work about the confrontation between the traditional filtering methodology and the Wavelet transform. The overall results show that the performance of the wavelet-based filter seems better than the Fourier one. Moreover, the possibility of getting a multi-resolution analysis and study local features of the signal in the time domain makes the proposed methodology a valuable tool for gravity data processing.
Keywords: *Gravimeter, wavelet transform, filtering, volcanic monitoring*

INTRODUCTION

Studies on the effect of external influencing parameters on the behavior of gravity sensors for the monitoring of volcanic activity have revealed that temperature, pressure and humidity play a very critical role [El Wahabi et al., 1997; Warburton and Goodkind, 1997]. Several authors have demonstrated that meteorological parameters, especially atmospheric temperature, do affect continuously running spring gravimeters. In particular, in El Wahabi et al. (1997) it has been proven that, over a yearly period, temperature changes can cause up to 1 mGal instrumental effect. An admittance up to 0.2 mGal/°C, over changes with period longer than 1 month, has been evidenced in Carbone et al (2003). An important issue with the gravity data sequences is the need of separating the useful signal (i.e. the volcano-related one) from unwanted components (signal due to tides, instrumental and meteorological effects). Obviously, frequency-domain filters cannot be applied to remove the effect of these perturbations since the spectrum of each component of various origins has wide intervals of superposition.

The aim of the present work is to get a preliminary test concerning the application of the wavelet decomposition to the continuous gravity data. The wavelet transform is thus applied to a short sequence (7 months registration) acquired at Mt Etna site (see Figure 1). The continuously running station is located about 2 km NE of the summit NE crater at the "Pizzi Deneri Volcanological Observatory" (PDN; 2820 m a.s.l.). Data presented and analyzed in the following were acquired through L&R PET 1081 gravimeter with a measurement range of about 5 mGal. Besides gravity, other parameters were acquired: ground tilt in two perpendicular directions, atmospheric temperature, pressure, humidity and tension from the power system feeding the station. Data were recorded at 1datum/min sample rate (each datum is the average calculated over 60 measurements)

through a CR10X Campbell Scientific data-logger and transmitted through a wireless connection to Catania.

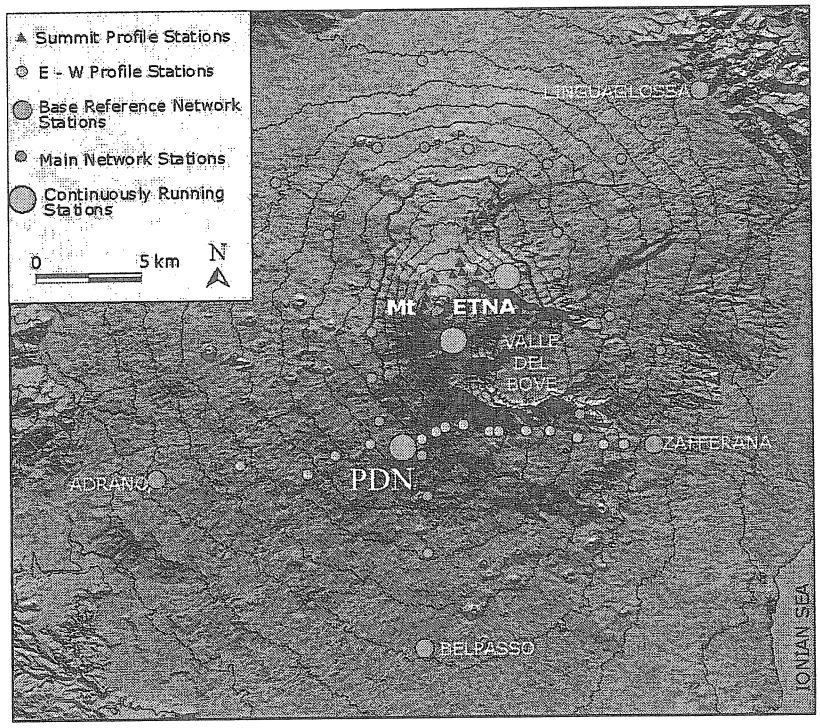

Fig. 1: Sketch map of Mt Etna showing the gravity network installed by INGV

DISCRETE WAVELET TRASFORM AND MULTI-RESOLUTION ANALYSIS

Wavelets are mathematical tools for analyzing time series. As the name suggests, a wavelet is a "small wave". A small wave grows and decays essentially in a limited time period. There are two main classes of wavelets. The first one is the continuous wavelet transform (CWT) which is designed to work with time series defined over the entire real axis; the second, is the discrete wavelet transform (DWT), which deals with series defined over a range of integer values [Percival et al., 2002].
The continuous wavelet transform of a function *f(t)* with finite energy is defined by

$$\widetilde{W}(a,b)=\frac{1}{\sqrt{a}}\int f(t)\psi\left(\frac{t-b}{a}\right)dt \qquad (1)$$

where $b\in R$ and $a\in R^{+}$, with R^{+} being the set of positive real numbers. Every wavelet is obtained by a translation and dilation of a 'mother wavelet' $\psi\in L^{2}(R)$, where $L^{2}(R)$ denotes the Hilbert space of square integrable functions. The function ψ has unit energy and zero mean although higher order moments may also be zero; it is chosen with a compact support to obtain localization in space.
For practical applications the scale parameter a and location parameter b need to be discretized. With the choice $a = 2^{l}$ and $b = ka$ with $l,k\in Z$ (Z is the set of integers), the discrete family of orthonormal wavelets,

$$\psi_{l,k}(t)=\frac{1}{\sqrt{2^{l}}}\psi\left(\frac{t-k2^{l}}{2^{l}}\right)=\frac{1}{\sqrt{2^{l}}}\psi\left(2^{-l}t-k\right), \qquad (2)$$

is obtained by dilating or contracting and translating the function $\psi(t) \equiv \psi_{0,0}(t)$.
In this case, the discrete wavelet transform (DWT) is

$$\tilde{w}_{l,k} = \int_{-\infty}^{\infty} f(t)\, \psi_{l,k}(t)\, dt \tag{3}$$

and the inverse wavelet transform is

$$f(t) = \sum_{l=-\infty}^{+\infty} \sum_{k=-\infty}^{+\infty} \tilde{w}_{l,k} \psi_{l,k}(t) \tag{4}$$

in the L^2-sense.
The framework of multi-resolution analysis, developed by Mallat (1992) and Meyer (1993), allows a signal to be approximated at certain scales or resolutions (Foufoula-Georgiou and Kumar, 1994). At a fixed level l of resolution 2^{-l} samples per unit length, the approximation of the signal is given by its orthogonal projection, $S_l f = \sum_{k=-\infty}^{\infty} \langle f, \phi_{l,k} \rangle \phi_{l,k}(t)$ [1], onto the vector space V_l included in $L^2(R)$. The vector space V_l represents the space of all possible approximated signals at resolution 2^{-l}, and the orthonormal basis $\phi_{l,k}$ derives from a function ϕ defined as the scale function or 'father wavelet'. The details of the signal at any scale 2^l characterize the difference between the process carried out at two different scales 2^l and 2^{l-1}, or equivalently at two different resolutions. If $\psi_{l,k}$ is the orthonormal basis in the vector space O_l (orthogonal complement of V_l in V_{l-1}), the details are given by the orthogonal projection, $D_l f = \sum_{k=-\infty}^{\infty} \langle f, \psi_{l,k} \rangle \psi_{l,k}(t)$, of the original signal on to the vector space O_l, so O_l is orthogonal to V_l, i.e.

$$V_{l-1} = O_l \oplus V_l . \tag{5}$$

If $f(t)$ is defined by a set of m discrete values, the wavelet expansion consists of the coefficients,

$$\tilde{w}_{l,k} \text{ with } l \in [-(L-1), 0];\ k \in [0, 2^{|l|} - 1], \tag{6}$$

where $L = \log_2 m$ (we pick values that are separated by multiples of 2^l).
Using this notation, the finest and the coarsest levels correspond to l = - (L - 1) and l=0, respectively.
At a fixed level j, the function $f(t)$ is represented by

$$f(t) = S_j f(t) + \sum_{l=-(L-1)}^{j} D_l f(t) . \tag{7}$$

A discrete signal $f(t)$ can thus be expressed as a wavelet expansion by orthonormal basis

---

[1] $\langle f, \phi_{l,k} \rangle$ is the inner product: $\langle f, \phi_{l,k} \rangle = \int_{-\infty}^{\infty} f(t) \phi_{l,k}(t)\, dt$

functions derived from the two related functions: scaling function $\phi(t)$ and the wavelet $\psi(t)$. The above expansion (*Eq.* 7) means that scaling and translating $\phi(t)$ and $\psi(t)$ leads to an orthogonal basis for the analysis of signal. In such way *f(t)* is decomposed into a smoothed version $S_j f(t)$ obtained by applying the low-pass filter ϕ and a sum of the details (D_j) obtained by the high-pass filter ψ.
The relationship between the representation of *f(t)* at level *j* and that at level (*j* - 1) is summarized by

$$S_{j-1}f(t) = S_j f(t) + D_j f(t). \tag{8}$$

Figure 2 shows the recursive scheme, usually called a pyramid algorithm, used to calculate the wavelet coefficients from the finest level to a chosen level *j*.
The multi-resolution analysis is obtained by applying the inverse wavelet transform to the coefficients of each level.

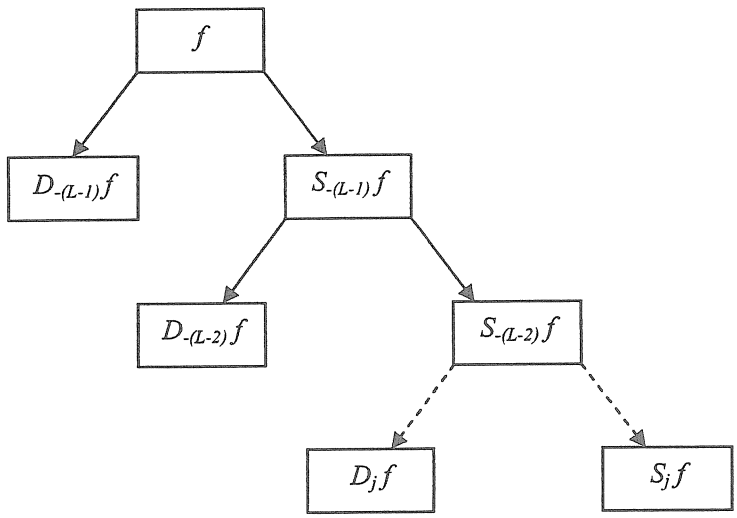

Fig. 2: Recursive scheme used to calculate the wavelet coefficients of a function *f* from the finest level -*L*+1 to a chosen level *j*

The advantage of analysing a signal with wavelets is that it enables local features of the signal to be studied with a detail matching their characteristic scale. In the temporal domain, such a property allows transient signals to be represented effectively [M.T. Carrozzo et al., 2002]. Thus it can be said that the DWT enables a *multi-resolution analysis* of a signal to be made.

CHOICE OF THE WAVELET BASIS

Different wavelet basis are obtained by varying the support width of the wavelet. Changes in the wavelet support in general affect the final frequency characteristics of the wavelet transform. Usually the amplitudes of the coefficients change and, consequently, the scale where the signal and noise separate also changes.
The choice of a wavelet basis could represent an open problem for filtering. Since it was impossible to test the filter effectiveness with statistical significance for all the wavelets available in the Matlab® software package, some criteria were used to make a preliminary selection of a set of wavelet bases.
Deighan and Watts (1997) and Grubb and Walden (1997) considered the compactness of the wavelet functions in the time and frequency domains as a useful parameter for choosing the best wavelet basis to solve a specific problem.

A criterion to evaluate the suitability of a wavelet of a specific shape to represent the signal is to determine how concise and localized its wavelet representation is.
The "maximum compactness" or "minimum entropy" criterion, which Coifman and Wickerhauser (1993) and Fedi and Quarta (1998) applied for data compression and data analysis, respectively, was used here in an attempt to optimize the choice of the wavelet basis.
In particular, this criterion was applied to the sequence available for this study, which spans from June to December 2005 and was acquired at one of the Etna's continuous gravity stations (PDN). To find the most appropriated support for our case the transform is repeated using different basis and Shannon's entropy of the analysed gravity sequence was then calculated. As underlined by the test carried out over 39 wavelet basis, it seems that the range of relative variability of the values calculated is more restricted only for a narrow number of wavelet basis and leads to the selection of a set of six wavelets: Symmlet 8, Bior 6.8, Daubechies 5-7-9, Rbio 2.8. The averages of the entropy values are shown in Table 1 for each tested basis of this small group.

Tab. 1: Table of the executed test showing the averages of the entropy values for each tested wavelet basis

Wavelet basis	Entropy
Symmlet 8	4.02
Bior 6.8	4.13
Daubechies 5	4.21
Rbio 2.8	4.22
Daubechies 7	4.27
Daubechies 9	4.37

DATA PROCESSING, COMPARATIVE TECHNIQUE AND RESULTS

Previous to the filtering analysis of the sequence at hand, acquired by LaCoste & Romberg PET 1081 at Mt Etna site, its spikes, gaps steps and large amplitude oscillations due to earthquakes events are corrected using T-soft, a graphical and interactive software developed by Van Camp and Vauterin (2005).
The signal from any continuous running gravity meter is affected by the tidal acceleration (Torge, 1989). In order to remove the Earth tides effect, the raw data are decimated to 1-h ordinates for a classical tidal analysis using the ETERNA3.4 software (ANALYZE, Wenzel, 1994). A RMS error on unit weight of 12 nm/s^2 was obtained, implying tidal residuals on the gravity signal up to 1-2 μGal peak-to-peak over the most relevant tidal families (diurnal and semidiurnal).
Continuously recording spring gravimeters are affected by aperiodic temporal variations in the display of the zero position called instrumental drift (Torge, 1989). To correct the data for the main effect of instrumental drift a best linear fit was removed from the sequence.
The gravity signal perturbations, due to the local pressure changes consist of two main effects: the upwards attraction of the air masses on the sensor of gravimeter, and the loading effect, due to the vertical displacement of the ground and the associated changes of potential. The linear pressure correction often leads to an obvious decrease of the RMS error of tidal gravity factors. Global pressure changes may also make contributions to the annual gravity signals, but these effects are difficult to model [Richter et al., 2004]. Moreover, the instrumental reactions to meteorological effects are very complex and can trigger large annual variations in the drift.
Through the optimization of an automatic one-dimensional algorithm, that enables the wavelet decomposition to be made, a multi-resolution analysis of the signal is obtained in Matlab® development environment.

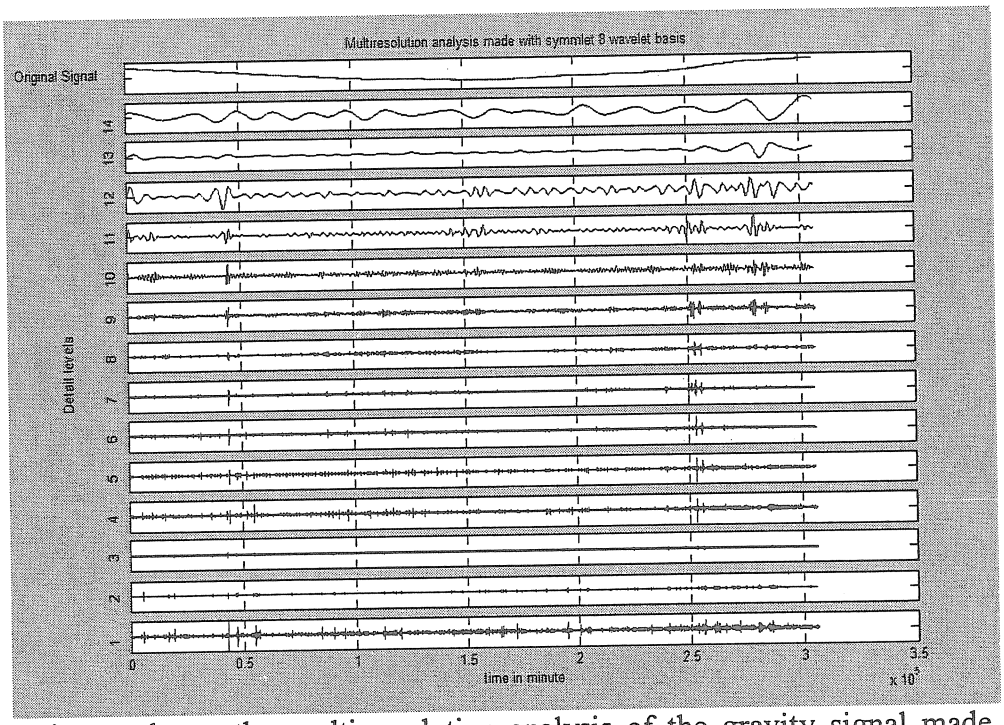

Fig. 3: The picture shows the multi-resolution analysis of the gravity signal made with Sym8 wavelet basis. The input signal is displayed at the top (red one).

Figure 3 shows an example of multi-resolution analysis of the continuous gravity sequence under discussion after the elimination of the tide and linear drift. It is performed using the wavelet basis Symmlet 8 (Daubechies, 1992). Since the gravity sequence consist of 308160 samples and the length of Symmlet 8 basis is 16, using the general criterion:

$$lev = (log(lx/(lw-1))/log(2))$$

where:
lev is the maximum allowed level decomposition;
lx is the length of the signal;
lw is the length of the wavelet basis;
the multi-resolution analysis contain 14 scales each containing 308160 samples. In such way the first scale (l = 1) has 16384 coefficients, the next (l = 2) contains 8192 coefficients and so on…; this adds up to 308160 numbers including the mean value of f (t). The original signal is thus obtained (as showed in the pyramid algorithm) with a summation of all the detail levels plus the approximation level (S_j) that is the long period content of the signal.
The multi-resolution analysis made with both detail and approximation levels allow local features of the signal to be studied in time domain and transient signals to be represented effectively. This is an important point since the continuous gravity signal could include some volcanic effects, which in time span from minute to years. The only way to check them is the correlation, in the time domain, with other geophysical or geochemical signal. On the other hand the approximation levels representation of the signal enables the separation of the long period component from the high frequency ones. In order to get a confrontation with the classical filtering method, the same component is thus obtained with both Chebyshev and Butterworth frequency filters with different cut off frequencies and polynomial orders. The figure 4 is an over-plot between the original signal and the two filtering methods. The wavelet filter is the only one fitting perfectly the general behaviour of the curve.

a)

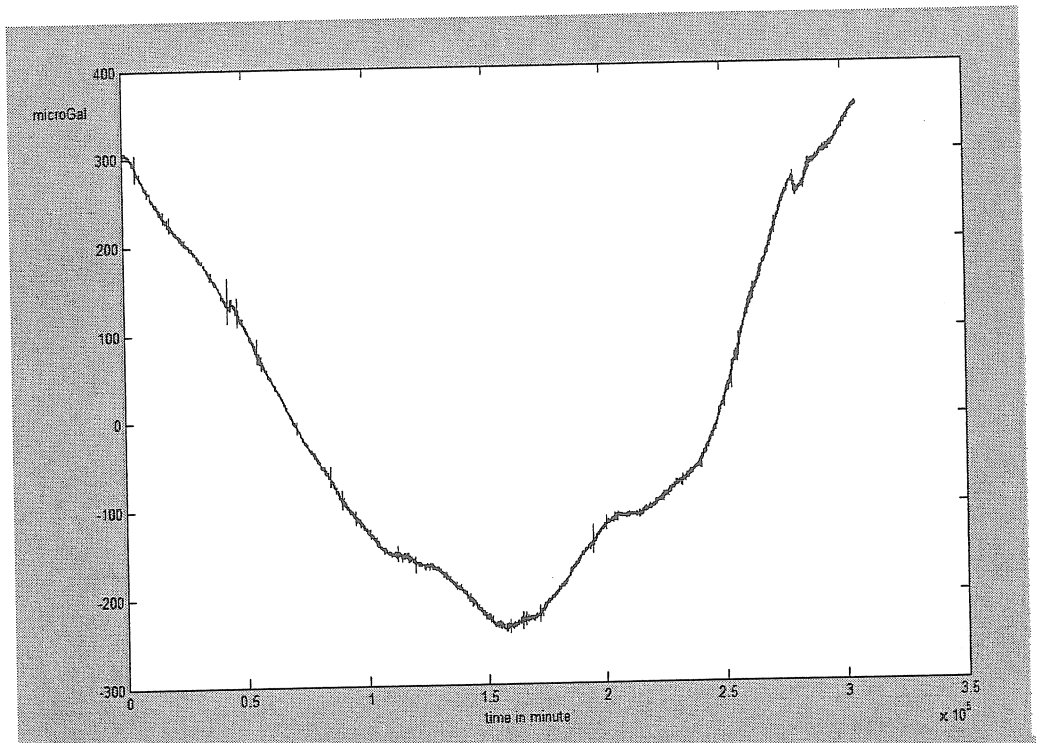
microGal
400
300
200
100
0
-100
-200
-300
0
0.5
1
1.5
2
2.5
3
3.5
time in minute
x 10^5

b)

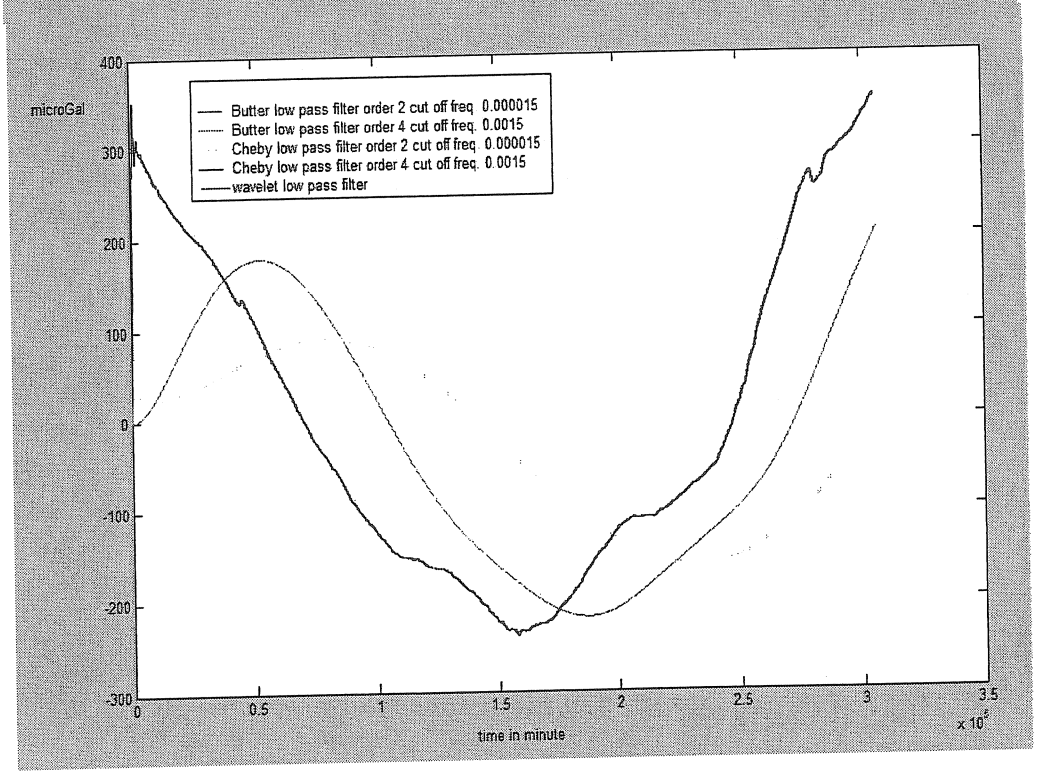
microGal
Butter low pass filter order 2 cut off freq 0.000015
Butter low pass filter order 4 cut off freq. 0.0015
Cheby low pass filter order 2 cut off freq 0.000015
Cheby low pass filter order 4 cut off freq. 0.0015
wavelet low pass filter
400
300
200
100
0
-100
-200
-300
0
0.5
1
1.5
2
2.5
3
3.5
time in minute
x 10^5

c)

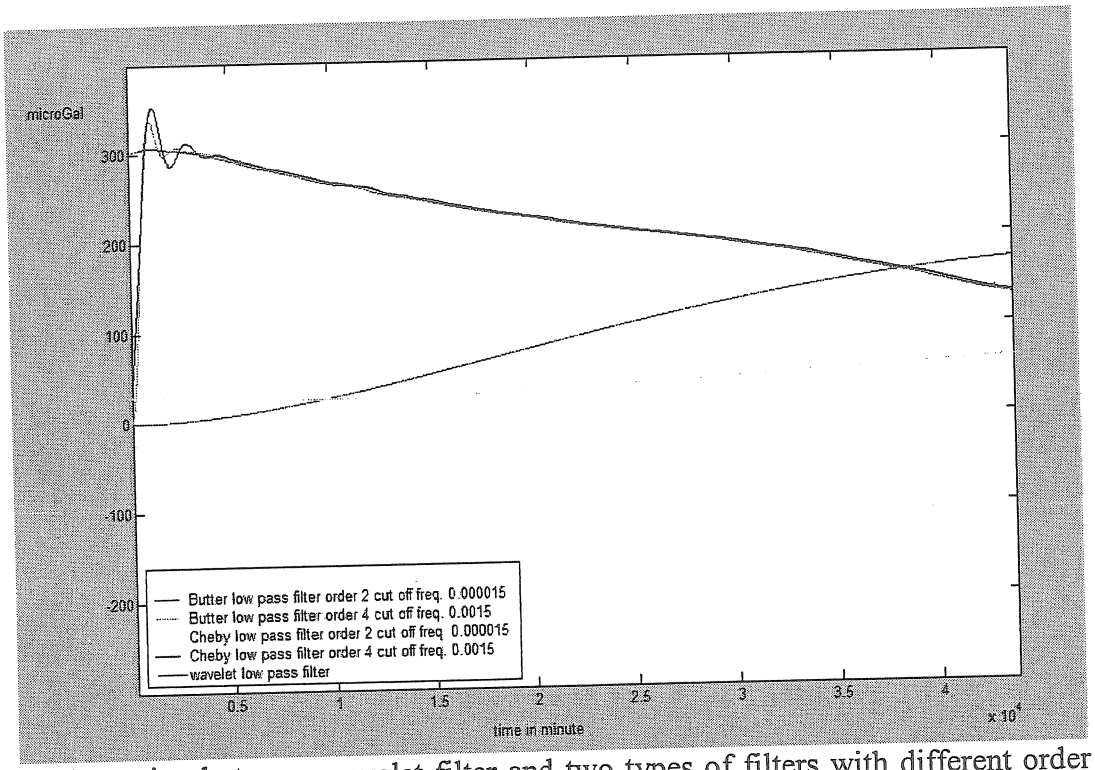

Fig. 4: Confrontation between wavelet filter and two types of filters with different order and cut off frequencies: a) on the top is displayed the original signal; b) global view of the different filtering method; c) zoom showing the edge effects;.

It seems that frequency domain filtering does not always work well because:

- Depending on both cut off frequency and filter order it also can introduce edge effects and distortions of the original signal;
- The frequency filters often leave some high frequency in the low pass filter, if we want to get a separation of the long period waves from the short ones;
- It globally removes frequencies causing a generalized smoothing effect that substantially broadens features of interest.

The long period signal obtained with the low pass filter performed by wavelet transform is more smoothed and without any significant edge effects. The same technique is then applied to the pressure, temperature and humidity signals, acquired at the same station, and the correlation analysis between the corresponding low frequencies component of the signals shows a strong anticorrelation with temperature (-0.7735) while the correlation with pressure and humidity are -0.5209 and -0.0896 respectively. Moreover, temperature and humidity signals show a correlation index of 0.5152. It seems that this long period component of the gravity sequence is a part of the annual oscillation due to the mainly influence of the seasonal temperature changes. Additionally, a cross-correlation analysis shows a time lag of about 40 days of the gravity signal with respect to the temperature changes (Fig. 5).

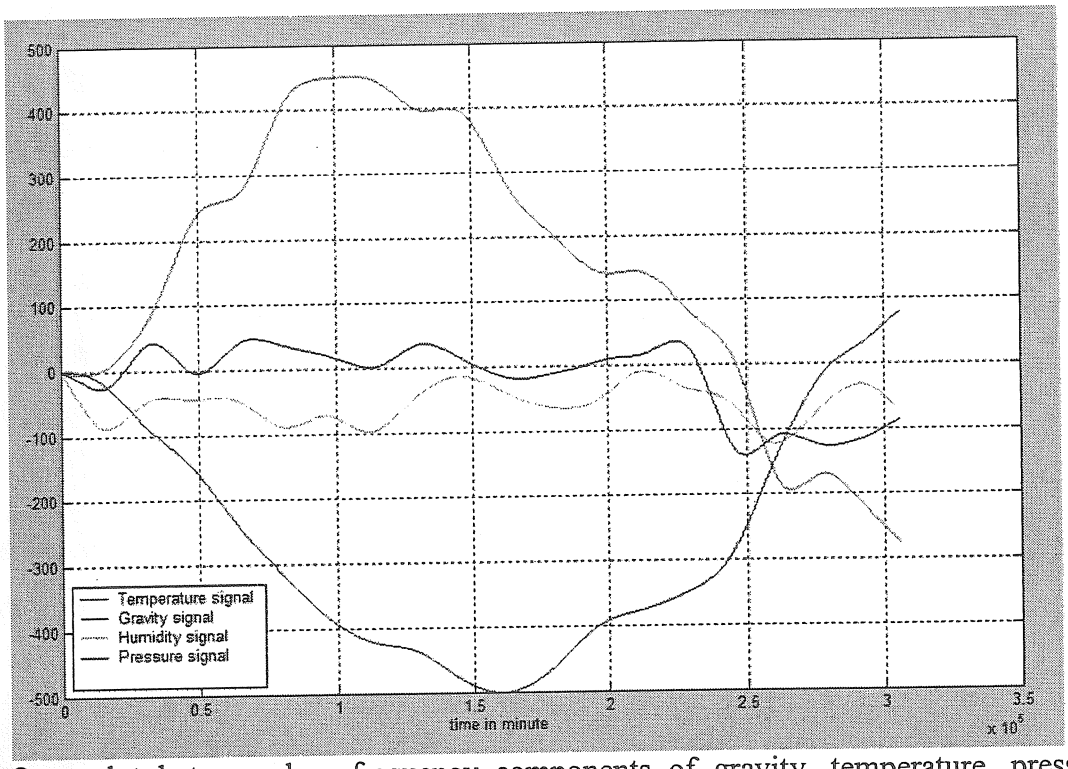

Fig. 5: Over plot between low frequency components of gravity, temperature, pressure and humidity signals. The figure shows the strong correlation and the time lag between temperature and gravity signal. In order to get the same scale, the temperature and pressure signals are multiplied by an amplification factor of 10.

The figure 6 shows the spectra of all signals obtained with the wavelet low pass filter. It shows how the wavelet filter works well since we have only low frequencies without high frequency signal. This kind of analysis clearly shows that the spectrum of each signal contain the same main components. The main peak around 200 days is the harmonic of annual period which is not resolved properly due to the insufficient time span.

It is thus more difficult to detect changes due to volcanic processes in the long period component of the signal, as this one is largely affected by the annual oscillations due to the meteorological parameters. Consequently, it is more suitable to analyze separately the low and high frequency parts of the signal.

Once the useful signal for our purposes has been suitably separated, the residuals can be used to evidence, over the time-interval considered, (i) recurrences in time (i.e. cyclic processes) and (ii) microgravity anomalies correlated with the ensuing volcanic activity (Fig. 7).

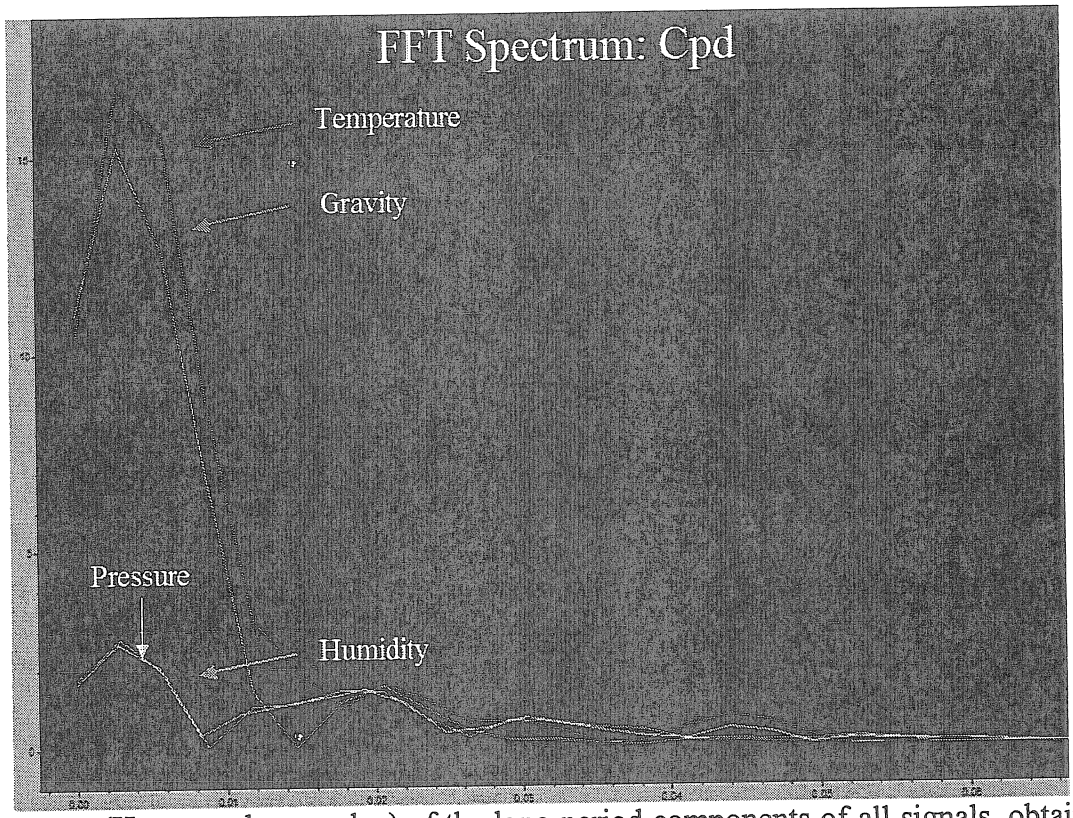

Fig. 6: Spectra (Hz vs cycles per day) of the long period components of all signals, obtained with the wavelet low pass filter. The figure shows that the filtered components contain only low frequencies.

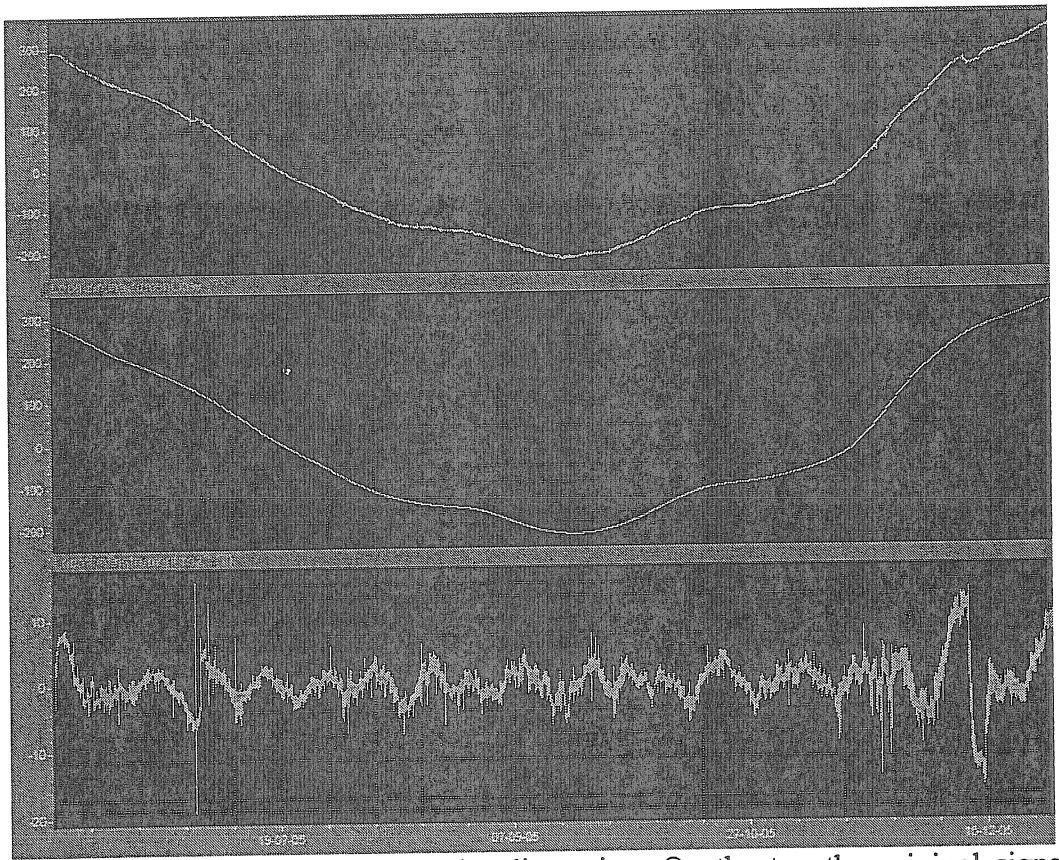

Fig. 7: Residues of the gravity signal under discussion. On the top the original signal, on the middle the low frequency component and on the bottom the high frequency one.

CONCLUSIONS

A new promising technique, for continuous gravity data noise-filtering based on "Wavelet transform", was proposed. The aim of this preliminary work is only an overview about wavelet transform with an application on the continuous gravity data.

The results obtained with wavelet decomposition seem to be better than the frequency domain filtering. The perturbations caused by the simultaneous action of different parameters (e.g. tide, instrumental drift, pressure, temperature and humidity) cannot be separated with frequency filters, since the spectrum of each component of various origins has wide intervals of superposition. The wavelet decomposition could be suitable for the construction of a non-linear multi-regression model that could enable a simultaneous correction of the main perturbing processes. Moreover, frequency domain filtering does not always work well because: (i) it globally removes frequencies causing a generalized smoothing effect that substantially broadens features of interest; (ii) depending on both cut off frequency and filter order it also could introduce edge effects and distortions of the original signal; (iii) it does not allow to study local features of the signal in the time domain.

Furthermore, the wavelet based filter does not require any tuning of parameters to produce results as good as the best achieved with frequency domain filters. This makes the process faster and more convenient. Finally, this paper stresses that the wavelet transform has others advantages over Fourier transform: multi-resolution decomposition and time-space localization, two important characteristics for denoising problems.

ACKNOWLEDGMENTS

S. Panepinto worked at the Royal Observatory of Belgium (ROB) during six months in the framework of the bilateral collaboration between ROB and Prof. D. Luzio of the University of Palermo, thanks to the economical support of the Italian Government (grant n. 76202 Università degli studi di Palermo). This project would not be possible without the collaboration between ROB and the Istituto Nazionale di Geofisica e Vulcanologia, Catania section.

REFERENCES

Budetta G., Carbone D., Greco F. and Hazel R., 2004. Microgravità Studies at Mount Etna (Italy). American Geophysical Union-Geophysical Monograph Series 143: 221-240.

Carbone D., Budetta G. and Greco F., 2003a. Possible mechanisms of magma redistribution under Mt. Etna during 1994-1999 period detected through microgravity measurements. Geophys. J. Int., 153: 187-200

Carbone D., Budetta G., Greco F. and Rymer H., 2003b. Combined discrete and continuous gravity observations at Mt. Etna. J. Volcanol. Geotherm. Res., 123:123-135

Carrozzo M.T., R. de Franco, L. De Luca, D. Luzio, R. Primiceri, T. Quarta and M. Vitale. Wavelet correlation filter for wide-angle seismic data. Geophysical Prospecting, 2002, 50, 547-564

Coifman R.R. and Wickerhauser M.V. 1993. Wavelets and adapted waveform analysis. A toolkit for signal processing and numerical analysis. Proceedings of Symposia in Applied Mathematics 47, 119-145.

Daubechies I. 1992. Ten Lectures on Wavelets. Society for Industrial and Applied Mathematics.

Deighan A.J. and Watts D.R. 1997. Ground roll suppression using the wavelet ttansform. Geophysics 62, 1896-1903.

El Wahabi A., Ducarme B., Van Ruymbeke M., d'Oreyè N. and Somerhausen A., 1997. Continuous gravity observations at Mt. Etna (Sicily) and Correlations between temperature and gravimetric records. Cahiers du Centre Européen de Géodynamique et de Séismologie, 14: 105-119.

Fedi M. and Quatta T. 1998. Wavelet analysis for the regional residual and local separation of the potential field anomalies. Geophysical Prospecting 46, 507-525.

Foufoula-Georgiou E. and Kumar P. 1994. Wavelets in Geophysics. Academic Press, Inc.

Grubb H.]. and Walden A.T. 1997. Characterizing seismic time series using the discrete wavelet transform. Geophysical Prospecting 45, 183-205.

Mallat S. 1992. Multiresolution approximation and wavelets. Transactions of the American Mathematical Society 315, 69-88.

Mallat S. 1999. A Wavelet Tour of Signal Processing. Academic Press, Inc.

Meyer Y. 1993. Wavelets Algorithms mid Applications. Society for Industrial and Applied Mathematics.

Percival D. B. and Walden A. T. 2002. Wavelet methods for time series analysis. Cambridge University Press

Warburton R. J. and Goodkind J. M., 1997. The influence of barometric-pressure variations on gravity. Geophys. J. R. Astron. Soc., 48: 281-292.

Detection of the Special Gravity Signals in Sub-tidal Band by Using a Wavelet Technique

H. P. Sun[1], W. D. Zheng[2], J. Q. Xu[1], H. Z. Hsu[1]

1. Institute of Geodesy and Geophysics, Chinese Academy of Sciences, Wuhan 430077, China;
2. Shanghai Astronomical Observatory, Chinese Academy of Sciences, Shanghai 20030, China;

Abstract

Based on the 5-year length of tidal gravity observations recorded with a superconducting gravimeter at Wuhan International Tidal Gravity Reference Station, the special gravity signals associated with the possible Earth's solid inner core translational oscillations in sub-tidal bands are studied by using for the first time a wavelet transformation technique. The analysis is conducted on tidal gravity residuals after removing the synthetic tidal gravity signals and air pressure perturbation from original observations, demonstrating that there exist gravity oscillation signals at 4~6 h bands with amplitude at the ngal (10^{-12}g) level. However, it is found that the frequency and amplitude of such kind of oscillation signals change with time, and the analysis shows that these oscillation signals are provoked probably by some non-continuous source with very low amplitude.

BIBLIOGRAPHY

H. P. Sun, W. D. Zheng, X. L. Ding, Wu Chen, X. D. Chen (2006): Detection of the special gravity signals in sub-tidal band by using wavelet technique. Chinese Science Bulletin, 51, 6, 713-722

Volcanic activity and tidal heating of Saturn's moon Enceladus

P. Varga

Geodetic and Geophysical Research Institute,
Seismological Observatory,
Budapest, Meredek u. 18 H-1112, Hungary
(varga@seismology.hu)

1. Preliminary statements concerning dynamics of Enceladus

The medium size, spherical satellites of Saturn turned in synchronized rotation in the early stage of their history, what means their orbital and rotation periods are the same. Consequently their tidal bulge has no motion in a coordinate system fixed to the body of the moon, therefore there is no tidal friction influencing the axial rotation spin and dynamical processes on and within the celestial object. This passivity disappears however if the orbit is locked in the resonance between the orbital periods of members of the satellite system. This resonance generates a forced eccentricity which leads to temporal variation of the tidal bulge due to central body of the system. Enceladus is one of the innermost moons of Saturn. The most remarkable types of tectonic features found on Enceladus are faults that can run up to two hundred kilometres long, which cross older, tectonically deformed formations. The origin of these global linear structures should be related to tidal activity generated by the Enceladus-Dione 2:1 resonance. Tidal heating is resulting perhaps also from this orbital resonance with Dione, which powers the water volcanism imaged by Cassini spacecraft in 2005.

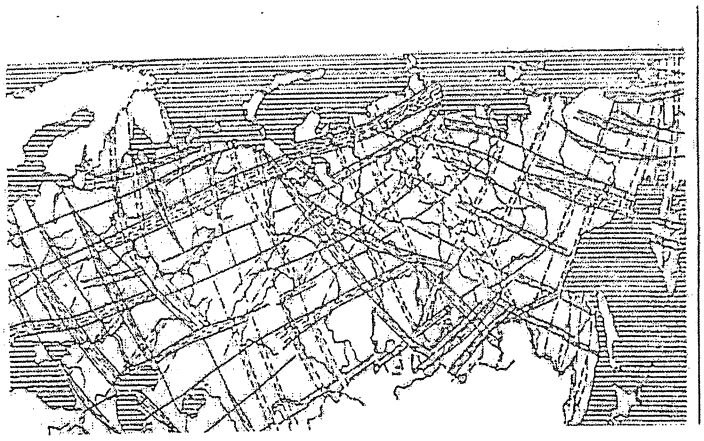

Fig.1. Distribution of linear structures on the surface of the Earth

Fig. 1 shows lineaments detected on the Earth over the former USSR with the use of satellite telemetric investigations during eighties of XXth century. (*Brjukanov et al.,*

1984). These structures, which were found in other parts of the Earth too, have regular distribution over the planetary surface and possibly are related to despinning of axial spin. Similar fault-lines are visible on the surface of Enceladus (Fig.2) what can be in principle also associated to resonance supported tides of Enceladus.

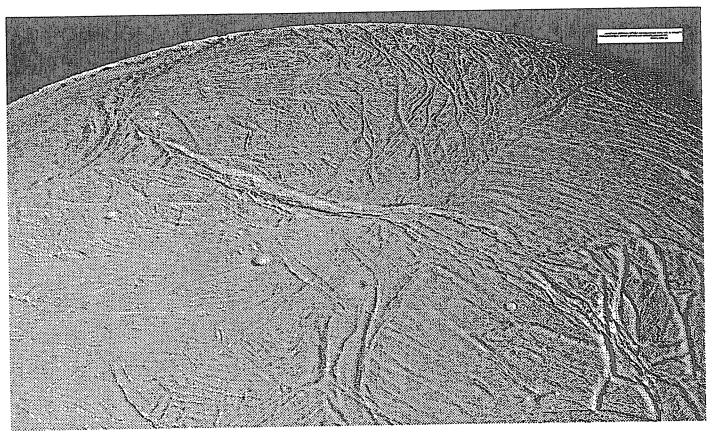

Fig.2. Distribution of linear structures on the surface of the Earth

The aim of investigation carried out by the author is to model contribution of the tidal phenomenon in dynamics of Enceladus. The mathematical modelling of the tide generated normal (radial) and tangential (tangential) distribution in the icy "mantle" of Enceladus was carried out. With the use of these results the magnitude of tidal heating was estimated.

2.Description of elastic deformations of spherical body

The stresses produced by tidal forces were studied by inhomogeneous differential equations of elasticity for a gravitating globe, which are generally used in earth tidal research. Elastic deformations in this system can be characterised by dimensionless functions of Love and Shida: $H(r)$ describes the vertical, $T(r)$ the horizontal displacements and $R(r)$ gravitational potential associated with elastic deformation. $\mu=\mu(r)$ and $\lambda=\lambda(r)$ are the Lamé parameters, $\rho=\rho(r)$ is the density at a r distance from the centre. $W=W(r)$ describes the gravity potential, while n is the degree of spherical harmonics and G is the gravitational constant. If the notation system introduced by *Molodensky (1953)* is in use the corresponding differential equations are:

$$-\left[\mu\left(T'+H-\frac{2}{r}T\right)\right]' = \rho\left(R+W'H\right)' + \lambda F + 2\frac{\mu}{r}\left[2H+T'-\frac{n^2+n+1}{r}T\right]$$

$$-(\lambda F+2\mu H')' = \rho(R+W'H)'-\rho W'F+4\frac{\mu}{r}\left(H'-\frac{H}{r}\right)-\frac{n(n+1)}{r^2}\mu\left(T'+M-4\frac{T}{r}\right)$$

$$R'' = -\frac{2}{r}R'+\frac{n(n+1)}{r^2}R+4\pi G\left(\rho F+\rho' H\right)$$

$$F = H'+\frac{2}{r}H-\frac{n(n+1)T}{r^2}$$

(All differentiations (′) are carried out with respect to the radius r)

From among the six boundary conditions three refer to the surface ($r=a$). By the definition of elastic theory of tidal deformations $N(a)=M(a)=0$. At the core boundary $r=b$ $N(b)$ is equal to the hydrodynamic pressure and the value of $M(b)$ depends on the structure of the core.
To determine the normal (radial) and tangential (horizontal) stresses the following auxiliary relations are valid

$$N = (\lambda + 2\mu)H' + \lambda\left[\frac{2}{r}H - \frac{n(n+1)}{r^2}T\right]$$

$$M = \mu\left(T' - \frac{2}{r}T + H\right)$$

3. Model of Enceladus used for aims of present investigation

The data listed in Table 1 show characteristics of Saturnn's moon Enceladus.

Table 1. Characteristics of Enceladus (*Porco et al, 2006*)

Orbital characteristics	Physical characteristics
Semimajor axis (R_E): $2.37948\cdot10^8$ m	Mean radius (a_E): $2.521\cdot10^5$ m
Eccentricity(e_E): $4.5\cdot10^{-3}$	Mass (M_E): $1.08\cdot10^{20}$ kg
Orbital period (T_E): 1.3702 day	Volume: $6.712\cdot10^{16}$ m^3
Mean surface temperature: 75 K	Mean density(ρ_E): 1610 $kg\cdot m^{-3}$
(Mass of Saturn (M_s): $5.68\cdot10^{26}$ kg)	Surface gravity: 0.078 $m\cdot s^{-2}$

If the physical parameters of Enceladus and another significant Saturn moons (Mimas, Thetys, Dione, Rhea, Titan, Hyperion and Iapetus) are compared it turns out that the Enceladus has a relatively high average density (see Table 1). It means that due to the fact that his surface is composed by water ice Enceladus should have an inhomogeneous inner structure with a denth core. For the purpose of present study a two layered somewhat arbitrary selected model was used:

- „icy" mantle $1\geq r/a>0.55$
- „rocky" core $0.55\geq r/a\geq 0$

The physical parameters of such an artificial model of Enceladus are described in Table2.

Table 2. Physical properties of the model

	Mass (kg)	Volume (m^3)	Density ($kg\cdot m^{-3}$)	μ GPa	λ GPa
„icy" mantle	$6.15\cdot10^{19}$	$5.59\cdot10^{16}$	1100	5	5
„rocky" core	$4.64\cdot10^{19}$	$1.12\cdot10^{16}$	4150	20	20

In the above model the Lame parameters are taken equal ($\mu = \lambda$) and the effect of increasing hydrostatic pressure along the radius was not taken in consideration. The numerical solution of the sixth order differential equation in case of $n=2$ for the auxiliary functions (expressed in relative units) within the "icy mantle" gives auxiliary functions $M_2(r)$ and $N_2(r)$ in the form shown in Fig. 3.

Fig. 3. Distribution of the auxiliary functions $M_2(r)$ and $N_2(r)$ within the mantle

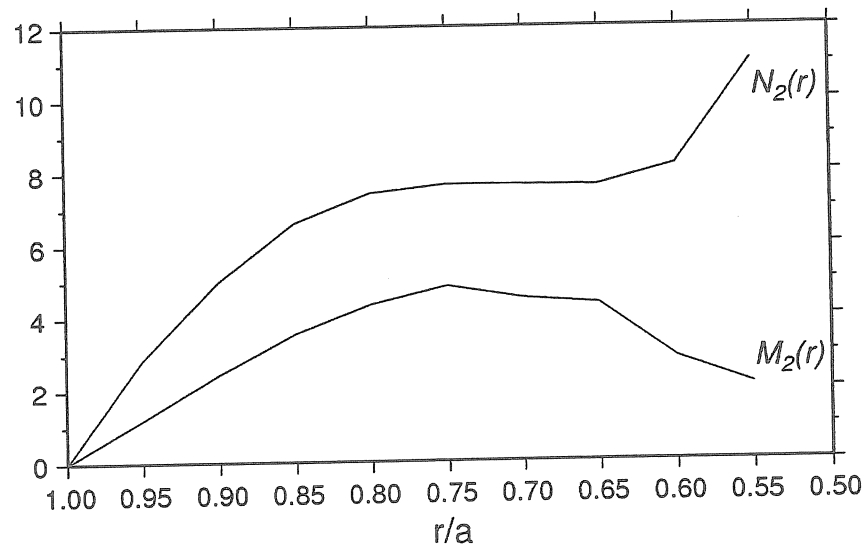

The experience of the study of very different models of the Earth shows, that the general trend remains similar for essentially different models of the mantle in case when the depth of the core-mantle boundary remains the same (*Varga, 1985, 1988, 1992*). If the core radius decreases (i.e. in case of reduced inhomogenity of the planetary body) the relative maximums of $N_2(r)$ and $M_2(r)$ are displaced to the deeper parts of the mantle.

4. Tidal heating of Enceladus

Due to synchronous rotation of Enceladus the tidal bulge varies only due to forced eccentricity caused by 2:1 orbital tidal resonance with Dione. The corresponding variation of second degree tidal potential can be given with equation

$$\Delta W_2 = \frac{G \cdot M_S \cdot a_E^2}{R_E}\left(\frac{3}{2}\cos^2\Psi - \frac{1}{2}\right)\left(\frac{r}{a_E}\right)^2 \frac{2e_E}{(1-e_E)R_E}$$

The normal and tangential second degree tidal stresses can be expressed with the use of auxiliary functions $N_2(r)$ and $M_2(r)$ (Fig. 3)

$$\sigma_N(r) = N_2(r)\frac{\Delta W_2(r)}{g_E \cdot r^2}\cdot\left(\frac{r}{a_E}\right)^2$$

$$\sigma_M(r) = M_2(r)\frac{\partial(\Delta W_2(r))}{\partial\Psi}\cdot\frac{1}{g_E \cdot r^2}\cdot\left(\frac{r}{a_E}\right)^2$$

The stress generated energies E_N or E_M in a volume $V(r)$ can be obtained with

$$E(r) = \frac{\sigma(r)}{2\mu} V(r)$$

Results of calculations carried out are plotted on Fig. 4.
It can be concluded that most of tidal energies are concentrated in the middle of the somewhat arbitrary chosen mantle. It is so - independently from the selected model - because of features of $N_2(r)$ and $M_2(r)$ (Fig. 3) and due to $\left(\frac{r}{a}\right)^2$ in expression for the tidal potential. This energy concentration in the middle of the mantle can be illustrated by the distribution of focal depths of quakes of the Moon (*Nakamura, 1983*).

Fig. 4. Energy due to tangential (E_M) and normal (E_N) stress within the mantle

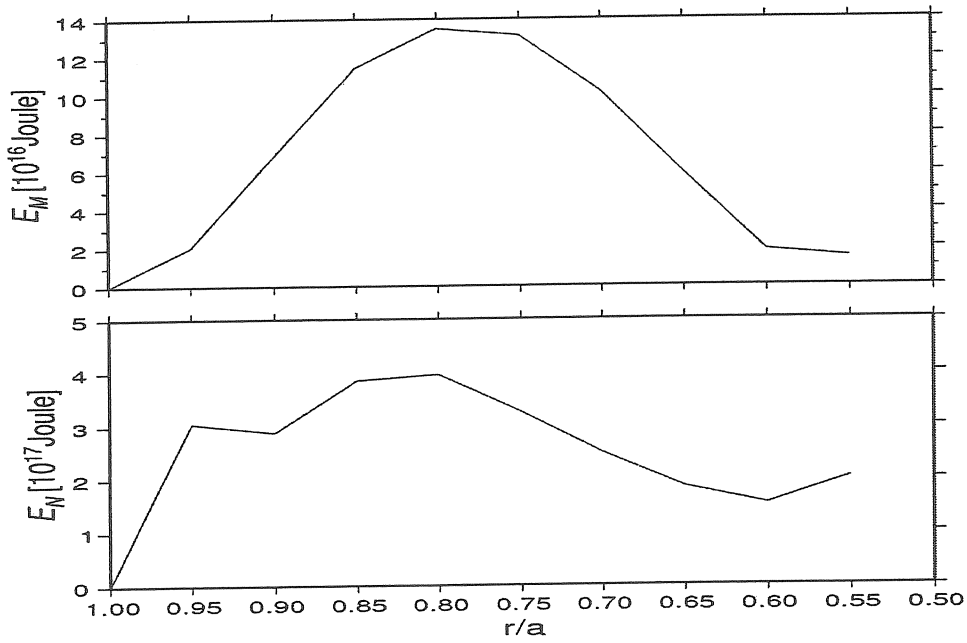

For energy dissipation within the Enceladus (M_E=*1.08·10^{20} kg*) one gets

$$-\left[\frac{dE}{dt}\right]_E = J \cdot \sigma \cdot K \cdot M_E$$

Here J is the mechanical equivalent of heat (*=4.182 Joule*), σ expresses the specific heat (*≈0.2*). To calculate the warm up K (in *degree/s*) we got for dissipation from $\Delta E \approx 10^{17}$ *Joule* and ΔT=*1/2 T_E= 0.6851 day*

$$-\left[\frac{dE}{dt}\right]_E = 8.4 \cdot 10^{11}\, Joule/s.$$

This way for the warm up we got *K=1.4·10^{-8} degree/s*. This means that during *300-350 year* the temperature enlargement in the "middle mantle" can be *≈200Kelvin.*
(For a comparison for the Earth *K=1.4·10^{-16} degree/s* i.e. *3Kelvin* during *10^9 year*)

5. Tidal friction due to irregular axial rotation along eccentric orbit.

Applying Kepler's third law to the Saturn_Enceladus system orbital velocity of Enceladus in case of circular motion is

$$n_E = \sqrt{G(M_S + M_E)a_E^3}$$

In case when the axial rotation is syncronized $\omega_E = n_E$
and due to the forced eccentricity caused by Dion the magnitude of orbital speed variation is

$$\Delta n_E = 2G^{1/2}(M_S + M_E)^{1/2} a_E^{3/2}\left[1-(1-e_E^2)\right]^{3/4}$$

$\Delta n_E \sim 10^{-3}$ °/s
This means that the librational motion of Enceladus on ist orbit around Saturn (Fig. 5) is ±8.6°.

Fig.5. Librational motion of Enceladus

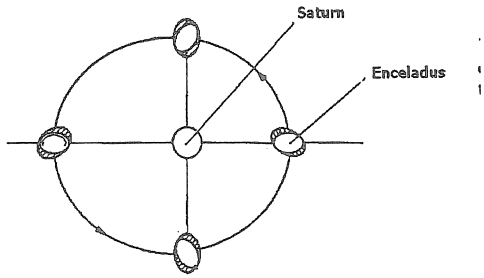

This motion produces an additional heating independently from the inner structure of Enceladus. The amount of heating generated in this way will be discussed in a future contribution.

5. Conclusions.

The tidal stresses and energies as it is shown by earlier model calculations for a spherical non-rotating, elastic and isotropic Earth are generated chiefly in the middle part of the s mantle. This conclusion holds in case of another bodies of the solar system too. This circumstance allows extend the traditional field of earth tide studies to the problems of planetology. By definition tidal stresses are equal to zero both at the surface and the centre of celestial bodies: at the planetary surface $N(r)=M(r)=0$ while at the centre the tidal potential $\Delta W=0$.

The tidal heating can warm up and melt the inner part of the Enceladus at the depth interval 15-160 km. This way, the fountain-like plumes detected by the Cassini mission can be explained. In case of reduced of reduced inhomogenety (expressed in lower mean density values), the tide generated heat moves to the deeper parts of

the moon. Possibly that is the reason why in case of other moons ofSaturn there is no similar volcanic activity observed.

Tidal friction due to irregular axial rotation along eccentric orbit can be an another source of tidal heating, which needs further investigations.

Acknowledgements

The research described in this contribution was realized in the frame of German-Hungarian bilateral project "Investigation of geodynamical processes by means of Liouville equation" supported by the Deutsche Forschungsgemeinschaft and by the Hungarian Academy of Sciences. The Hungarian project participants appreciate support of the Hungarian Science Foundation (Project: OTKA K60394).

References

Brjukanov et al., 1984. Cosmogeological map of the USSR of the scale 1 : 2 500 000. Paper presented at the 27th International Geological Congress, Section C 18, Nauka, Moscow.

Molodensky M.S., 1953. Elastic tides, free nutations and some problems of the Earth's structure. Trudi Geophys. Inst., 19 (146), 3-52.

Nakamura Y., 1983. Seismic velocity structure of the lunar mantle, J. Geophys. Res., 88, 677-686.

Porco C.C. et al., 2006. Cassini observes the active south pole of Enceladus. Science, 311, 10 March, 1393-1401.

Varga P., 1985. Influence of external forces on the triggering of earthquakes, Earthq. Predict Res., 3, 191-201.

Varga P. and Denis C., 1988. A study of the variation of tidal Love numbers with Earth structure., Geophys. Transact., 34, 4, 263-282.

Varga P., 1992. Stresses of lunisolar origin acting at the core mantle boundary. Manuscripta Geodetica, 17, 351-355.

PLANS FOR GRAVIMETRIC MEASUREMENTS AT JOZEFOSLAW OBSERVATORY

Marcin Barlik, Janusz Bogusz, Tomasz Olszak

Institute of Geodesy and Geodetic Astronomy, Warsaw University of Technology

1. INTRODUCTION

Installations of the absolute gravimeter FG5 No 230 in Astro-Geodetic Observatory at Jozefoslaw in June 2005 gave the possibility for the continuation of the gravity behaviour monitoring. The previous investigations were performed using ballistic (symmetric) gravimeter ZZG, constructed in Poland. The paper presents results of semi-annual interval of determinations of the gravity and geophysical phenomena appeared in non-tidal frequency bands. At the laboratory the tidal gravity measurements have also been performed since 2002 using LC&R ET-26 gravimeter. This elaboration also deals with the results of three and a half years cycle of gravimetric tidal observations adjustment. It also presents the influence of the environmental parameters (seasonal loading effects induced by air pressure and ocean, surficial water table, soil moisture and the rainfall as well) to the gravity changes.

2. GRAVIMETRIC LABORATORY

In 1996 Polish State Committee for Scientific Research decided to assign the founds for a new building of the Observatory. The construction ended in 2000. Several scientific laboratories were established and one of them was gravimetric laboratory placed in the Observatory's cellar, 6 m depth mostly to avoid microseimses (fig. 1).

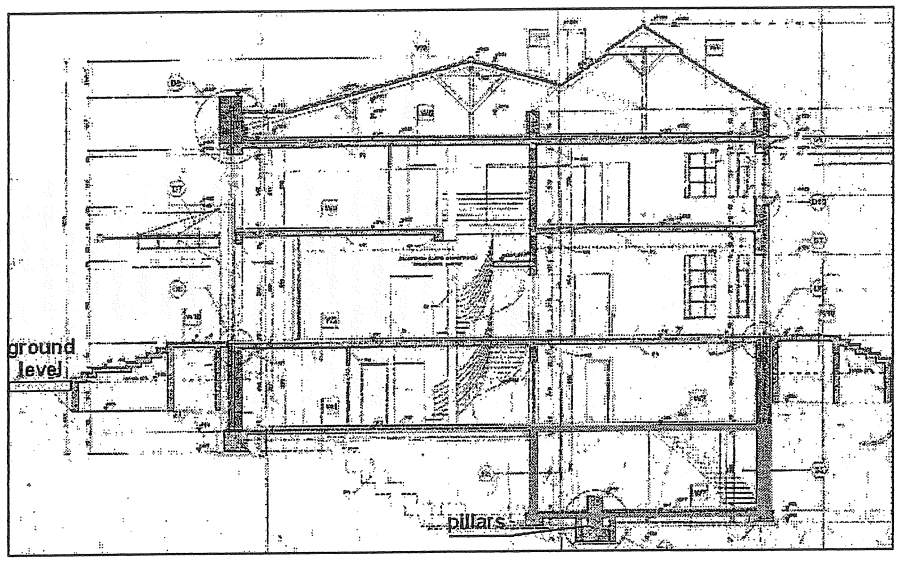

Fig. 1. Gravimetric laboratory at Jozefoslaw Observatory.

3. TIDAL GRAVITY MEASUREMENTS

Continuous tidal gravity measurements have been conducted since January 2002 using LaCoste&Romberg ET-26 gravimeter. The instrument is placed in the electronically controlled thermal chamber, sampling rate is one minute with the time stability controlled by Internet. The data stored from 2002 are presented in fig. 2.

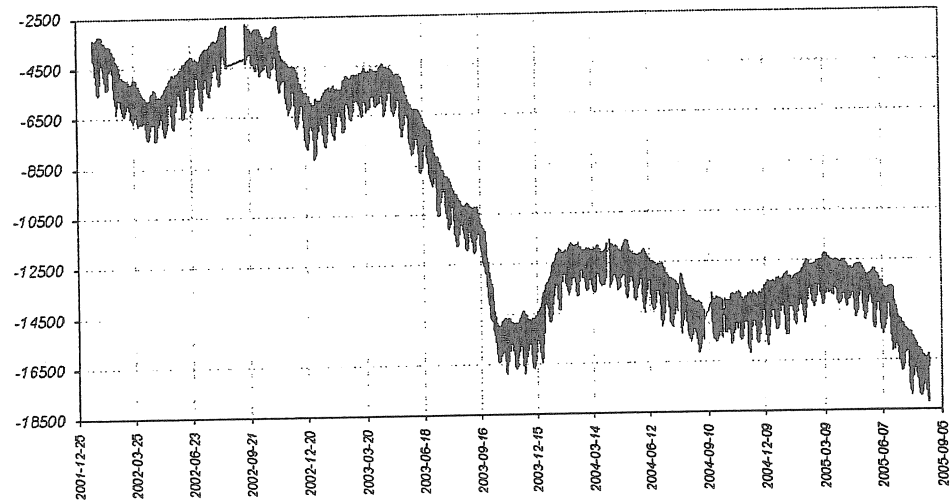

Fig. 2. Tidal data [nm/s^2].

The data adjustment of this data was made using ETERNA v. 3.4 (Wenzel, 1996). It shows that the accuracy is 8.4 nm/s^2, but if we divide the data into one-year blocks we obtained:
$m_{0\ 2002}$ = 4.4 nm/s^2, $m_{0\ 2003}$ = 4.5 nm/s^2, $m_{0\ 2004}$ = 4.6 nm/s^2, $m_{0\ 2005}$ = 2.3 nm/s^2.
These accuracies are not comparable to the accuracies of superconducting gravimeters, but we have to point out that these observations are the most precise that were ever carried out in Poland. The results of tidal data adjustment are presented in fig. 3 and 4.

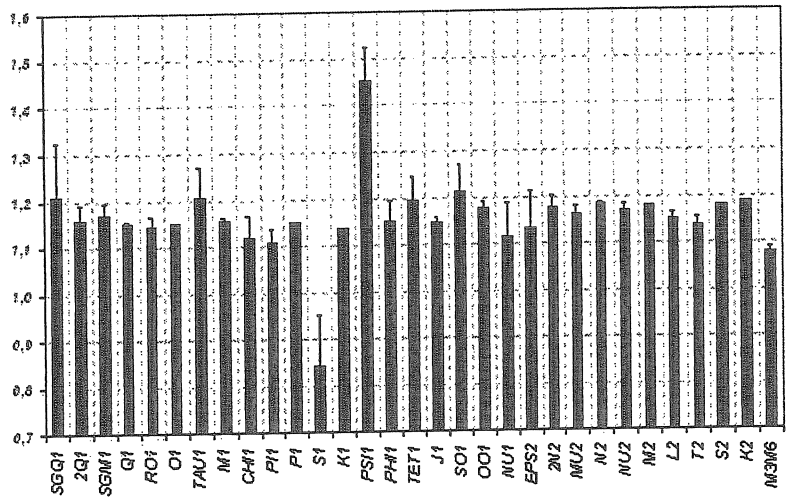

Fig. 3. Amplitude factor.

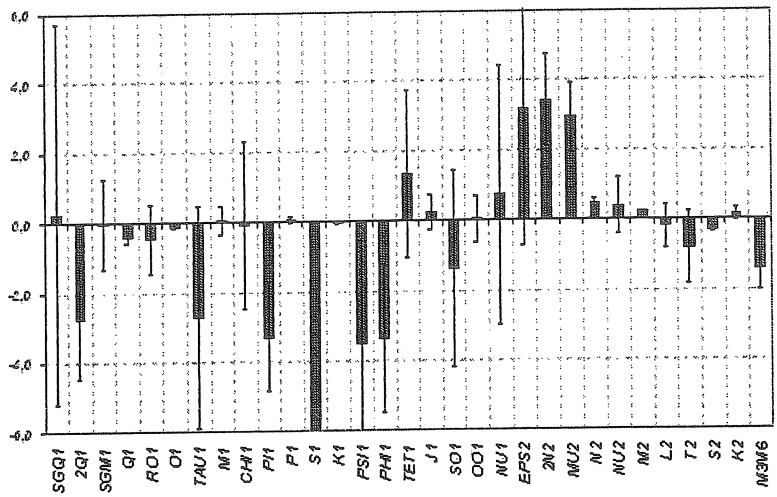

Fig. 4. Phase shift [°].

4. ABSOLUTE GRAVITY MEASUREMENTS

The absolute gravimeter FG5 No. 230 has been installed at Jozefoslaw observatory in June 2005.

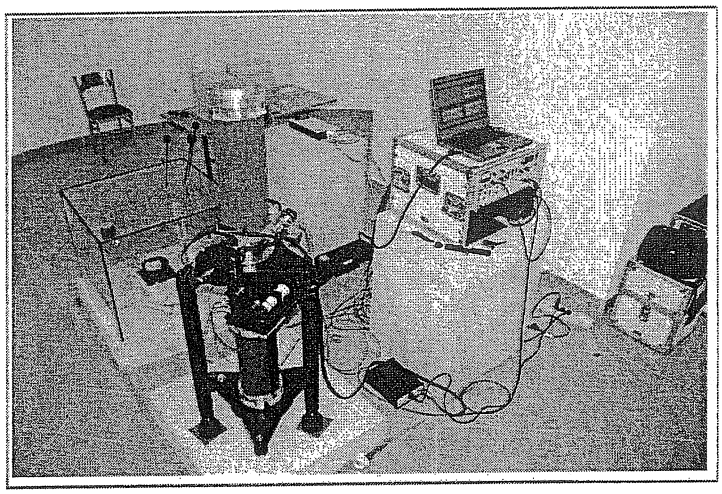

Fig. 5. FG5 No 230 gravity meter in Jozefoslaw.

From this time the repeated gravity measurements regularly once a month have started. Standard procedure of measurement embraces 24 hours cycle with 24 sets. Typically g value is obtained from 2400 drops. Gravity station in Jozefoslaw Observatory offers good stability, so precision of a single drop is ca. 7 - 8 μGal. This precision makes possible to obtain 2 μGal precision of final g value, with about 1 μGal set scatter.
The raw values of g are corrected by:

- elastic earth tides (ETGTAB procedure) with common standard coefficients;
- barometric effect;
- polar motion influence;
- ocean mass loading;

and referred on 100 cm level above pillar. The changes of gravity are presented in fig. 6.

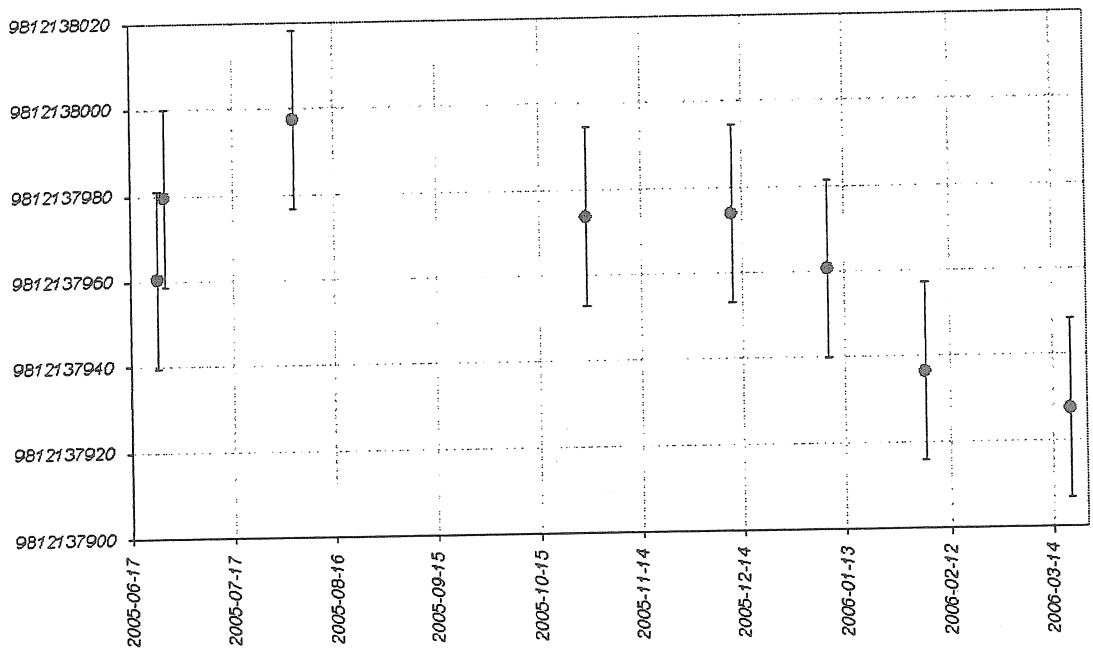

Fig. 6. Changes of gravity [nm/s^2].

5. SUPPORTING OBSERVATIONS

Together with the gravity changes we monitor and determine influence of the environment. The following supporting observations are conducted:

- ambient pressure, temperature and humidity;
- soil moisture;
- rainfalls;
- ground water table;
- snow coverage.

5.1. Ambient pressure, temperature and humidity

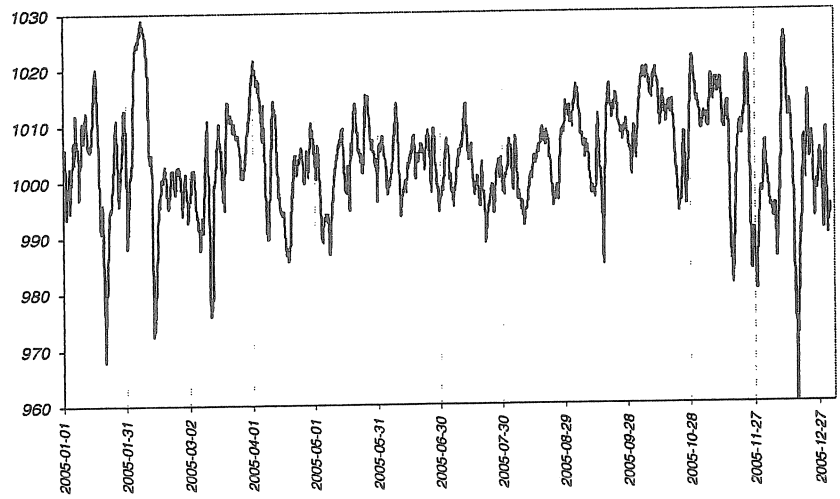

Fig. 7. Changes of ambient pressure [hPa] in 2005.

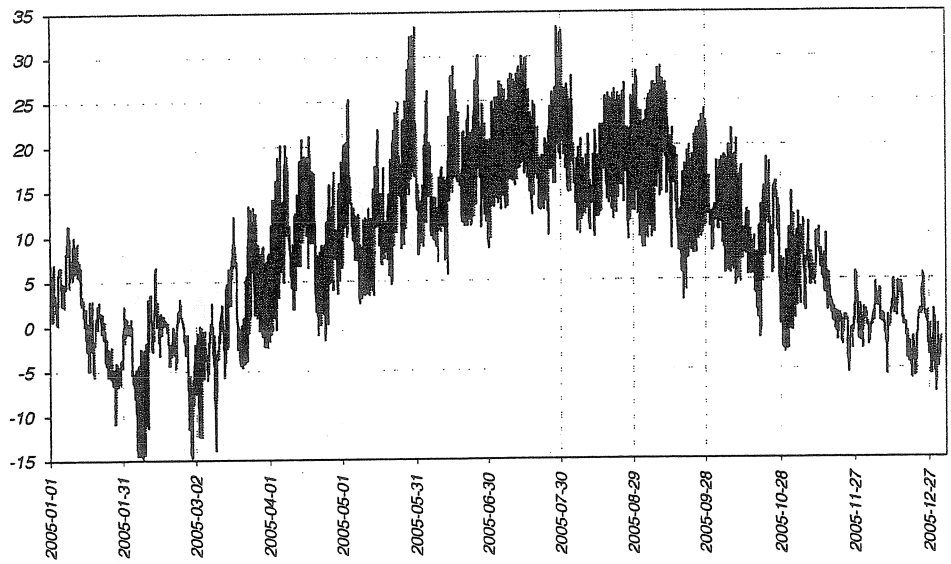

Fig. 8. Changes of ambient temperature [°C] in 2005.

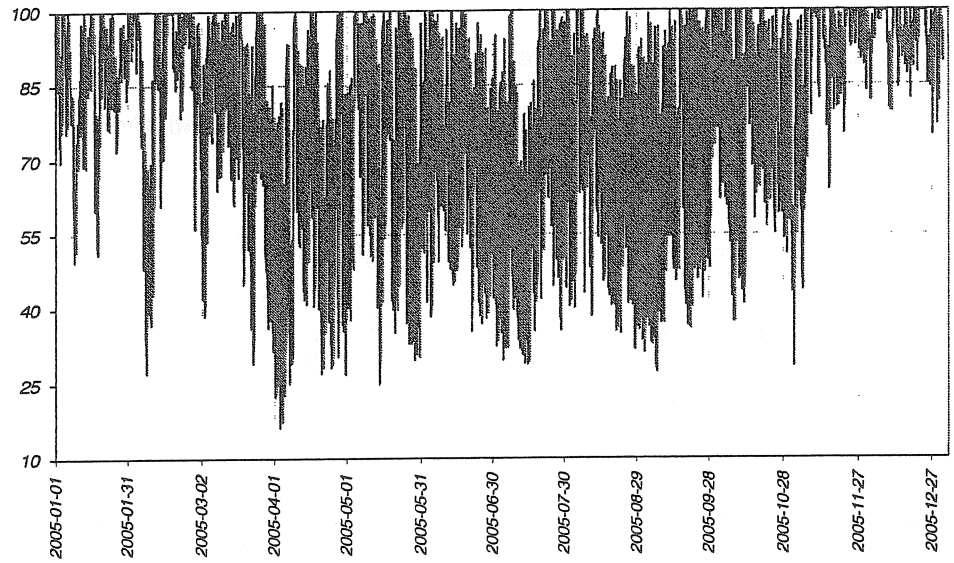

Fig. 9. Changes of ambient humidity [%] in 2005.

The effect of the atmospheric influence to the gravity calculated using single regression coefficient determined in previous researches (Bogusz, 2000):

$$\begin{aligned} \Delta g\left[nm/s^2\right] &= -3.450 * \Delta p[hPa] \\ \Delta u[mm] &= 0.3575 * \Delta p[hPa] \end{aligned} \tag{1}$$

are presented in fig. 10.

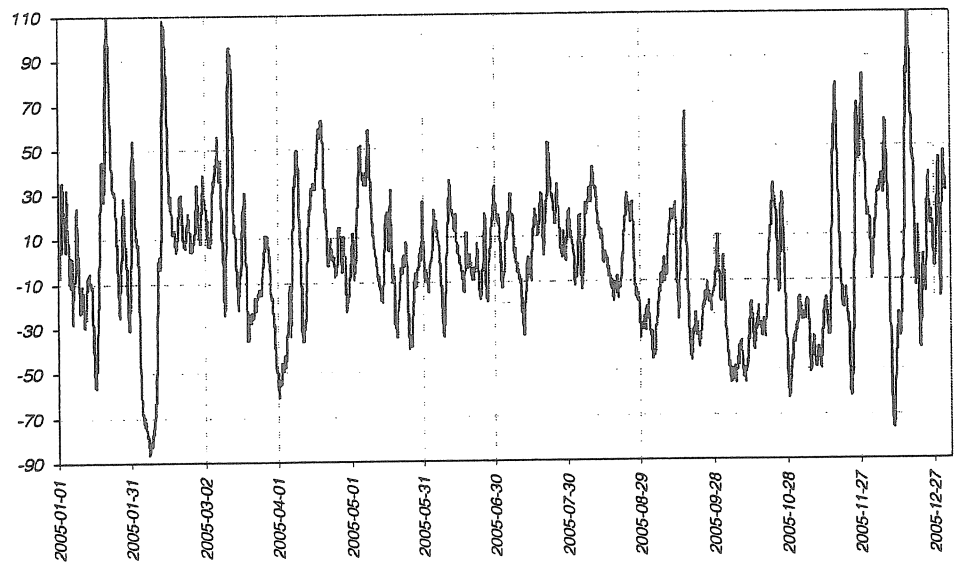

Fig. 10. Changes of atmospheric gravity effect [nm/s^2] in 2005.

5.2. Groundwater level observations

The ground at the Observatory is composed mostly of the sand and clay (fig. 11).

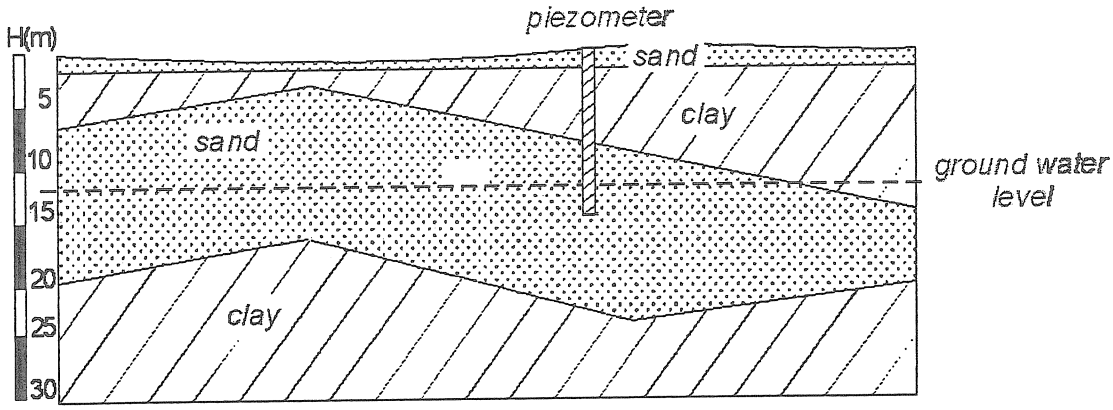

Fig. 11.

This is not very comfortable situation because clay keeps water. The piezometer to observe changes of water level is placed near the building of the Observatory to make the proper correction due to these changes. The fig. 12 presents the changes of the water table.

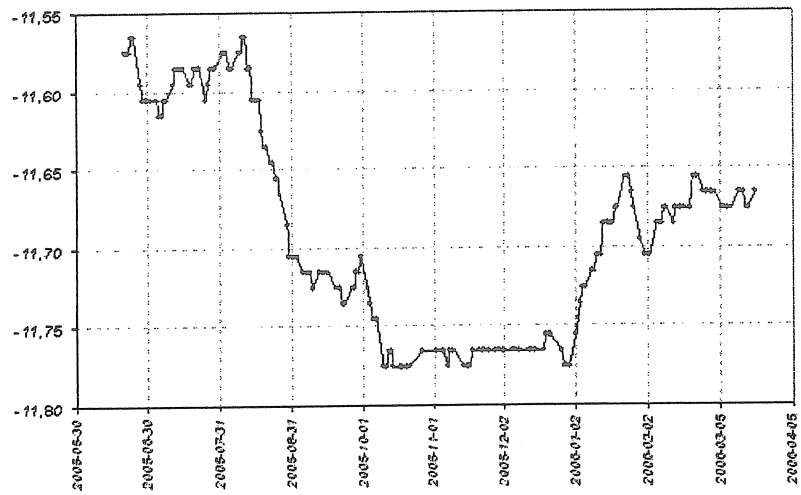

Fig. 12. Changes of the water table [m] observed in 2005.

Using the equation derived from the previous researches (Barlik at. al., 1989):

$$\Delta g\ [\mathrm{nm/s^2}] = 102.7 \cdot \Delta H\ [\mathrm{m}] \tag{2}$$

we obtained changes of the gravity due to water level changes (fig. 13).

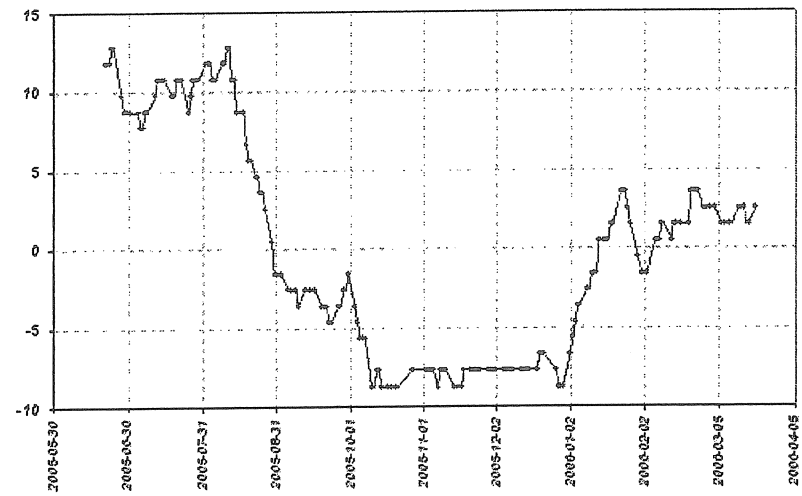

Fig. 13. Changes of the gravity [nm/s^2] due to the water level changes.

5.3. Soil moisture determinations

In 2005 we have made the test measurements of the soil moisture changes at two points at 0.5 m depth, which are presented in fig. 14. We plane to put in 2006 sensors to measure the soil moisture continuously.

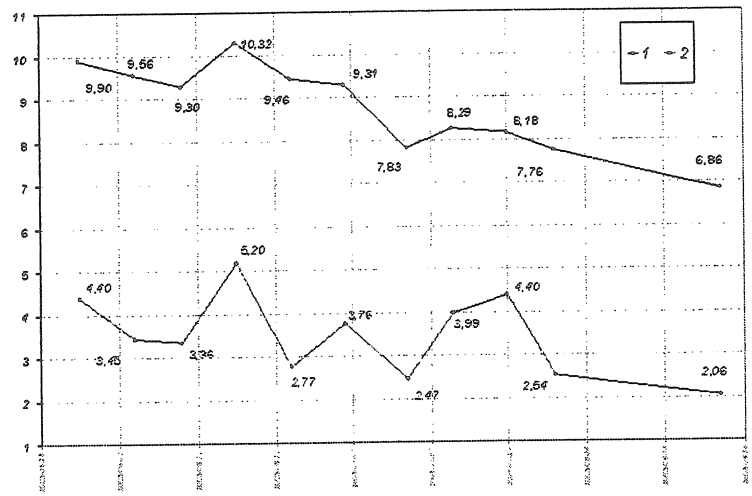

Fig. 14. Soil moisture changes [%] observed in 2005.

5.4 Changes of precipitation

In 2005 analog instrument for rainfalls measurements were put in the Observatory to make test measurements (fig. 15). We also plan to establish permanent recordings of the precipitation.

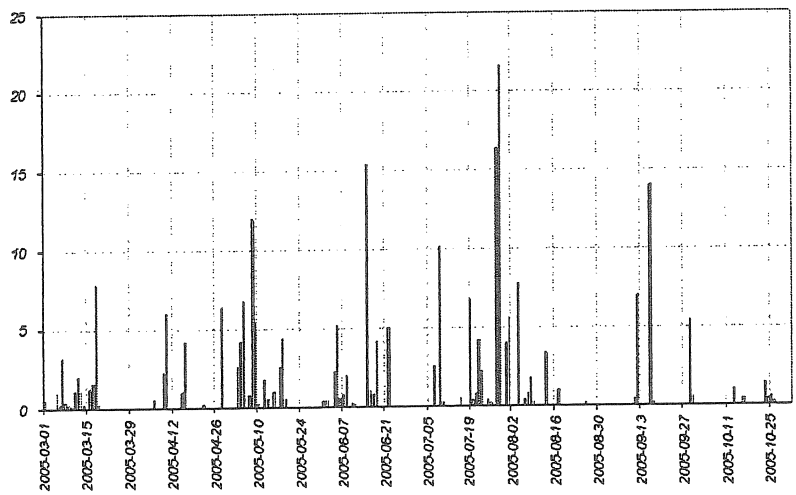

Fig. 15. Changes of precipitation in 2005 [mm].

5.5 Snow coverage observations

During winter measurements we have also monitored the height and density of the snow coverage. We considered that the slow drift of the gravity which can be clearly seen in fig. 6 can be explained by snow and ground water influence.

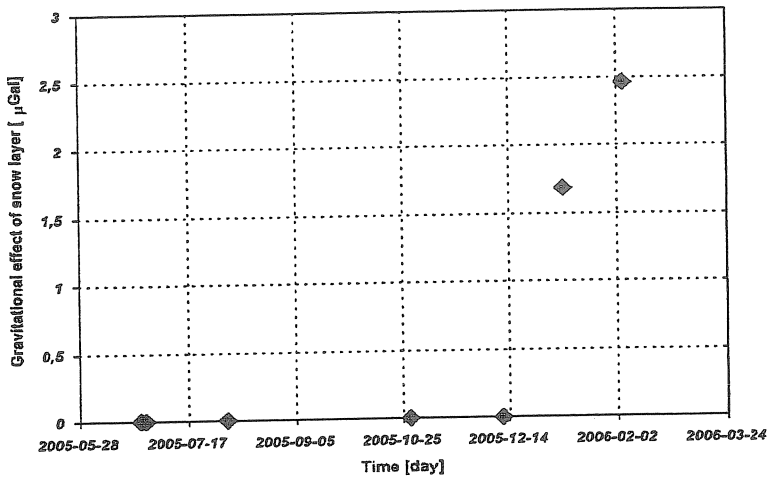

Fig. 16: Gravitational effect of a snow layer at Jozefoslaw.

6. SIMULTANOUS GRAVITY OBSERVATIONS

Before the ET breakdown we have made three simultaneous determinations of gravity using also FG5. Fig. 17 shows that the ET is quite well calibrated but the work on calibration will be done in the near future.

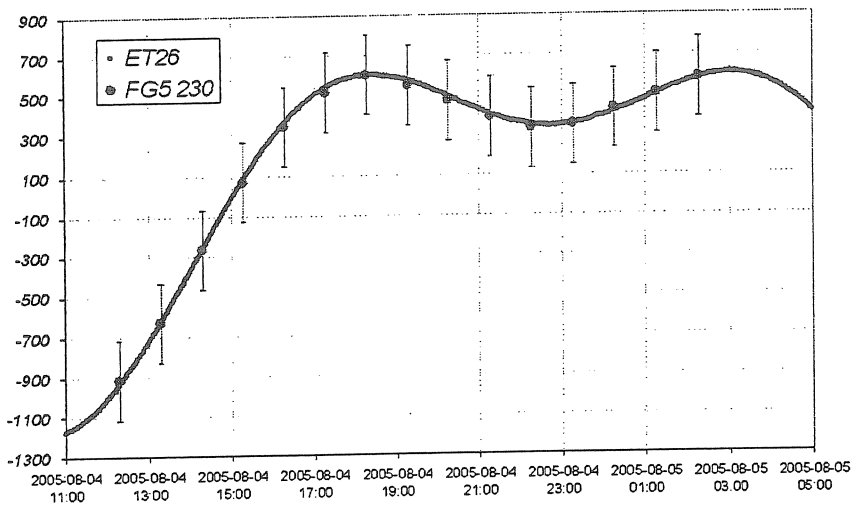

Fig. 17. Simultaneous gravity observations.

9. CONCLUSIONS AND PLANS FOR FUTURE

The paper presents a situation conditions in the Astro-Geodetic Observatory at Jozefoslaw and possibilities in the field of gravity changes monitoring there using the absolute gravimeter as well as gravimetric tide registration. Authors presume that our gravimetrical laboratory supplies good conditions for localisation there the comparison centre for absolute gravimeters in the region of Central and Eastern Europe. The monitoring of gravitational effects of geophysical phenomena gives possibility to improve gravimetric determinations and to compare them from epoch to epoch as well.

BIBLIOGRAPHY

1. Barlik M., Rogowski J. B. (1989): „Variation of the Plumb line Direction Obtained from Astronomical and Gravimetric Observations". Prace Naukowe PW. Geodezja z. 33, 1989.
2. Bogusz J. (2000) – "Investigation of Atmospheric Influence to the Gravimetric Tidal Observations". Ph. D. Thesis.
3. Wenzel H.-G. (1996): „ETERNA 3.30. Earth Tide Data Processing Package". Operation Manual.

News from the Geodynamic Observatory Moxa: the 4-component borehole strainmeter

G. Jentzsch[1*], T. Jahr[1], and H. Ishii[2]
1: Department of Applied Geophysics, Institute of Geosciences, University of Jena, Burgweg 11, D-07749 Jena, Germany
2: Tono Research Institute for Earthquake Science (TRIES), 1-63 Yamanouchi Akeyo-cho Mizunami City, GIFU Pref., 509-6132, Japan

Abstract

In September 2005 a 4-component borehole strainmeter was installed in a borehole inside the gallery of the Geodynamic Observatory Moxa, south of Jena, Germany. There, two quartz-tube strainmeters are recording along the two perpendicular axis of the gallery, as well as a laser-strainmeter connecting the end points of the quartz tubes. The borehole strainmeter comprises four strain gauges: three in the horizontal plane and one gauge for the vertical component. A fifth channel provides the temperature.

The strain sensor consists of a small magnetometer, the linear potentiometer FS-3791 invented by MACOME Corporation, Japan. The resolution of the strain sensors over the diameter of the sonde of 104 mm allows the detection of the tides as well as seismic signals with a high dynamic range. 1 μm corresponds to about 400 mV equivalent to 10^4 nstrain. Thus, the output signal of 1 mV equals 2.5 nm (~ 25 nstrain). The analog data is filtered and sampled every 10 seconds. The signal magnitude is in the order of some millivolts. Therefore the data is amplified by a factor of about 10, and the offset can be corrected before digitization. The first results presented here are promising.

Keywords:, borehole strain measurements, geodynamics, Geodynamic Observatory Moxa

1 Introduction

Continuous multi-component monitoring of crustal activities is the special field of co-author Hiroshi Ishii: He built several borehole devices comprising sensors for the monitoring of tilt, strain changes, seismic waves, magnetic field and temperature. Such instruments are installed in boreholes, the deepest drilled up to now being 1200 m (Ishii et al., 2003; Okubo et al., 2004; Asai et al., 2005). Thus, the design of the borehole sensor is adaptable to different tasks. The sonde provided for the Geodynamic Observatory Moxa consists of four strain sensors (three in the horizontal plain, one in the vertical), and a temperature sensor is suitable to monitor the conditions of the location (at the beginning especially the progress of hardening of the concrete to couple the sonde to the surrounding rock).

Besides other geophysical instruments, in the Geodynamic Observatory Moxa also three strainmeters are operating: These are two quartz-tube strainmeters (each 26 m long), oriented North-South and East-West, and one laser-strainmeter in a horizontal borehole (38 m) which connects the end points of both quartz-tubes to form a right angled triangle (Jahr et al., 2001; 2006). In the junction of the two galleries containing the quartz-tubes we drilled a 10 m deep borehole for the installation of the borehole strainmeter. To fix the strainmeter in the borehole an expanding cement is used. For Moxa observatory the provided borehole sensor comprises 3 horizontal strain sensors at different orientations (0°, 120°, 240°), a vertical sensor and a temperature sensor.

2 The borehole strainmeter: Sensor and calibration

The sensor consists of a mechanical sensor operating like a miniature fluxgate magnetometer. Fig. 1 shows a sketch of this device. It consists of a pair of magnets whose

* Corresponding author: gerhard.jentzsch@uni-jena.de

north and south poles are aligned opposite, such that a strong magnetic field gradient emerges (top left). The miniature sensor is given in the center and its orientation on the right. The travelling direction is up and down in parallel to the paper surface. The sketch below shows the perpendicular direction to demonstrate the importance of the alignment along the center, and the air-gap, crucial for the sensitivity and the resolution of the signal. The displacement is monitored by the relative movement between these magnets and a very small fluxgate magnetometer (Linear potentiometer FS-3791, MACOME Corporation, Japan).

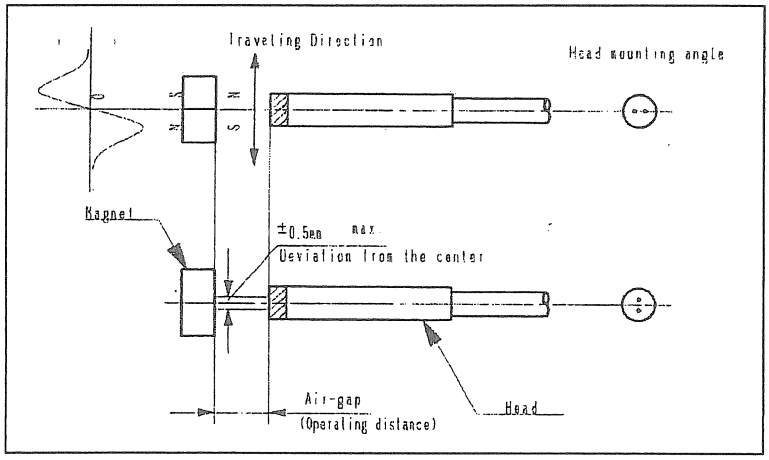

Fig.1. Sketch of the magnetic displacement read-out system (Linear potentiometer FS-3791 by MACOME Corporation, Japan; from the manual, courtesy by MACOME).

In order to increase the resolution a mechanical unit is used to amplify the deformation signal by a factor of about 40. Fig. 2 shows the mechanical amplifier. The displacement signal is fed into this plate and amplified in three stages due to the lay-out of the hinges.

The calibration function is determined in the laboratory. Fig. 3 shows one example.

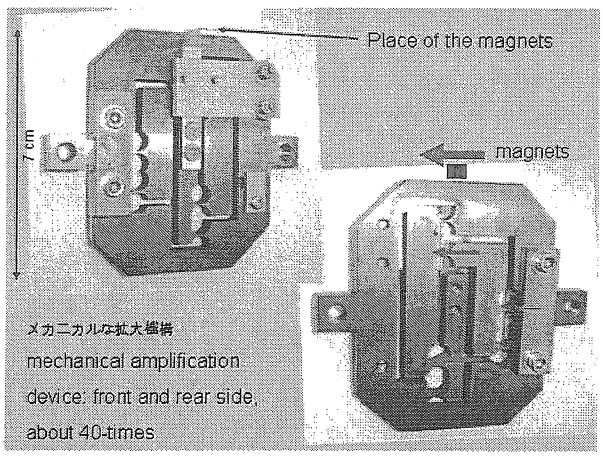

Fig. 2. Mechanical amplification device: Note the hinges which take care that the input deformation is amplified in several stages. Finally, the deformation is read out by the magnetic sensor.

Since the diameter of the borehole instrument is only 0.104 meter, the resolution of the magnetometers have to be very high. Fig. 4 shows a section of the calibration function of the sensor HS-3. The other three sensors have similar relations, but different offsets. The linear factor is the amplification factor which has to be multiplied with the amplification applied in the second step. The factor here is 370.7428 mV/μm, with a very small error of < 0.5 %. According to the calibration table of sensor HS-1 we have the relations:

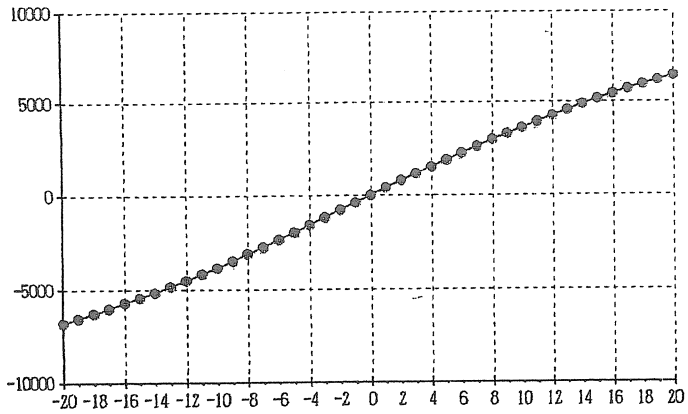

Fig. 3. Calibration function of one of the sensors (millivolts / vertical axis versus displacement / horizontal axis); note linearity around zero (from the manual, courtesy by MACOME).

1 μm ≡	370.7428 mV	corresponding to	0.96 * 10^4	nstrain
1 mV ≡	2.70 nm	corresponding to	27.0	nstrain

Since the strain changes to be observed are in the order of magnitude of about 50 nstrain it is clear that the calibration factor is not critical. But, before amplifying the signal for digitisation we have to determine its level and note the factor. If there is no strong drift over several micrometers (which is normally not to be expected) this factor can be used throughout.

In order to digitise the data we first apply analog filtering (anti-aliasing) with a cut-off of about 20 mHz. In this step we have the opportunity to compensate the offset, if necessary, and the signal is then amplified by a factor of about 10 (HS-1: 9.93; HS-2: 9.66; HS-3: 10.00; VS-1: 10.04). Then, we sample the data every 10 seconds using a HP34470A (Agilent, resolution 24 bit), multiplexing all four channels and the temperature channel. In addition we also record one of the strain outputs directly for comparison.

The whole sonde has a length of 1.22 meters. It comprises of four sections: At the bottom is a weight to reduce buoyancy, two sections contain the horizontal and the vertical strain sensors, respectively, and one section on the top contains the electronics and the temperature sensor. The borehole has a diameter of 150 mm, and a depth of 10 m. Actually, the borehole was drilled more than two meters deeper, but an inclining fault was detected, and, thus, it was decided to fill it with concrete up to the installation depth of 10 m. The installation was carried out such that a rod was fixed to the top with a mark indicating the orientation. Later, the borehole was filled with an expanding cement mixed according to a special recipe. The strainmeter was pressed into the fluid cement, and the orientation was kept by turning the rod accordingly. Finally, it was oriented such that channel HS-1 points towards east.

Although the cement was filled up to the top of the borehole, its volume was reduced during the drying out time. Now, we have about 2 meters between the top of the cement and the gallery floor which can be used to calibrate the strainmeter by taking out and/or filling in water.

2 Data and first results

It took about four weeks for the cement to dry out, which was monitored by the temperature and the strain changes. Fig. 5 gives the data for the first period, September 12 until

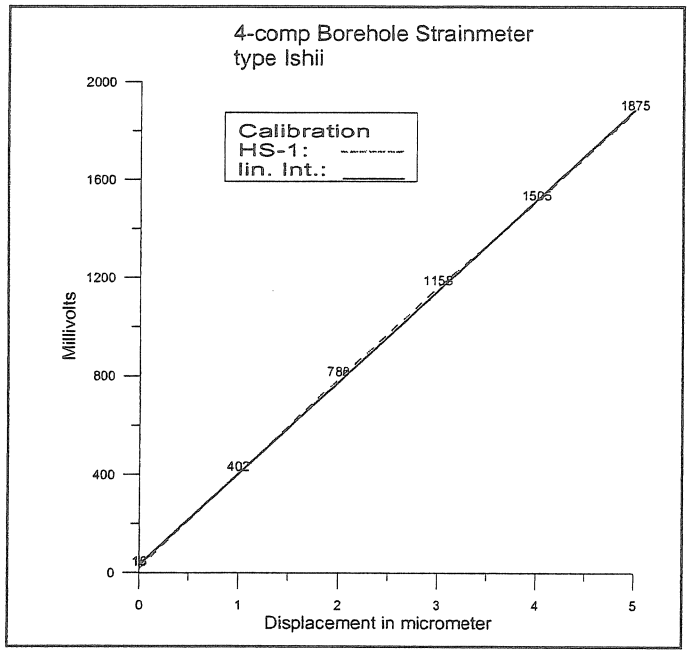

Fig. 4. Calibration function of horizontal sensor HS-1: This function is determined in the laboratory. The deviation to linearity is very small, and the factor is determined by linear interpolation. The numbers at the curve denote the voltage outputs obtained at the displacements in steps of one micrometer.

Formatted: Font: (Default) Arial, 11 pt, English (U.K.)

November 4, 2005. During this period we recorded with a reduced resolution of 10 percent to avoid the data going off scale. Thus, the amplitude scales (on the left) have to be multiplied by a factor of 10. The scale on the right denotes the temperature in degree devided by 10: The temperature of the rock is about 7.5° Celsius. The reasons for the two small steps are unknown.

Fig. 6 shows a section of the data of channel 2 (SH-2) pointing 210°, November 24 until December 10, 2005. The output in volts has to be converted to nanostrain using the calibration provided in the manual. The tides are clearly visible, as could be expected. The recording unit used now amplifies the signal by a factor of about 10.

3 Discussion

The borehole strainmeter runs in parallel with the above mentioned quartz-tude strainmeters and the laser strainmeter. Therefore, it is most interesting to compare the observed borehole strain with these long-based instruments. As a first example of this comparison we show a spectrum of both East-West components (Fig. 7). For this comparison we used a section of 33 days, filtered the data to hourly samples and computed the spectra. The time interval is February 5 – March 9, 2006. Both spectra are calibrated and the amplitudes can be compared directly. As can be seen, the noise levels are about the same, especially in the long-period part, but the tidal amplitudes are a little different.

Since the calibration is still preliminary and has to be verified, it is obvious that the diurnal tidal amplitudes are of the same order of magnitude and fit quite well. In contrary, the semi-diurnal amplitudes are quite different. Since the East-West strain is very sensitive against changes in orientation we assume that the azimuth determined by adjusting the rod fixed to the strainmeter may not be as accurate as intended. We will check the orientation by comparison of tidal analyses with the theory and with the other three strain components.

Table 1 contains the comparison of the first tidal analyses of both record sections. The results for the individual tidal constituents confirm the findings from the spectra. The obtained noise levels as well as the standard deviation are of the same order of magnitude.

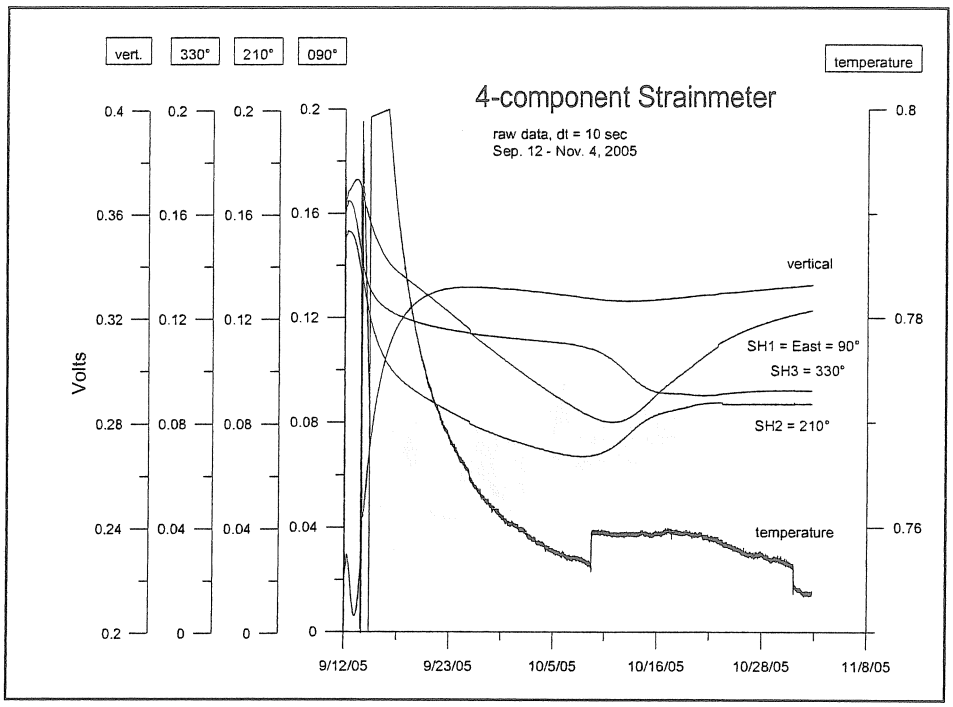

Fig. 5. Data for the first period, September 12 until November 4, 2005, recorded with a reduced resolution; note the running-in period. The temperature scale must be multiplied by 10 to give degrees Celsius.

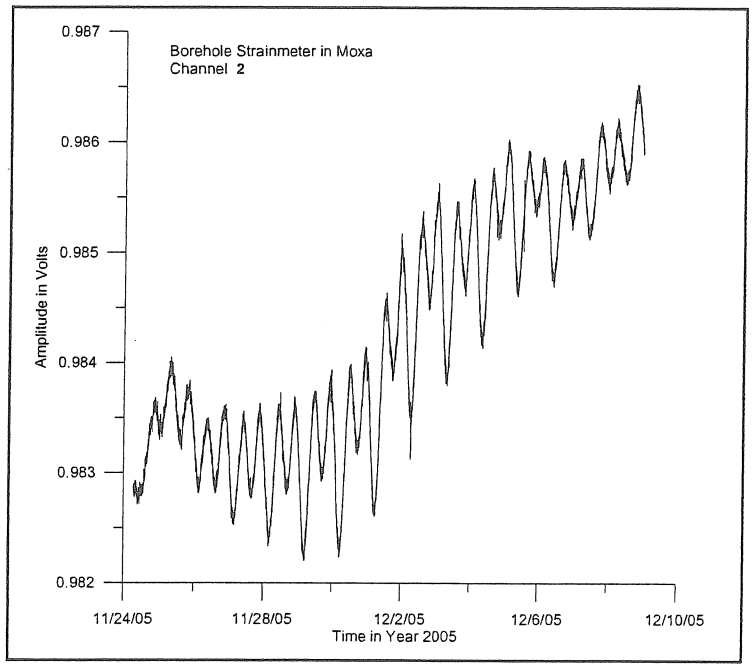

Fig. 6. Data of channel 2 pointing about 210° (South-West to North- East); the period is November 24 until December 9, 2005, now recorded with full resolution.

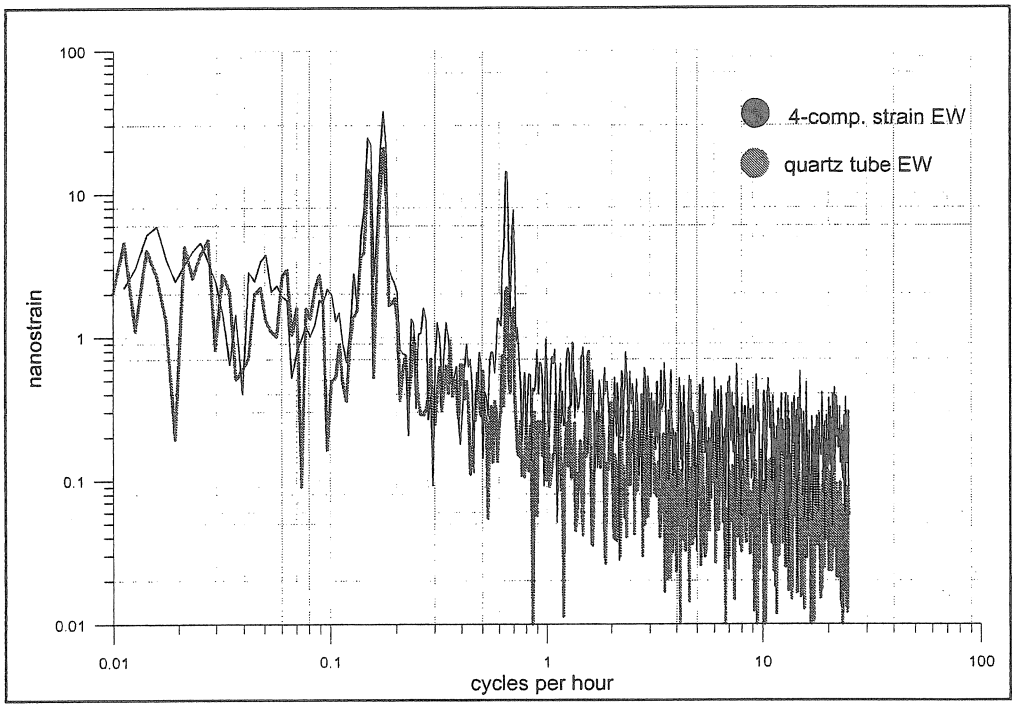

Fig. 7. Spectra of the strainmeters in direction EW: SH-1 and quartz-tube, hourly values, 33 days: Feb. 5 – March 9, 2006; note the good correlation in the low-frequency part (see text).

Acknowledgments

At first we have to thank the company MACOME, especially the president Shigejiro Shimizu and Masao Iikubo, the sales manager. Hideo Sugaya constructed the sonde. They helped to successfully install the sonde in the observatory Moxa. The key to this success was the contribution of the two technicians of the observatory, Wernfrid Kühnel and Matthias Meininger, who took care for all boundary conditions needed for the installation.

References

Asai, Y., M. Okubo, H. Ishii, T. Yamauchi, Y. Kitigawa, and N. Koizumi, 2005. Co-seismic strain-steps associated with the 2004 off the Kii peninsula earthquakes – observed with Ishii-type borehole strainmeters and quartz-tube extensometers. Earth Planets Space, 57, 303 – 308.

Ishii, H., T. Yamauchi, Y. Asai, M. Okubo, S. Matsumoto, and H. Aoki, 2003. Continuous multi-component monitoring of crustal activities by a newly developed instrument installed in a 1200 m deep borehole – The deepest multiple observation in the world consisting of stress, strain, tilt, seismic waves, geomagnetism, temperature. Paper presented at the XXII General Assembly of IUGG, Sapporo, Japan.

Jahr, T., G. Jentzsch, and C. Kroner, 2001. The Geodynamic observatory Moxa / Germany: Instrumentation and purposes. Proc. 14th International Symposium on Earth Tides, Special Issue of the Journal of the Geodetic Soc. of Japan, 47/1, 34 – 39.

Jahr, T., C. Kroner, and A. Lippmann, 2006. Strainmeters at Moxa Observatory, Germany. In: Jentzsch, G. (Ed.) Earth Tides and Geodynamics: Probing the Earth at Sub-Seismic Frequencies, J. of Geodynamics, Vol. 41, 1-3, 205 – 212.

Okubo, M., Y. Asai, H. Aoki, and H. Ishii, 2004. The seismological and geodetical roles of strain seismogram suggested from the 2004 off the Kii peninsula earthquake. Earth Planets Space, 57, 303 – 308.

Wenzel, H.-G., 1996: The Nanogal Software: Earth Tide Data processing Package ETERNA 3.30., Bull. d'Inf. Marées Terrestres 124, 9425-9439.

Table 1. Comparison of computed tidal parameters for the East-West components of the borehole strainmeter and the quartz-tube strainmeter; note differences in the amplitudes of the semi-diurnal constituents (period: 68 days, January 1 until March 9, 2006). The analyses were carried out using the program ETERNA 3.3 (Wenzel, 1996).

Borehole strainmeter, component SH-1 (East-West)

Estimation of noise by FOURIER-spectrum of residuals

0.1 cpd band	99.9990	nstr	1.0 cpd band	0.1292	nstr
2.0 cpd band	0.0777	nstr	3.0 cpd band	0.0701	nstr
4.0 cpd band	0.0533	nstr	white noise	0.0768	nstr

adjusted tidal parameters :

	ampl. [nstr]	ampl.fac.	stdv.	ph. lead [deg]	stdv. [deg]
Q1	0.7935	0.60310	0.03786	10.0495	3.5969
O1	4.3631	0.63493	0.00843	6.6419	0.7603
M1	0.5025	0.93031	0.07620	17.9806	4.6931
K1	5.9721	0.61820	0.00596	5.5735	0.5526
J1	0.3829	0.70855	0.09666	-34.7265	7.8164
OO1	0.2196	0.74317	0.11900	-11.8649	9.1745
2N2	0.1496	7.37131	1.45881	179.6032	11.3390
N2	0.6748	5.31177	0.33323	-156.1341	3.5944
M2	3.2057	4.83151	0.06347	-158.0459	0.7527
L2	0.0896	2.84154	0.74624	151.3012	15.0468
S2	1.2938	4.19151	0.11877	-160.1042	1.6236

Degree of freedom:	1493	
Standard deviation:	1.098	nstr

Quartz-tube strainmeter (East-West)

Estimation of noise by FOURIER-spectrum of residuals

0.1 cpd band	99.9990	nstr	1.0 cpd band	0.1370	nstr
2.0 cpd band	0.0410	nstr	3.0 cpd band	0.0676	nstr
4.0 cpd band	0.0553	nstr	white noise	0.0721	nstr

adjusted tidal parameters :

	ampl. [nstr]	ampl.fac.	stdv.	ph. lead [deg]	stdv. [deg]
Q1	0.8454	0.64253	0.04248	3.5051	3.7880
O1	4.5574	0.66321	0.00938	0.8582	0.8099
M1	0.4674	0.86525	0.08549	-17.3093	5.6611
K1	5.7250	0.59262	0.00654	-0.0039	0.6327
J1	0.4303	0.79627	0.10789	11.2228	7.7635
OO1	0.2555	0.86436	0.13454	5.6552	8.9180
2N2	0.0562	2.76907	0.82147	-88.6306	16.9974
N2	0.2348	1.84849	0.18576	126.7215	5.7578
M2	0.8525	1.28481	0.03518	-175.5750	1.5688
L2	0.0579	1.83529	0.41173	160.1035	12.8538
S2	0.4860	1.57465	0.06670	-106.1775	2.4270

Degree of freedom:	1555	
Standard deviation:	1.108	nstr

Stability investigation of the new three-dimensional extensometric observatory in Bakonya, Hungary

Gyula Mentes[1], Zsolt Berta[2], Ildikó Eper-Pápai[1]

[1]Geodetic and Geophysical Research Institute of the Hungarian Academy of Sciences,
[2]Mecsekérc Environmental Protection Public Limited Company

Abstract

In year 2000 a new three-dimensional extensometric station was established in the western area of Mecsek Mts. in Hungary. The paper describes the new observatory and the instruments. Registered data and results from data analysis are given. The influence of the temperature and air pressure variations on the extensometric measurements were investigated and compared with those obtained in the case of the closed deep station in an abandoned uranium mine not far from the new 3D surface station. The results show that the new surface station is more sensitive to the temperature, air pressure variations and to the moisture variations of the soil above the station than the deep station in the mine. The measured large displacements are probably due to the cavity and local disturbing effects as a consequence of the geometry of the surface station.

1. Introduction

In May 1992 a deep extensometric station was established for local geodynamical observations in a uranium mine near Pécs. This station was closed in 1999 because the mining activity was given up and the mine was closed. In 2000 a new three dimensional (3D) extensometric station was established for the investigation of tectonic movements on a possible area to dispose high level radioactive wastes in the Western Mecsek Mts. in Hungary. Both observatories were built by the Mecsekérc Environmental Protection Public Limited Company in the frame of a scientific cooperation with the Geodetic and Geophysical Research Institute of the Hungarian Academy of Sciences (GGRI).

The paper presents the recorded data, investigates the influence of the environmental parameters. Since the geologic circumstances of the new 3D and the closed deep observatories are similar, they can be compared from the view-point of stability.

2. The 3D extensometric station in Bakonya

The 3D extensometric station was established near to the earlier deep station in the western part of the Mecsek Mts. as it is shown in Fig. 1. The coordinates of the observatory are: latitude 46.1145°N; longitude 18.1303°W. The new station was placed in an abandoned underground explosive repository of the uranium mine in Bakonya. It is a near surface observatory overlaid by the bedrock with a thickness of about 60 m. The ground-plan of the station is shown in Fig. 2. The extensometers are placed in the most inner gallery about 130 m from the entrance.

Figure 3 shows the extensometers in the gallery. The instruments are made of quartz tubes with a diameter of 45 mm, a wall thickness of 2 mm and have the same construction as the extensometer in the Sopron Observatory (Mentes, 1991). The three horizontal extensometers have a common pillar as one end of the instruments. In the longitudinal direction of the gallery there are two parallel extensometers a long (20 m) and a short (1.7 m) one.

Perpendicular to these extensometers there is a transversal short (1.7 m) instrument. At this end of the transversal extensometer the pillar for the displacement sensor is common with the one of the vertical extensometer, the other end of which is fastened to the top of the gallery. The length of the vertical extensometer is also 1.7 m.

All of the extensometers work with the capacitive sensor developed at the GGRI (Mentes, 1991). The sensor electronics were calibrated in the laboratory of the GGRI (Mentes, 1995). The short extensometers have no built-in calibration device, the long extensometer has a magnetostrictive calibration device developed at the GGRI. Beside the deformation data temperature, humidity and air pressure data are also recorded. The parameters of the extensometers are given in Table 1.

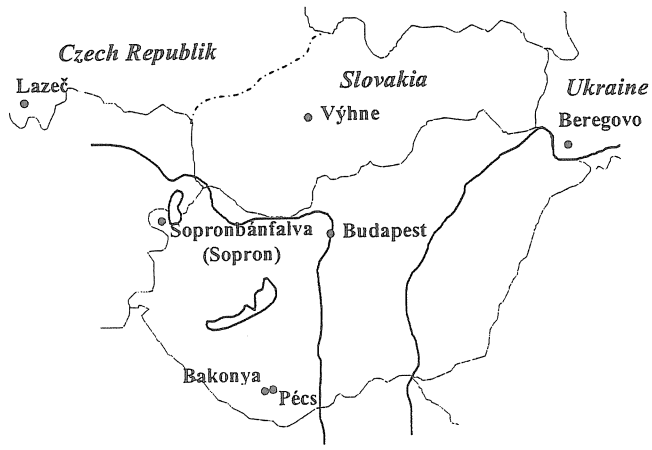

Fig. 1. Extensometric observatories in the Carpatho-Balkan Region

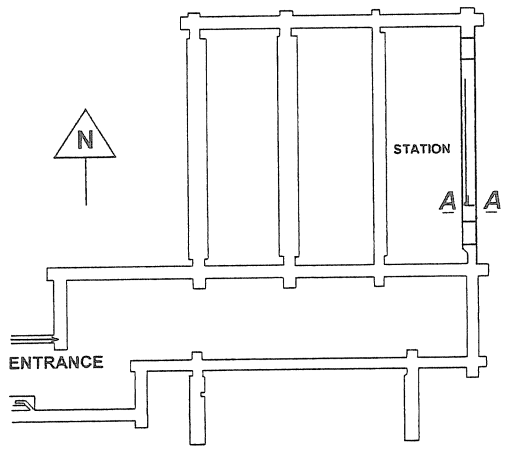

Fig. 2. The ground-plan of the 3D extensometric observatory

Table 1. Parameters of the extensometers

Extensometer	Length [m]	Direction	Scale factor [nm/mV]
Ext.1 (E1)	20	N-S	1,491
Ext.2 (E2)	1.7	N-S	1,385
Ext.3 (E3)	1.7	E-W	1,539
Ext.4 (E4)	1.7	Vertical	1,347

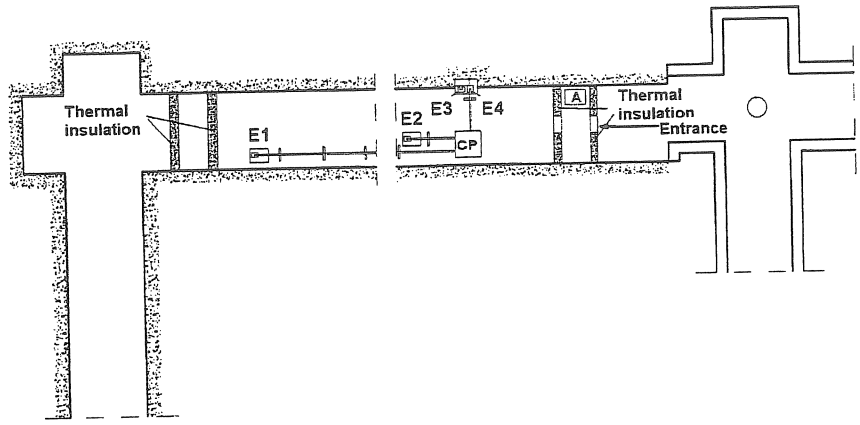

Fig. 3. Lay-out of the extensometers in the station

3. Results of data analysis

In spite of the fact that the station was established in 2000 due to some technical problems we have continuous data series only since the beginning of 2003. In this year the recorded displacements were very high and the signals went out from the measuring range very often. The situation was the same in year 2005, so the data series obtained in 2004 were chosen for the stability investigations of the observatory. In Fig. 4 the raw data measured in 2004 are given. Figure 4 shows clearly that after the first quarter of the year something happened and the measured displacements in all components became much higher than previously. The step corrected extensometric data are given in Fig. 5. The curves obtained from the parallel instruments Ext.1 and Ext.2 exhibit very similar characteristic, but their relative strain rates are different i.e. the ratio of the lengths of instruments differs from the ratio of the measured displacements. The absolute displacement measured by extensometer Ext.1 is about 75000 nm and the one obtained by Ext.2 is about 22500 nm. The difference is probably caused by the inhomogeneity of the rock. Displacements measured by the transversal (Ext.3) and the vertical (Ext.4) extensometers are much more disturbed than those measured by the longitudinal instruments. The reason is probably the fact that the gallery of the instruments is strongly deformed by the water content of the soil above the station. There are four galleries not far from each other (Fig. 2), therefore the transversal and vertical deformations of the observatory are much higher than the longitudinal one (cavity effect). Unfortunately, the precipitation was not measured during the investigated period, so it was not possible to investigate its influence on the registration.

To retrieve the tidal waves from the data a polynomial of 9th order was fitted to the raw data and this polynomial was subtracted from the original series to obtain short periodic variations. These residual data were Fourier-transformed to get the amplitude spectrum. Figure 6 shows the amplitude spectra of the data series. All the spectra show clearly the main diurnal and semidiurnal tidal waves except the vertical extensometer (Ext.4). One of the short horizontal extensometers (Ext.2) does not produce clearly emerging tidal lines in the diurnal band, these peaks are hidden by the spectral noise, while the other short extensometer (in the transversal direction) gives the proper spectral peaks in both tidal bands. Nevertheless at S_2 frequency the amplitude ratios calculated in the case of the parallel short and long extensometers are approximately the same as the ratio of their lengths.

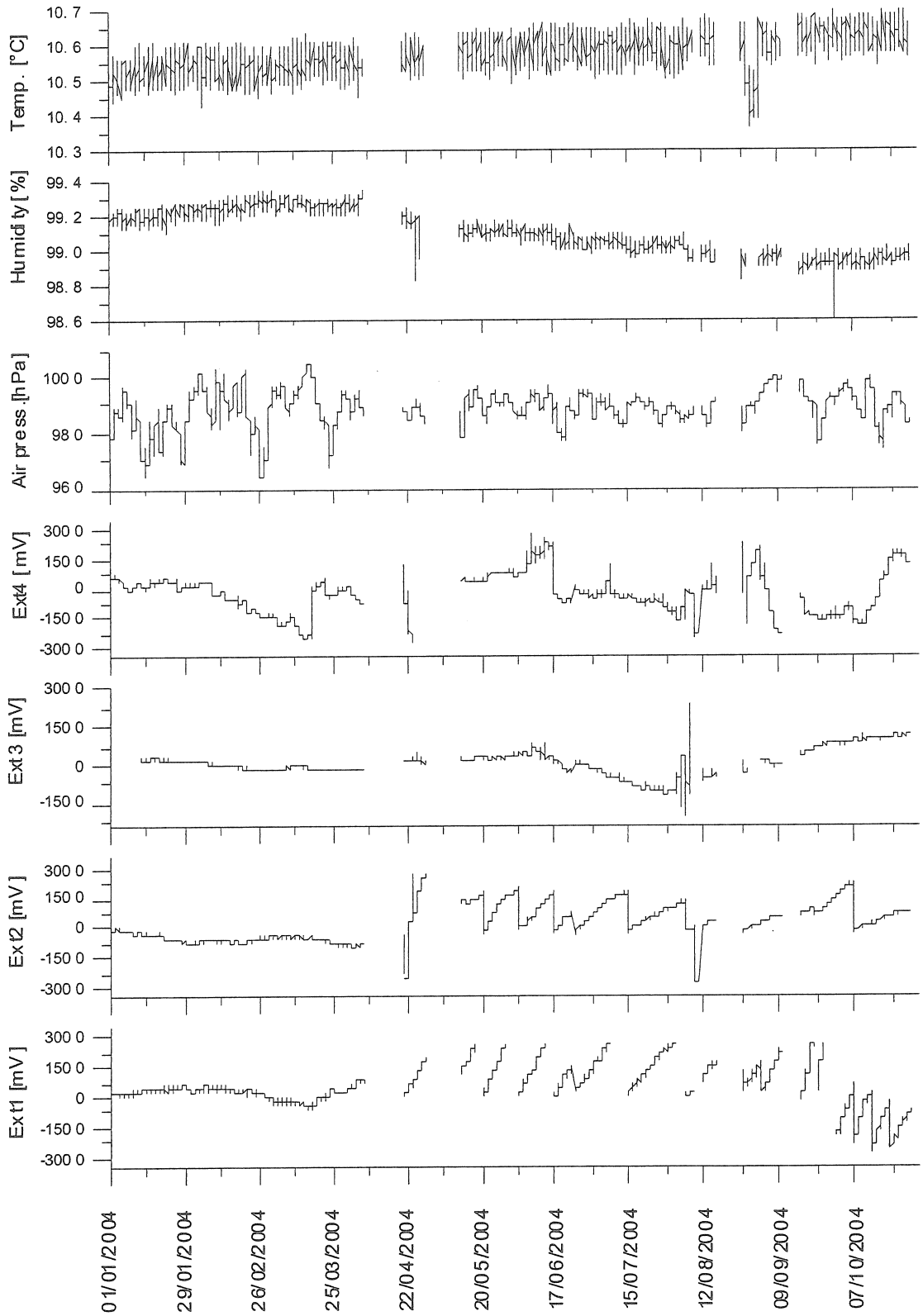

Fig. 4. Raw data measured at the Bakonya station in 2004

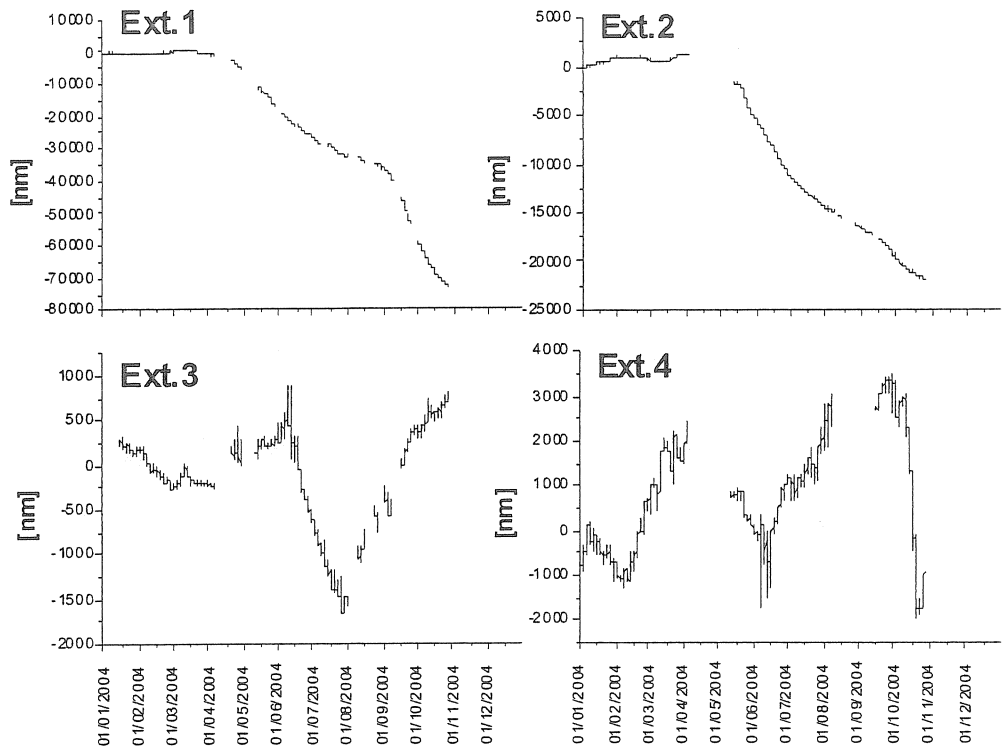

Fig. 5. The displacements recorded by extensometers at the Bakonya station in 2004

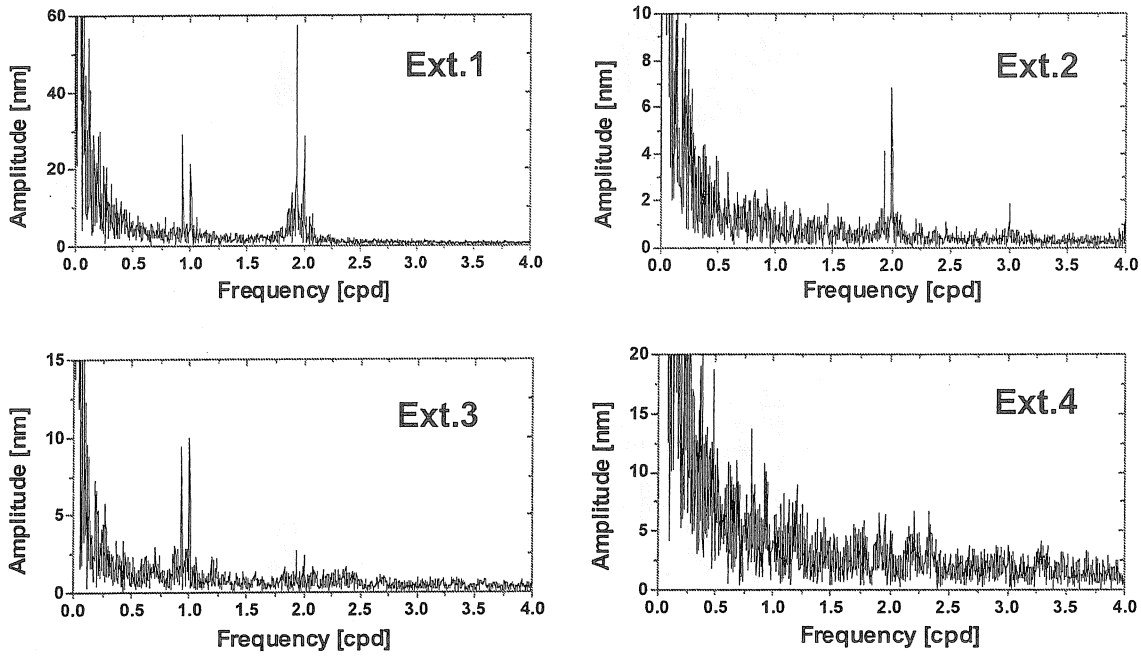

Fig. 6. Amplitude spectra of the extensometric data

Tidal parameters were calculated by means of the Earth tide data processing program ETERNA 3.30. (Wenzel, 1996). In the case of the vertical extensometer the tidal parameters could not be determined because of the strongly disturbed signal. The obtained tidal amplitudes measured by the horizontal extensometers are compared with the theoretical values in Fig. 7.

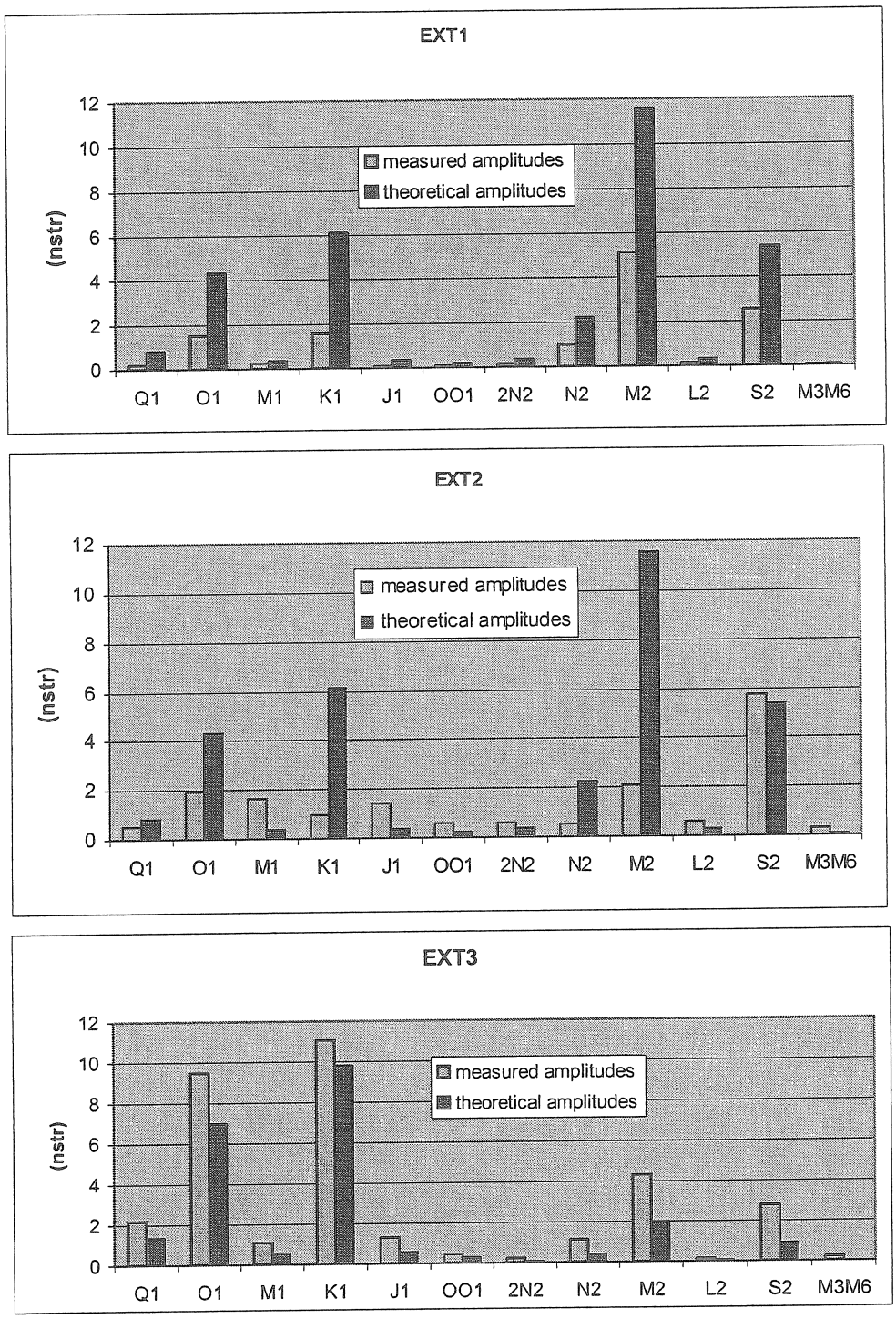

Fig. 7. The tidal amplitudes measured by the horizontal extensometers and the calculated theoretical amplitudes

In Figure 7 we can see that the measured amplitudes are smaller in the case of the longitudinal extensometers than the theoretical amplitudes. At the transversal extensometer (Ext.3) it is inverse, the amplitude factors are higher than 1.0. Although different characteristics of the tidal responses in the case of the perpendicular extensometers can be observed, this discrepancy presumably may be attributed to the same factors (local geological inhomogeneities, geometry, surface topography) which develop their effects differently into the perpendicular directions.

4. Comparison of the stability of the deep and the surface station

The deep extensometric station was established in the uranium mine in 1040 m depth. A detailed description of the station is given by Mentes and Berta (1997). The raw data recorded in the period between 1993 and 1999 is shown in Fig. 8. The calculated tidal parameters are given in Table II. For the sake of a numerical comparison the amplitudes and phase lags of the tidal waves obtained by the long extensometer (Ext.1) in Bakonya are given in Table III.

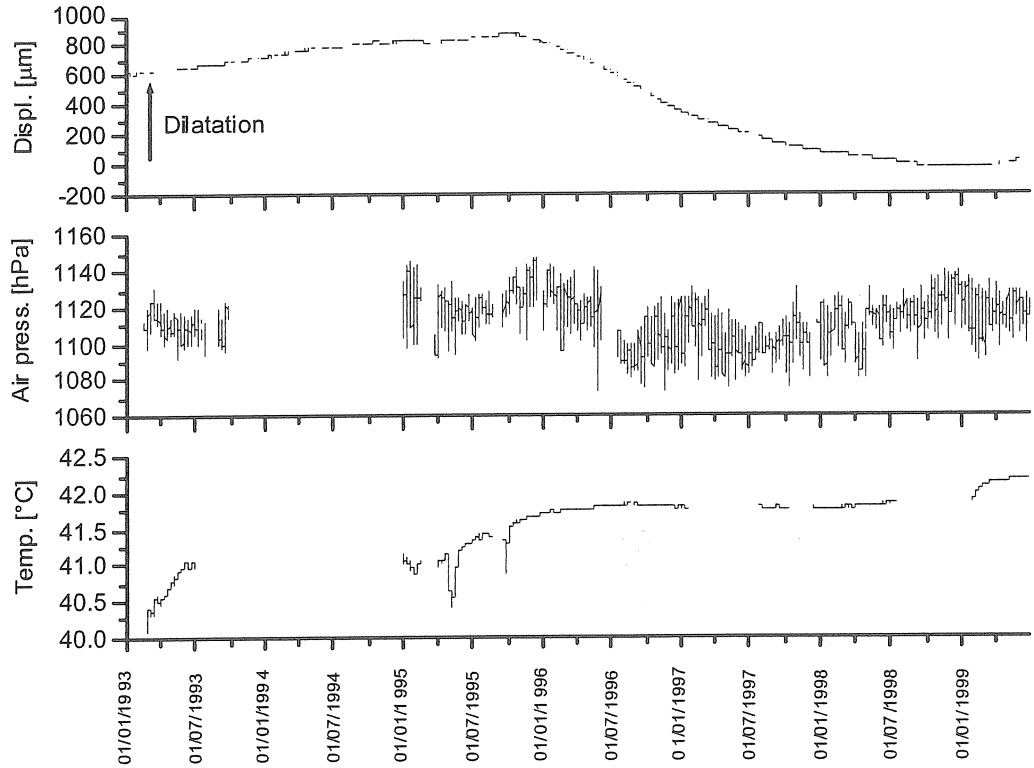

Fig. 8. Raw data recorded at the deep station in the uranium mine

The consistent tidal amplitude factors prove that stable deformation measurement conditions were provided in the deep observatory. In the case of the new 3D station we also get similar, almost uniform amplitude factors (in the range of 0.3-0.4). There is a difference in the tidal responses of the two measurement systems, namely from the surface station the amplitude factors have not exactly the same magnitude in the tidal frequency bands (in the diurnal band they are about 20 % lower). In case of the gravitational tide the solar effect is about the half of the lunar effect in contrast with the barometric waves, which are mainly guided by daily thermal variations (Chapman and Lindzen, 1970). The microbarograph

measurements carried out by Mentes (2004) prove also that the S_2 solar semidiurnal wave is dominant in the atmospheric tide. The amplitude spectrum of the air pressure variations recorded at the 3D surface station shows clearly this fact (Fig. 9). The semidiurnal air pressure variations seem to induce higher strain loading in the surface station than in the deep observatory, so the atmospheric tidal loading is supposed to be responsible for the smaller diurnal tidal factors in the surface station. It means that the surface station should be more sensitive to air pressure variations than the deep observatory.

Table II. Tidal parameters obtained in the uranium mine in Pécs

Wave group	Theoretical amplitude [nstr]	Calculated amplitude [nstr]	Phase lead [degree]
Q1	0.909	0.232±0.165	-41.754±37.092
O1	4.749	2.235±0.036	-21.029±4.331
M1	0.373	0.059±0.344	-108.542±123.984
P1	2.209	1.077±0.065	-41.343±7.6573
K1	6.676	2.662±0.024	-19.322±3.485
J1	0.373	0.410±0.428	-10.949±22.330
OO1	0.204	0.204±0.998	-37.368±54.235
2N2	0.333	0.181±0.237	-54.951±25.128
N2	2.087	1.024±0.052	-39.696±6.021
M2	10.902	5.041±0.010	-46.265±1.271
L2	0.308	0.296±0.405	-74.083±24.168
S2	5.072	2.382±0.022	-45.408±2.734
K2	1.378	0.711±0.106	-48.696±11.810

Table III. Tidal parameters obtained by the long extensometer (Ext.1) in Bakonya

Wave group	Theoretical amplitude [nstr]	Measured amplitude [nstr]	Phase lead [deg]
Q1	0.830	0.218±0.136	-41.605±22.624
O1	4.335	1.518±0.024	-33.102±2.961
M1	0.341	0.274±0.426	-26.080±22.823
K1	6.094	1.572±0.019	-42.264±0.210
J1	0.341	0.071±0.370	-48.278±75.712
OO1	0.187	0.071±0.404	-27.432±45.628
2N2	0.354	0.163±0.118	0.625±10.775
N2	2.214	0.989±0.017	-6.629±1.581
M2	11.563	5.109±0.003	-10.681±0.260
L2	0.327	0.133±0.079	-10.585±7.955
S2	5.379	2.558±0.005	-16.797±0.437

On the basis of investigations for meteorological effects (Mentes and Eper-Pápai, 2006), the data of the deep extensometer have rather small pressure induced noise in the tidal frequency bands. According to data analysis of the 3D station, clear correlation exists between the atmospheric pressure and deformation data (in the long-term scale) which is more

expressed than in the case of the 1 km deep station. It should be also noted that the yearly long-term strain rates from the deep extensometric and the new reliable Ext.1 data are in good agreement. The results of investigation of the barometric effect by regression analysis are summarized in Table IV.

The rates of the displacements measured by deep and surface instruments are given in Table V. The magnitudes of the extensions are the same from the deep and the Ext.1. extensometers. It is realistic since the two stations are not far from each other and the main tectonic structure should be the same at both stations. The deformation rate measured by Ext.2 is much higher than it should be on the basis of the length-ratio of the parallel instruments. The reason of the difference is unknown, probably it is in connection with the local rock inhomogeneities as it was mentioned above. The rates measured by the transversal and the vertical extensometers do not seem to be reliable as the measurements are highly disturbed.

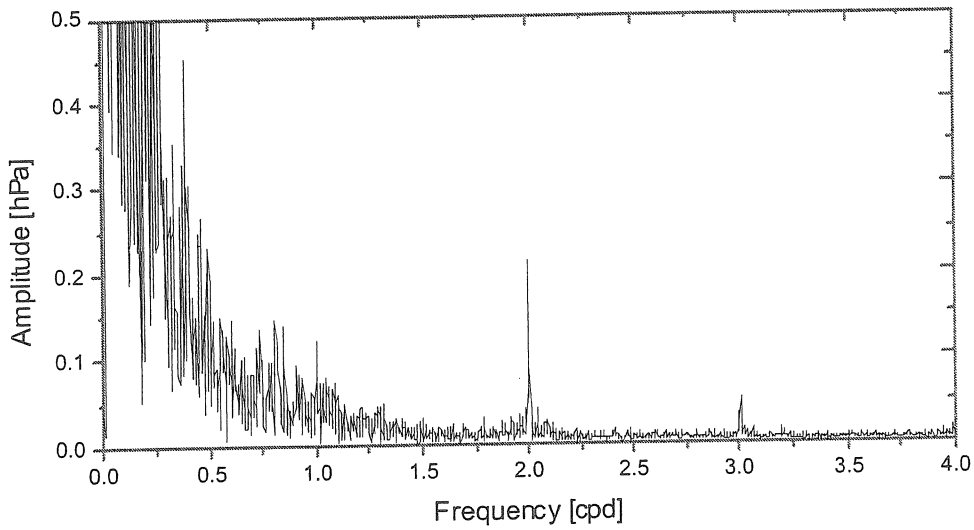

Fig. 9. Amplitude spectrum of the air pressure data recorded at the 3D surface station

Table IV. Comparision of the air pressure effect

Air pressure effect	Deep station	3D surface station
Short-term	0.3 nm/hPa	16 nm/hPa
Long-term	6.6 nm/hPa	124 nm/hPa

Table V. Comparison of the rates of the measured extensions

Extensometer	Rate of extension [μm/year]	Direction of the displacement
Deep extensometer	-85	contraction
Ext.1	-84	contraction
Ext.2	-32	contraction
Ext.3	-0.064	not reliable!
Ext.4	+2.5	not reliable!

Conclusions

Both the results of the tidal analysis and the investigations of the meteorological effects show unambiguously that the surface station is much more sensitive to the air pressure variations than the deep observatory. The pressure induced deformations are clearly superposed on the deformation signal of the instrument. From the analysis it seems that in the tidal frequency bands there is also pressure induced noise due to atmospheric tide, and this effect is of higher extent than in the deep station.

The displacement curves measured by the longitudinal extensometers in the 3D surface station are very similar but have difference in the magnitude, the reason of which can be the different local geological inhomogeneities between the ends of the instruments.

The vertical extensometer (Ext.4) does not provide useable data and the measured displacements of the transversal instrument (Ext.3) are very high. The construction of the station (cavity effect) is responsible for the disturbed data measured by the transversal extensometer which should be placed in the middle line of a long gallery. Probably the variations of the soil moisture above the station cause the high vertical deformations and presumably they are responsible for the high transversal displacements also. It could be proved by recording the precipitation and the ground water level above the station.

We can now state that the station is not suitable for recording reliable deformation measurements in the transversal and vertical directions because of the high disturbances caused by local and meteorological effects.

Acknowledgements

This research was supported by the Hungarian National Scientific Research Fund (OTKA) in the frame of the research project T046264.

References

Chapman S, Lindzen R S 1970: Atmospheric tides. D. Reidel Publishing Co.

Mentes Gy 1991: Installation of a quartz tube extensometer at the Sopron Observatory. Marees Terrestres Bulletin d'Informations. Bruxelles, No. 110, pp. 7936-7939.

Mentes Gy 1995: High Precision Calibration of Quartz Tube Extensometers. Proceedings of the Twelfth International Symposium on Earth Tides (Ed. H. T. Hsu), Science Press, Beijing, New York, pp. 209-214.

Mentes Gy 2004: Atmospheric tide obtained by the microbarograph developed at the Geodetic and Geophysical Research Institute of the Hungarian Academy of Sciences. Acta Geod. Geoph. Hung., Vol. 39, No. 1, pp. 39-48.

Mentes Gy, Berta Zs 1997: First results of the extensometric measurements in South Hungary. Marees Terrestres Bulletin d' Informations. Bruxelles, No. 127, pp. 9744-9749.

Mentes Gy., I. Eper-Pápai I. 2006: Investigation of meteorological effects on strain measurements at two stations in Hungary. Journal of Geodynamics, Vol. 41, No. 1-3, pp. 259-267.

Wenzel H-G 1996: The nanogal software: Earth tide data processing package ETERNA 3.30. Marees Terrestres Bulletin d' Informations, No. 124, pp. 9425-9439.

New results of the extensometric measurements at Budapest observatory

Gyula Mentes[1], Ildikó Eper-Pápai[1], Márta Kis[2], Gábor Újvári[1]

[1]Geodetic and Geophysical Research Institute of the Hungarian Academy of Sciences,
[2]Eötvös Loránd Geophysical Institute of Hungary

Abstract

First in Hungary two extensometers were installed by the Eötvös Loránd Geophysical Institute between 1980 and 1990. Both instruments had been working till 1996. After a recording break of about 7 years the instruments were renewed in 2004 and the extensometers have been recording continuously since that year. In this paper the first data series are analysed. On the basis of the new data series the influence of environmental parameters is also investigated and the possible conclusions in connection with the stability of the observatory are drawn.

1. Introduction

The first extensometer in Hungary was installed by the Eötvös Loránd Geophysical Institute (ELGI) in Budapest in the frame of a scientific co-operation with the Geophysical Institute in Moscow (Latinina et al., 1984) in the spring of 1980. The displacement sensor of this instrument was a photo-recorder and in 1981 a capacitive transducer developed in the Geodetic and Geophysical Research Institute (GGRI) was mounted. The second extensometer was built at the end of the eighties. This later instrument was equipped with a capacitive sensor (Mentes, 1981, 1991).

In the middle of the nineties extensometric measurements in the observatory were finished due to technical and financial problems. In 2004 these instruments were renewed and equipped with new capacitive sensors which were produced in the GGRI and a new digital data acquisition system was installed by ELGI in the observatory.

In this paper the deformation registrations of the new instruments are presented and compared with the results of the former measurements. On the basis of registrations the influence of environmental parameters are also investigated and possible conclusion on the stability of the observatory is drawn.

2. The Mátyás-hegy Geodynamical Observatory

The Mátyás-hegy Geodynamical Observatory is situated in the NW part of Budapest in a natural cave formed by thermal water in limestone. The level of the karstic water is about a hundred meter deeper than the level of the station. The river Danube flows about 2 km far from the observatory. According to Latinina et al. (1984) the data series recorded earlier does not show any connection with the water level changes of the Danube but they can have a connection with the level variation of the karstic water. The instruments are installed in a distance of about 80-90 m from the entrance and 30-35 m from the surface, so the thermal variation at the instruments is very low, less than 0.1 °C which ensures stable thermal conditions for the extensometers (Varga and Varga, 1994). Figure 1 shows the ground plane of the observatory and the places of the instruments. The station is only a part of a complex cave system separated from it by walls. Thus the caves under and around the station are capable of raising even strong cavity effect in the observatory. The geographical position of the observatory and the parameters of the instruments are given in Table I. Figure 2 shows the

new digital recording and data transfer system of the geodynamical observatory. The data can be on-line transferred to the ELGI. The ADAMS type A/D converters have a resolution of 16 bits and the sampling rate is 1 minute. In the vicinity of each sampling time a simple averaging digital filter is applied over some seconds and it produces the sampled voltage value. Temperature and air pressure data are also measured in the gallery where the instruments are placed.

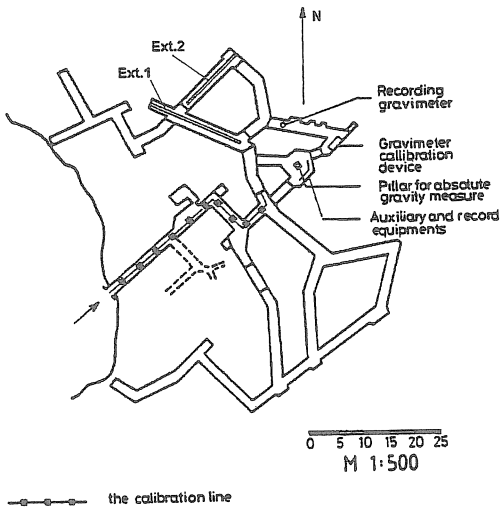

Fig. 1. The ground plane of the Mátyás-hegy Geodynamical Observatory

Table I. The parameters of the observatory and the instruments

Extensometer	Coordinates of the station			Azimuth	Length [m]
	Latitude	Longitude	Altitude [m]		
Ext.1	47°33'	19°01'	202	114°	21.3
Ext.2	47°33'	19°01'	202	38°	13.8

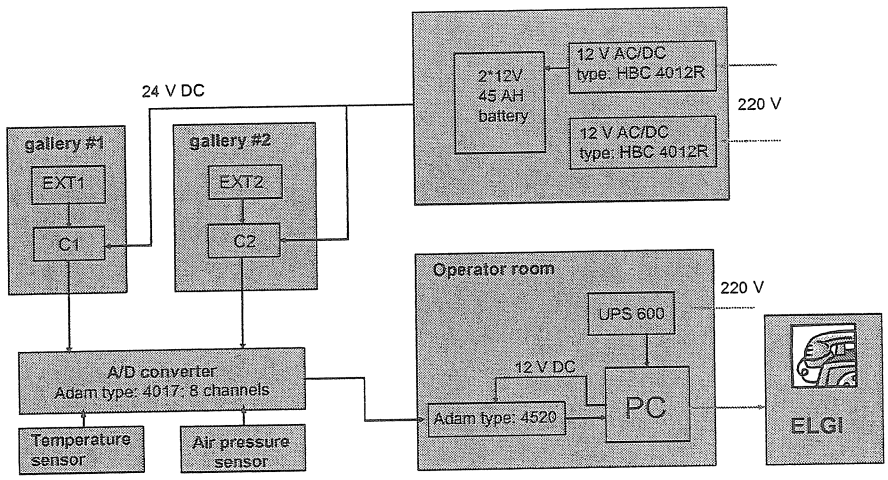

Fig. 2. Digital recording and data transfer system of the geodynamical observatory

3. Analysis of the strain measurements

The rebuilt extensometric station has been working since August 2004. From the measured data series a six months time interval (01. June 2005. - 07. December 2005.) was chosen. These data were processed and analysed in order to obtain information about the deformation measurement. Figure 3 shows the recorded raw data. Strain data of the long (Ext.1) and the short (Ext.2) extensometers along with air pressure and temperature data.

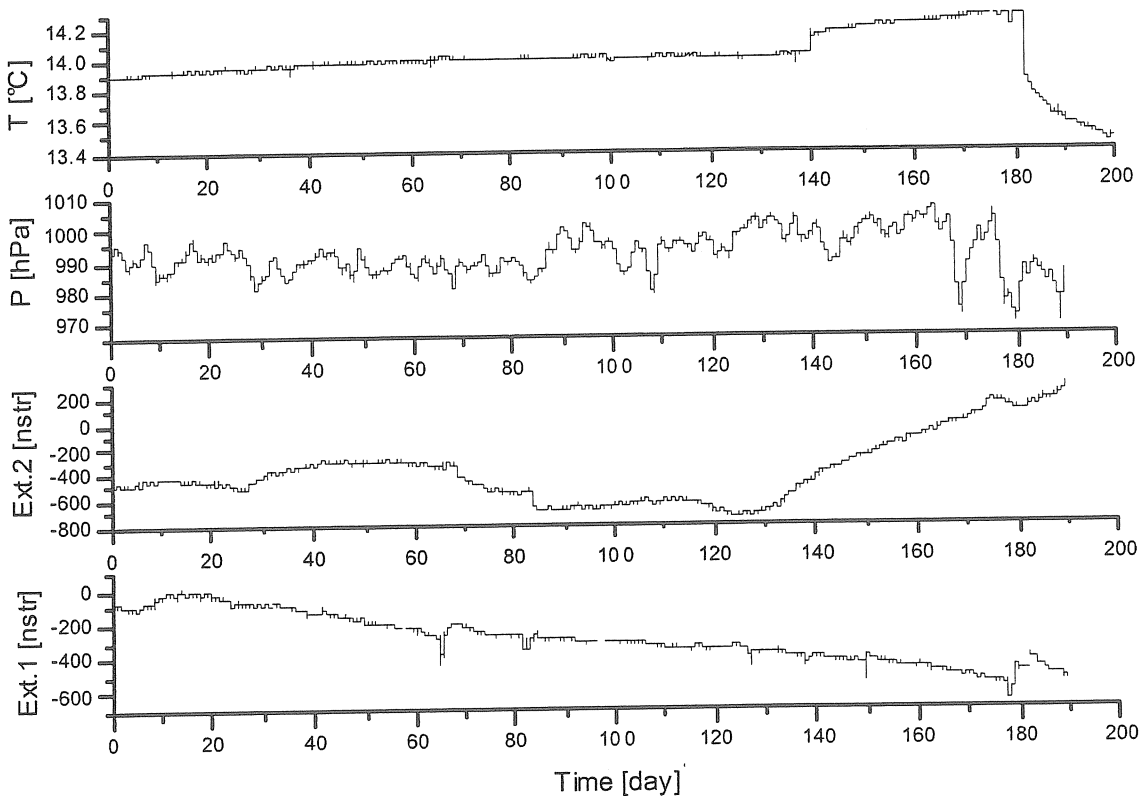

Fig. 3. The measured raw data in the Mátyás-hegy observatory between 01. June 2005 and 07. December 2005

Fourier analysis was carried out on the deformation data series to inspect the behaviour of the instruments in the tidal frequency bands and to get an idea about how successful was the installation of the new electronics onto the quartz tubes. If a clear resolvable tidal spectrum is resulted like in the case of many geodynamical extensometers, the working conditions of our instruments can be regarded as adequate. From Fig. 4. one can observe, that tidal spectrum lines are not obtained from the long extensometer (Ext.1) data – only slightly emerging blurred peaks can be observed in the diurnal band – in contrast with Ext.2 which produces the proper spectral contents of tidal rock deformations. It is obvious that Ext.1 does not work properly and something is erroneous in the instrumental system.

Data of Ext.2 were analysed and processed by Eterna 3.3 software and the results for the tidal constituents are presented in Fig. 5. and the numerical values are listed in Table II.

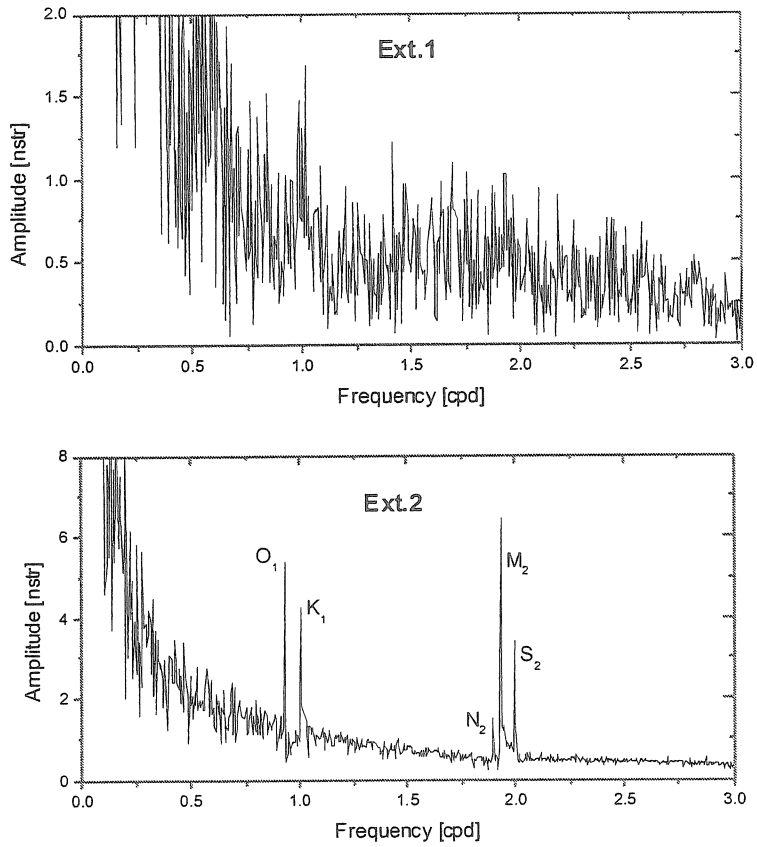

Fig. 4. Fourier amplitude spectra of the extensometric data

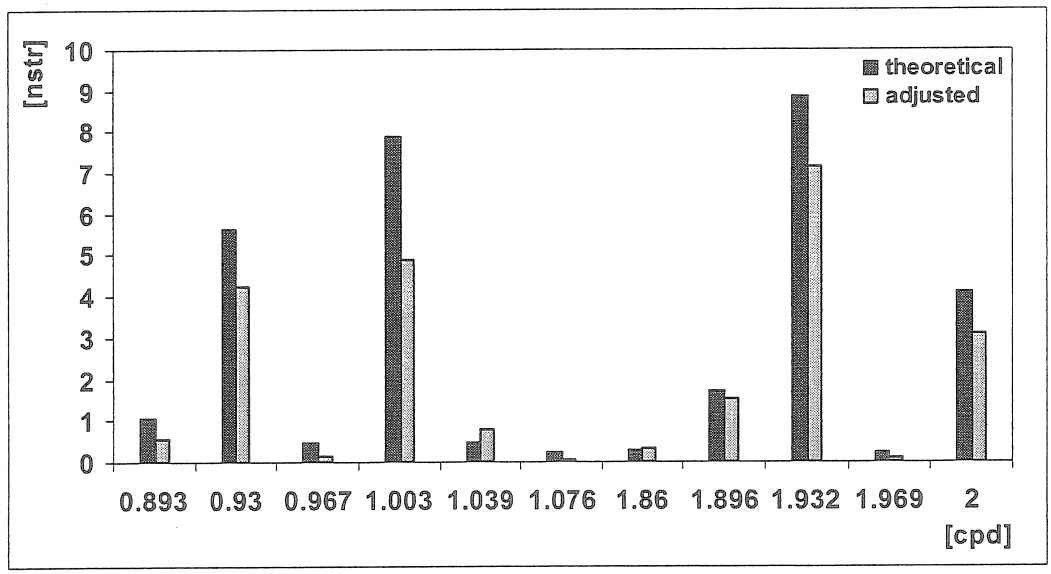

Fig. 5. Theoretical and calculated tidal amplitudes from data series of 01. June 2005.-07. December 2005. time interval, measured by the short extensometer (Ext.2) in the Mátyás-hegy observatory

Table II. Tidal parameters obtained from Ext.2

wave	measured amplitude [nstr]	amplitude factor	standard deviation	phase lead [degree]	standard deviation [degree]
Q_1	0.5424	0.5055	±0.199	-0.564	±22.657
O_1	4.2227	0.7535	±0.044	7.150	±3.365
M_1	0.1339	0.3039	±0.490	-12.791	±92.410
K_1	4.8763	0.6189	±0.038	14.231	±3.476
J_1	0.7639	1.7334	±0.553	50.006	±18.286
N_2	1.5320	0.9059	±0.092	16.384	±5.795
M_2	7.1469	0.8091	±0.018	18.219	±1.304
L_2	0.0894	0.3580	±0.506	-8.9869	±80.999
S_2	3.0990	0.7542	±0.032	20.490	±2.435

The tidal factors in the semidiurnal frequency band are about 15% higher than the amplitude factors obtained in the diurnal frequency band. This situation is similar to the characteristic of tidal adjustment from data of e.g. the Sopron observatory (Mentes and Eper-Pápai, 2006) but the difference between the amplitude factors is smaller in the case of Budapest. The possible cause of the above mentioned difference was investigated by means of Fourier transformation of the residual data (Fig. 6.), from which it can be seen that in the semidiurnal band disturbing deformation effects are present.

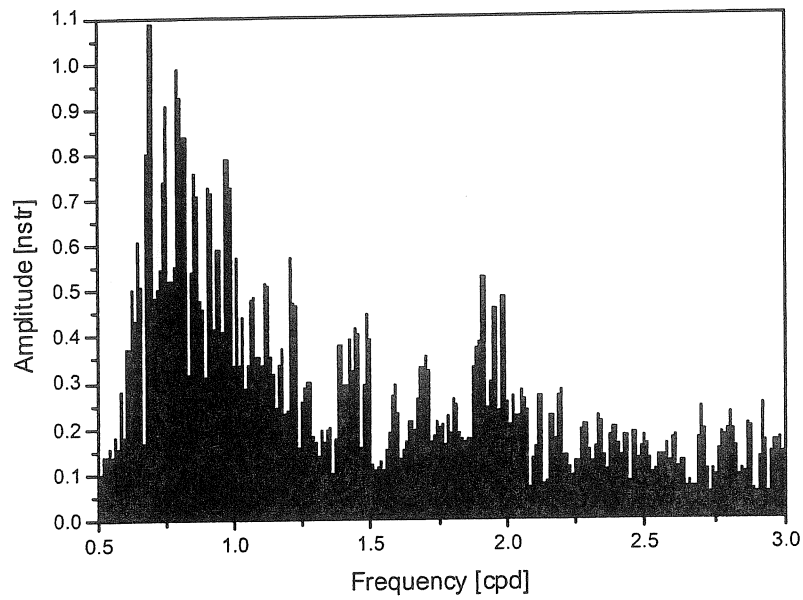

Fig. 6. Amplitude spectrum of the residual curve of Ext.2 data

4. Investigation of the meteorological effects

In spite of the fact that the air pressure and temperature variations were not measured outside the observatory a good estimation of the stability of the station can be achieved using air pressure and temperature data recorded inside the measurement gallery.

In Fig. 3. we can see that no close correlation exists between the strain data and inner temperature and air pressure variations but there are some obvious relationship. The reason of the temperature change of 0.1 °C magnitude in the second half of November (day 140) is still unknown. Presumably the same effect caused both the step in temperature and the change of the direction and the steepness of the strain curve of Ext.2. The second high step in temperature data occurred in the beginning of December (day 180). It obviously induced changes in both strain data series. We can observe from the data that the magnitude of the air pressure variations increased in the second half of November and this effect influenced the strain meters, too. The reason of these effects is still unknown probably they can be in connection with the cave system.

The long-term temperature and air pressure variations inside the station according to the new measurements are 0.3869 °C/year and 0.006 hPa/year. The annual temperature variation is somewhat lower than it was stated earlier (Varga and Varga, 1994).

The long extensometer (Ext.1) was left out from any further investigations due to technical problems of the instrument. In the first step regression method was applied. To calculate the long-term effect a polynomial of ninth order was fitted to the strain curve and it was plotted vs. air pressure and temperature. To get the short-term effect the polynomial was subtracted from the strain data and the remaining curve was also plotted vs. air pressure and temperature. In each case a regression line was calculated and the steepness gives the strain rate caused by temperature and air pressure variations. The results are given in Table III.

Since the temperature variation is very low within the station, its effect onto the strain data could not be calculated reliably. We can assume that the outside temperature variations are more than a hundred times higher than measured inside. In this case the temperature effect values from Table III. should be divided by hundred. The obtained values seem to be realistic: 17.27 nstr/ °C (long-term) and -2.94 nstr/°C (short term).

Table III. Air pressure and temperature effects

	Air pressure effect [nstr/hPa]	Temperature effect [nstr/°C]
Long-term effect	-9.02	1727
Short-term effect	-12.64	-290

Conclusions

Results of the Fourier and tidal analysis show that only the short extensometer (Ext.2) is working properly. The behaviour of the long extensometer (Ext.1) is very interesting. Sometimes it is sensitive to the same disturbances as the Ext.2 as it can be seen in Fig. 3. but it does not record the high frequency tidal deformation variations. The reason can be either of instrumental origin or other effects which obscure the tidal variations.

The analysis of the meteorological effects shows that the station is stable for tidal and tectonic measurements. It means that its sensitivity to the changes of meteorological influences is not higher than in other geodynamical stations of Hungary, in addition on the basis of tidal analysis the Budapest station is more stabile than Sopron from point of view of disturbing deformations induced by environmental effects.

The measurements carried out between 1990 and 1992 (Varga and Varga, 1994) show an average magnitude of the seasonal variations of about 700 nstr which corresponds to the long-term effects calculated by us. Sometimes very steep changes of the displacements occur in the earlier records similarly to the steep change beginning from the day 130 on Ext.2 in Fig. 3. The reason of these changes is unknown. Probably they are in connection with the airing of the surrounding cave system or with the karstic water under the station. To study these irregular changes it would be useful to investigate the level variations of the karstic water and the river Danube during the deformation measurement time periods.

Acknowledgements

This research was supported by the Hungarian National Scientific Research Fund (OTKA) in the frame of the research project T046264.

References

Latinina L A, Szabó Gy, Varga P 1984: Observations of the deformation of the Earth's crust in the „Mátyáshegy"-cave near Budapest. Acta Geod. Geoph. Mont. Hung., Vol. 19 No. 3-4, pp. 197-205.

Mentes Gy 1981: Horizontal pendulum with capacitive transducer. Acta Geod. Geoph. Mont. Hung., Vol. 16, pp. 269-280.

Mentes Gy 1991: Installation of a quartz tube extensometer at the Sopron Observatory. Marees Terrestres Bulletin d'Informations. Bruxelles, No. 110, pp. 7936-7939.

Mentes Gy, Eper-Pápai I. 2006: Investigation of meteorological effects on strain measurements at two stations in Hungary. Journal of Geodynamics, Vol. 41, No. 1-3, pp. 259-267.

Varga P, Varga T 1994: Recent horizontal deformation in the Pannonian basin measured with extensometers. Acta Geod. Geoph. Mont. Hung., Vol. 29, No. 1-2, pp. 57-80.

Observations of fluid induced deformation of the upper crust of the Earth: Investigations about the large scale injection experiment at the KTB site / Germany

T. Jahr[1], G. Jentzsch, and A. Gebauer
Department of Applied Geophysics, Institute of Geosciences, University of Jena, Burgweg 11, D-07749 Jena, Germany

Abstract

A tiltmeter array, consisting of five high resolution borehole tiltmeters of the ASKANIA type, was installed in the surrounding area of the KTB location in mid 2003 (KTB: Continental deep drilling site in Germany). There, an injection experiment of water started in June, 2004. The injection had a medium rate of about 200 liters/minute into the KTB pilot borehole (4000 meters deep). The aim of the research project is to observe and interpret the deformation of the upper crust at kilometre scale. We observe elastic as well as non-elastic responses: Changes of the rheologic properties due to pore pressure increase cause changes in the tidal parameters of M2 and O1. However, these changes are only observed for the north-south direction, which confirms seismological results: The induced seismicity, due to the injection, takes place more northwards of KTB than east- or westwards. Further we expect sudden changes of the drift curve as well as slow variations. For the separation of the induced drift signal it is necessary to eliminate locally induced interference, e.g. arising from groundwater variations or barometric pressure effects. The pore pressure changes observed at all stations show significant correlations with the recorded tilt signals. Taking into account these environmental influences and eliminating them we have now the potential to separate the injection induced deformation signal: During the injection period of about one year the tilt signals of three stations show a significant additional drift oriented from the stations in direction of the KTB site. In the next step these observations will be interpreted by numerical modelling, using a high resolution finite-element-model.

Keywords: KTB injection, fluid dynamics, deformation of the upper crust, tiltmeter observations, geodynamics

1 Introduction

In connection with the development of swarm earthquakes and related stress and strain processes the influence of fluids is more and more discussed. Beside different observations showing the correlation of fluid activities and the occurrence of swarm earthquakes numerical modelling yields some significant hints that the regional stress field alone cannot cause the local stress accumulation in the middle crust of the Earth (Yamashita, 1999; Kurz et al., 2003, 2004). However, the consideration of pore pressure variations in connection with geological features like fault zones and the brittle ductile transient zone in the middle crust results in high local stress accumulations in the crust, which are necessary for the appearance of swarm earthquakes. Up to now the whole process is not completely understood and related large scale experiments were not realized until 2003.

This research project combines a large scale injection experiment with the monitoring of induced seismicity and deformation. The interpretation of the process will be carried out by a high resolution three dimensional numerical modelling, using the finite-element-method. This interpretation can help to improve the knowledge about the interaction of fluid dynamics, stress accumulation, induced deformation and seismic activities, regarding swarm earthquakes.

[1] corresp. author: thomas.jahr@uni-jena.de

2 Tiltmeter-array around KTB

In June, 2004, at the German deep drilling site KTB, a water injection experiment started in the pilot borehole (4000 meters deep), to be completed in May 2005. The injection had a medium rate of 200 liters/minute into the pilot hole. Beside monitoring of induced seismicity by a local network, a tiltmeter array was installed in the surrounding area of the KTB location in mid 2003 (Fig. 1), consisting of five high resolution borehole tiltmeters of the ASKANIA type (Weise et al., 1999). The aim of the research project was to observe the induced deformation of the upper crust at kilometer scale (Jahr et al., 2005). Numerical modelling revealed that pressure built up by the given injection rate would cause a deformation of about 30 nrad within 4 months at the selected stations.

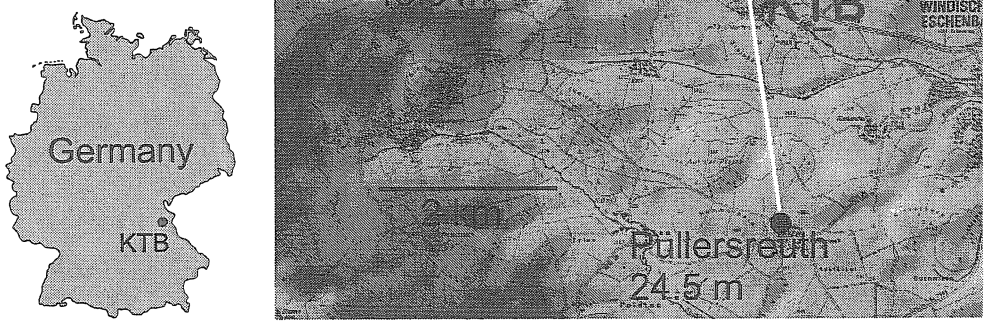

Fig. 1. The area around the KTB-site: The five tiltmeter stations were connected via WLAN to transmit the data on-line. Now the remaining stations Mittelberg, Püllersreuth, Berg and Eiglasdorf are running offline.

The locations of the tiltmeter stations in the vicinity of KTB are at distances of 1.6 to 3.2 km. The instruments are installed in bedrock in depths between 24.5 and 45.5 m depending on the depth of the sediment cover, usually less than 20 m. The tiltmeters are equipped with a 3-D geophone set in order to complete the local seismic network. Next to each tiltmeter borehole in an additional drill hole the groundwater level is monitored as pore pressure variation. Tilt, groundwater level and seismic data were downloaded via a wireless LAN to KTB and further via Internet to the GFZ-Potsdam and the Institute of Geosciences, Jena. The project was carried out in close cooperation with seismologists of the GFZ-Potsdam who operated the seismic network and the WLAN. The wireless connections are given in Fig. 1 as well. Thus, the quality of the raw tiltmeter data and the remotely performed instrument calibration could be checked every day. We also installed a meteorological station at KTB to monitor barometric pressure and precipitation.

2 Observed data

Fig. 2 shows the obtained data until the end of the year 2005. Due to technical problems and the end of funding we had to terminate the recordings at Stockau in August 2005 and the recording systems had to be replaced by systems without WLAN. The tilt data consist of long and uninterrupted sections. The comparison of the tidal amplitudes in the self-scaled plots reveals the different long-term drifts at each station: big tides denote small drifts.

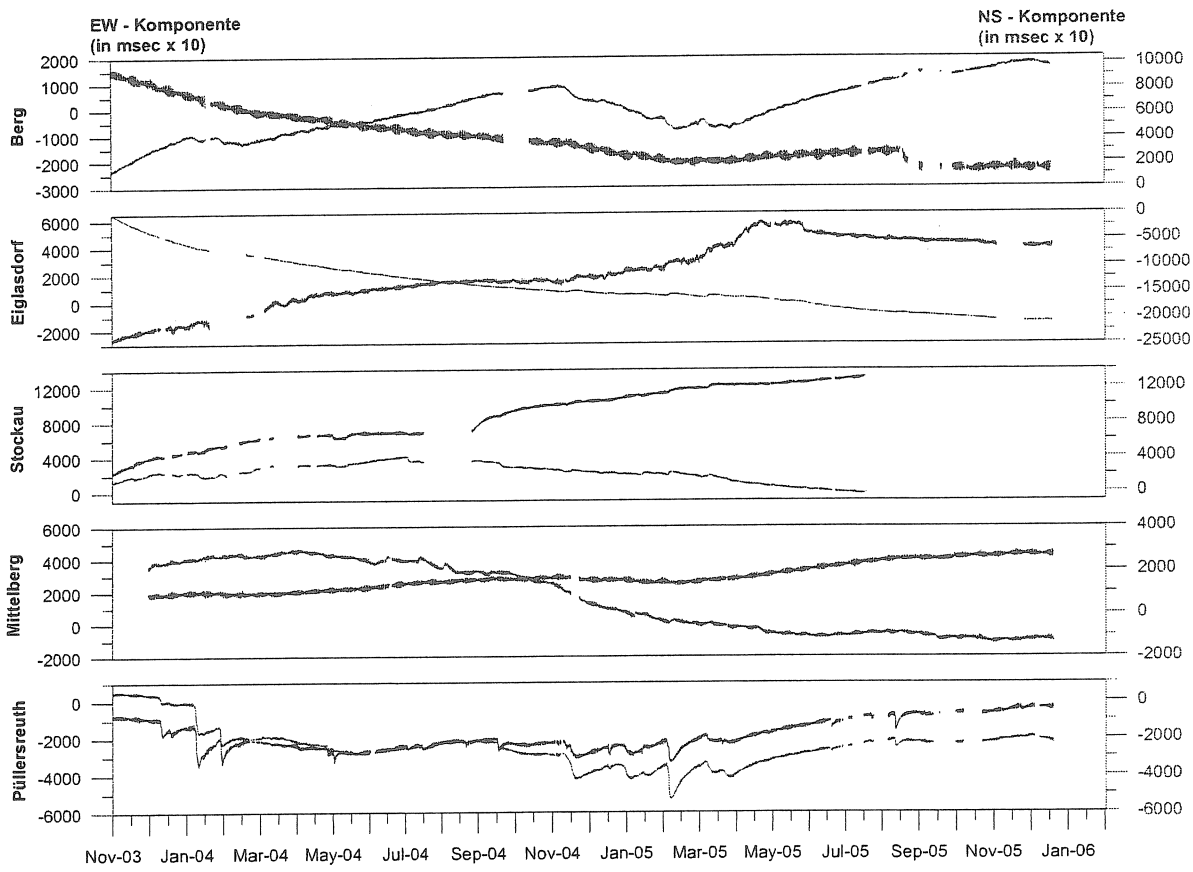

Fig. 2. Tidal recordings: After pre-processing the time series of the tiltmeter observations the drift behaviour can be visualised. The data is displayed in milliseconds of arc times 10 corresponding to about 100 nrad for the maximum tidal amplitudes. Mittelberg shows the lowest drift rates, while in Püllersreuth non-linear effects were caused by heavy precipitation. Data gaps at Eiglasdorf and Berg were caused by malfunctioning data loggers. In Stockau the tiltmeter failed in July 2005.

There are also different reactions to precipitation and local ground water changes. Heavy rainfall usually results in strong deviations with a relaxation of several days. The injection induced variations of tidal parameters, additional drifts of the records (in the order of the tidal amplitudes) and a characteristic movement of the tip of the tiltmeter pendulum (hodogram). The correction of the data for local meteorological effects (precipitation, air pressure) and ground water is in progress.

3 Results and discussion

Although the obtained tidal parameters show a wide scatter, the variations at the individual stations correlate, either no variation or slight variations, respectively. Fig. 3 gives the results for the main tidal constituents M2 (semi-diurnal) and O1 (diurnal): There is a slight change in the parameters corresponding with the injection, here shown for the constituents M2 and O1: Three different periods can be distinguished, before, during and after the injection. The

analyses show a slight increase of the parameters in the component North-South rather than in East-West. This corresponds to the findings regarding the seismicity which increased north of the KTB site. This can be interpretated as an injection induced change of the elasticity of the rock. This result is confirmed by the separated long-term drift. Although these drifts are still preliminary because local effects still have to be analysed and corrected, we can see common trends. Especially these drifts towards the injection center show a surface deformation correlating with the injection induced uplift of the KTB-site. Further, the hodograms reveal drift directions corresponding to geological strikes.

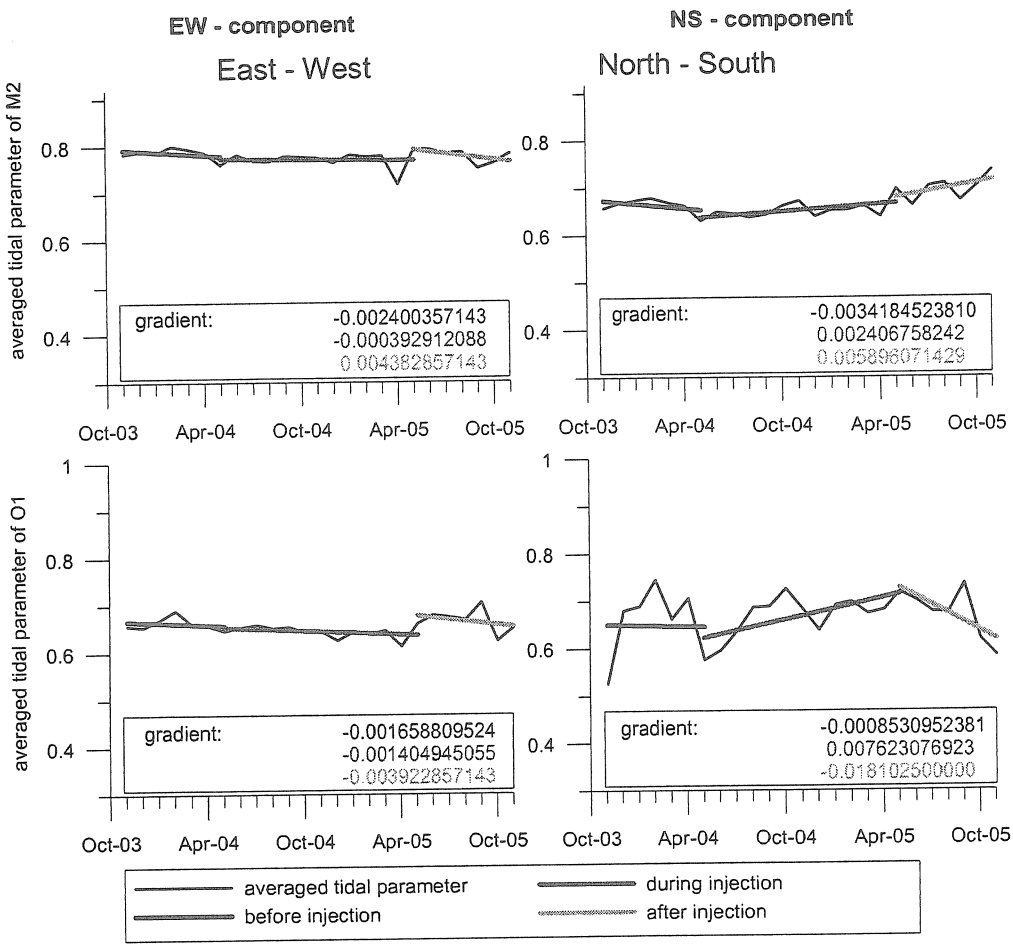

Fig. 3. Variation of tidal parameters of the main tidal constituents M2 and O1: Three different periods can be distinguished, before, during and after the injection. The effect is stronger in North-South than in East-West.

Conclusion

We can summarise that we found three different injection induced effects: Variations of tidal parameters, long-term drifts, and direct elastic tilts. These signals now need numerical interpretation.

The injection tests at KTB were accompanied by induced seismicity (Shapiro et al., 2006). Here, we have a combination of surface deformation and seismicity which was already discussed by Jentzsch et al. (2001). The interpretation with regard to physical properties of the rock and concerning fluid induced processes (Fujimori et al., 2001) will be

done by numerical modelling. We already modelled the expected deformation applying POEL (by R.J. Wang), but for a detailed modelling of the geologic structure we will use the Finite-Element-software ABAQUS. The first model is already under construction (Jahr et al., 2006).

Acknowledgments

We thank the KTB-working group and the Field Support Center for their help. Special thanks go to H. Letz (now IFRC, Genf), G. Asch and J. Kummerow (GFZ, Potsdam) for the organisation of the data collection and transfer. We wish to thank the *Deutsche Forschungsgemeinschaft* for the financial support, although it was not possible to receive funding for the completion of the work.

References

Fujimori, K., H. Ishii, A. Mukai, S. Nakao, S. Matsumoto, and Y. Hirata, (2001). Strain and tilt changes measured during a water injection experiment at the Nojima Fault zone, Japan. *The Island Arc*,10, pp. 228-234.

Jahr, T., Jentzsch, G., Letz, H., Sauter, M., (2005) Fluid injection and surface deformation at the KTB location: modelling of expected tilt effect. Geofluids 5, 20-27p.

Jahr, T., Letz, H. & Jentzsch, G., (2006) Monitoring fluid induced deformation of the earth´s crust: A large scale experiment at the KTB location/Germany. In: Jentzsch, G. (Ed.) Earth Tides and Geodynamics: Probing the Earth at Sub-Seismic Frequencies, J. of Geodynamics, Vol. 41, 1-3, 190 – 197.

Jentzsch, G., P. Malischewsky, M. Zaddro, C. Braitenberg, A. Latynina, E. Bojarsky, T. Verbytzkyy, A. Tikhomirov, and A. Kurskeev, (2001). Relations between different geodynamic parameters and seismicity in areas of high and low seismic hazards. *Proc. 14th International Symposium on Earth Tides, Special Issue of the Journal of the Geodetic Soc. of Japan*, 47/1, 82 – 87.

Kurz, J., T. Jahr & G. Jentzsch, (2003). Geodynamic modelling of the recent stress and strain field in the Vogtland swarm earthquake area using the finite-element-method. – J. Geodyn. 35: 247-258.

Kurz, J., T. Jahr & G. Jentzsch, (2004). Earthquake swarm examples and a look at the generation mechanism of the Vogtland-Western Bohemia earthquake swarms. – Phys. Earth Planet. Int., 142(1): 75-88.

Shapiro, S. A., J. Kummerow, C. Dinske, G. Asch, E. Rothert, J. Erzinger, H.-J. Kümpel, and R. Kind, (2006). Fluid induced seismicity guided by a continental fault: Injection experiment of 2004/2005 at the German Deep Drilling Site (KTB). Geophys. Res. Let., Vol. 33, L01309, doi:10.1029/2005GL024659, 2006

Weise, A., G. Jentzsch, A. Kiviniemi, and J. Kääriäinen, (1999). Comparison of long-period tilt measurements: Results from the two clinometric stations Metsähovi and Lohja, Finland. *J. of Geodynamics*, 27, pp. 237-257.

Yamashita, T., (1999). Pore creation due to fault slip in a fluid-permeated fault zone and its effect on seismicity: Generation mechanism of earthquake swarms. – Pure Appl. Geophys. 155: 625-647.

Observation of crustal deformation by means of wellhead pressure monitoring

H. Woith[*], A.P. Venedikov[**], C. Milkereit[*], M. Parlaktuna[***], A. Pekdeger[****]

[*]GeoForschungsZentrum Potsdam, [**]Geophysical Institute Sofia, [***]Middle East Technical University, Ankara, [****]FU Berlin, Berlin.

Abstract.

The paper represents results from a wellhead station, installed in a 400 m deep artesian well, drilled in the city of Bursa, NW part of Turkey. Water pressure variations are measured by a borehole sensor at a mean pressure level of 1.6 bars. The air-pressure variations are measured in parallel at the surface next to the borehole. The data processed is a series of 421 days (29.04.2004 – 23.06.2005) 5-minutes ordinates. The station is situated in a strongly dangerous seismic region, surrounded by a set of seismic stations. The main objective of the observations is the study of non-tidal signals in pore-pressure related to earthquakes, possibly event precursors. The paper shows how to process the data, in order to reveal anomalies in the residuals, which can be studied as such signals. Namely, the original data are reduced by: (i) a well determined tidal signal, (ii) the effect of the external air-pressure, by using an appropriate model, (iii) a simple polynomial model of the drift and (iv) some annual meteorological waves with basic frequency 1 cycle/year. The estimation and the reduction are made by the tidal program VAV, solving a system of equations by the least squares method, dealing at once in parallel with all components.

1. Introduction.

The paper represents preliminary analysis results from the water pressure records in a wellhead station. The station is installed in a 400 m deep artesian well, drilled in the city of Bursa, NW part of Turkey (Figure 1).

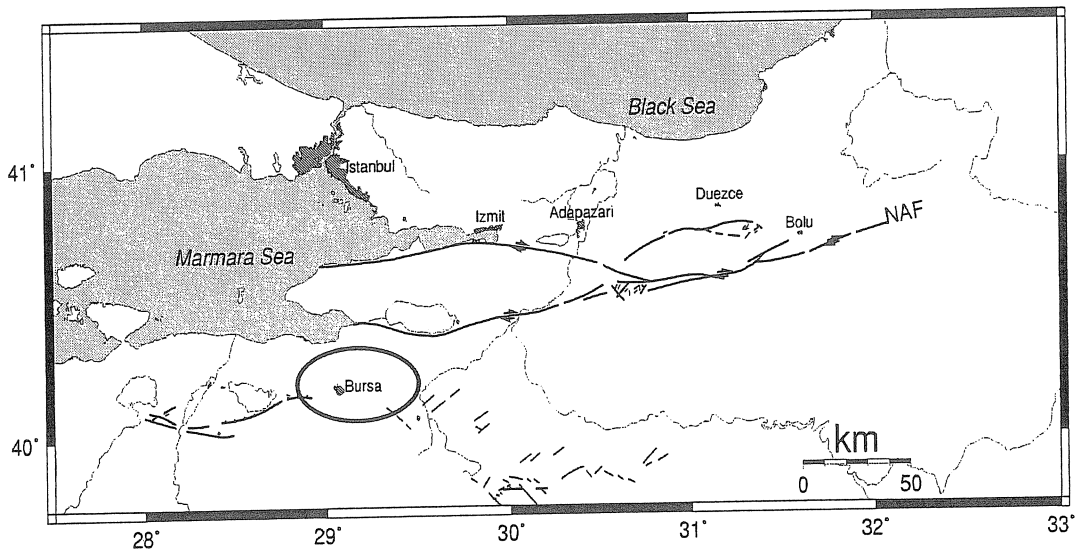

Figure 1. Location of the station in the city of Bursa for wellhead pressure monitoring.

Absolute pressure variations are measured by a borehole pressure sensor at a mean pressure level of 2.6 bars. A second sensor provides relative water pressure, at a mean level of 1.6 bar, the effect of the air-pressure being mechanically reduced (Figure 2).

Air-pressure variations are measured in parallel at the surface a few meters away from the borehole, in order to study their direct and indirect effect on the data.

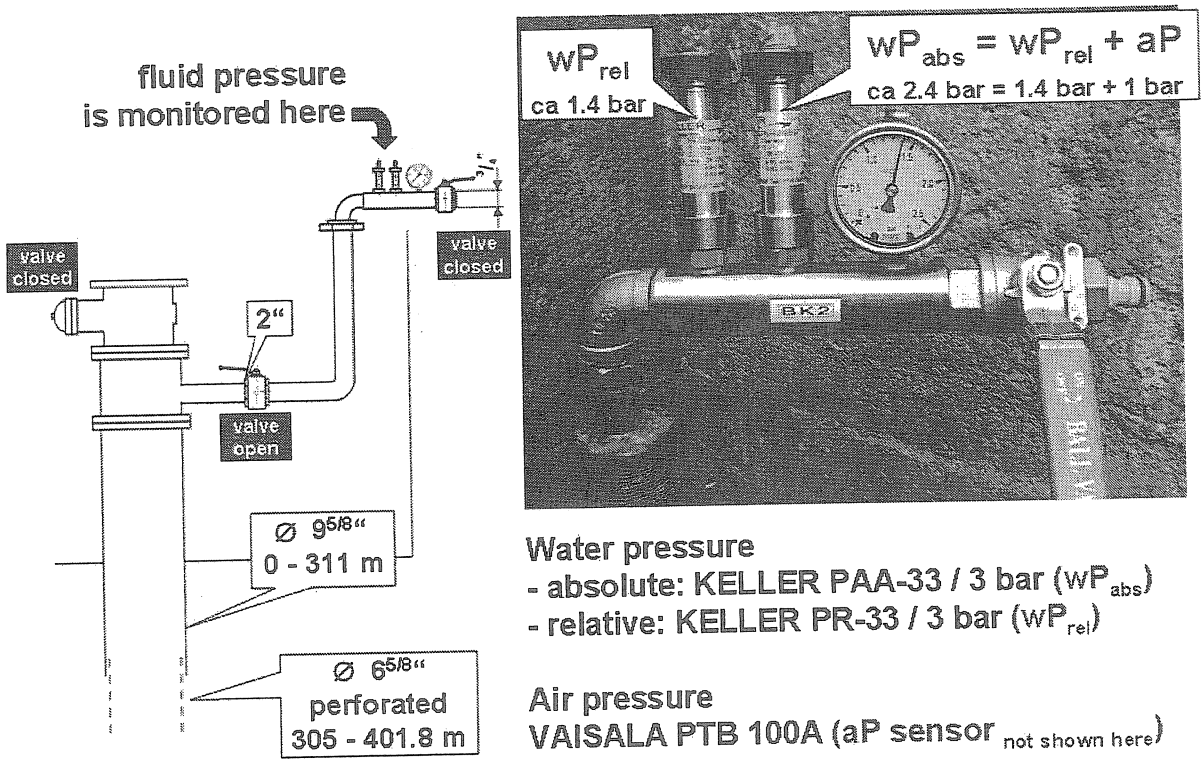

Figure 2 Technical setup of the wellhead pressure monitoring.

The data processed is a series of 421 days (29.04.2004 – 23.06.2005) 5-minutes ordinates. Figure 3 gives an idea about the quality and the properties of the data.

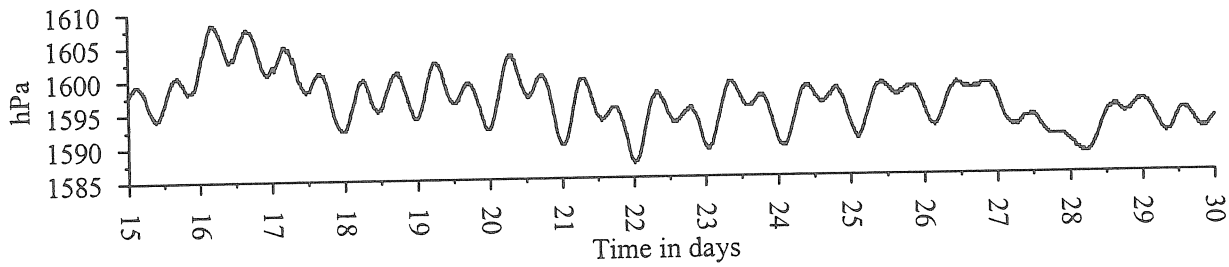

Figure 3. Sample of 15 days of the recorded 5-minutes data.

The station is situated in an active seismic region. The main objective of the investigation is the study of non-tidal signals in pore-pressure related to earthquakes and its potential as earthquake precursors.. This task needs at first place high quality tidal data with an as good as possible determination of the tidal signal and thus - as good as possible separation of the non-tidal signals.

The aims of the investigation need also the reduction of the meteorological effects. The effect of the air-pressure is taken into account by a multi-channel and a cross-regression analysis, by using an appropriate model.

The temperature variations now are not included in the data and. Instead, their effect is reduced by including in the processing annual components with basic frequency 1 cycle/year.

3. General model applied by the VAV program.

The algorithm of VAV (Venedikov et al., 2004) is based on the partition of the data in a set of intervals without overlapping $I(T)$ with central epoch $T = T_1, T_2, \ldots T_N$ and length $\Delta T = T_{i+1} - T_i$ hours (when there are no gaps). Independently in every $I(T)$ the drift of the data is represented by a polynomial of power K_d.

In this case a most simple but rather efficient variant is used with $\Delta T = 24^h$ and $K_d = 0$. This variant is accompanied by a determination of the LP tides in parallel with the other tidal groups. For the LP tides a single group Mf is used (Ducarme et al., 2004).

Since the data are taken every 5 min., every $I(T)$ covers 288 consecutive 5-minutes data.

The data in the $I(T)$ are transformed into a set of complex filtered quantities, by using

$$u_\nu(T) = \sum_\tau F_\nu(\tau) y(T+\tau) \quad \nu = 1,2,\ldots 6, \; T = T_1, T_2, \ldots T_N \tag{1}$$

where τ is internal time in the $I(T)$, which vary from -717.5^m to +717.5^m through 5^m.

When dealing with the quantities $u(T)$ obtained by (1) for every dsy, the time T is expressed in days

The filtration is made by using a set of orthogonal filters $F_\nu(\tau)$, which are complex functions of the internal time τ. For the case here used $\Delta T = 24$ hours = 1 day and $K_d = 0$ the filters are the Fourier operators

$$F_\nu(\tau) = \sqrt{2/288}.\mathrm{Exp}\left(\frac{2\pi\nu}{1440}\tau\right) \text{ amplifying frequency } \nu = 1,2,\ldots 6 \text{ cpd respectively.} \tag{2}$$

The filters $F_\nu(\tau)$ eliminate an arbitrary constant, i.e. a polynomial of power $K_d = 0$.

In connection with the concrete task, VAV uses the so called zero option (Venedikov et al., 2004), used also for the study of the polar motion (Ducarme et al., 2005, 2006), which includes in the set (1) a zero filtered number $u_0(T)$. The latter is a real number, equal to the arithmetic mean of the data in $I(T)$.

Further VAV creates a system of observational equations about the filtered numbers, which generally looks like

$$\left.\begin{aligned} u_1(T) &= S_1(T) + M_1(T) \\ u_2(T) &= S_2(T) + M_2(T) \\ &\cdots\cdots\cdots \\ u_6(T) &= S_6(T) + M_6(T) \\ u_0(T) &= S_0(T) + M_0(T) + D(T) + A(T) \end{aligned}\right\} \; T = T_1, T_2, \ldots T_N \tag{3}$$

Here $S_\nu(T)$, $\nu = 0,1,...6$ is the model of the tidal signal, used in the tidal analysis. As said above, this model includes a common LP tidal group MF (Ducarme et al., 2004). The terms $M_\nu(T)$, $\nu = 1,...6$, i.e. for $\nu > 0$ represents the multi-channel model used by VAV for the frequency dependent effect of the air-pressure on the D, SD, ... filtered numbers $u_\nu(T)$ for $\nu > 0$.

The term $M_0(T)$, together with the terms $D(T)$ & $A(T)$ are included in the model of $u_0(T)$ because the corresponding filter (arithmetic mean), unlike the filters $F_\nu(\tau)$ for $\nu > 0$, does not eliminate the drift and the slow meteorological effects. Concretely, $M_0(T)$ is a particular model of the effect of the effect of the air-pressure, $D(T)$ is a polynomial model of the drift, i.e. its manifestation in the central epochs T and $A(T)$ is a term, represented low frequency meteorological effect, mainly connected with the annual variations of the temperature.

After the joint solution of the system (3) we get the adjusted quantities $\tilde{S}_\nu(T), \tilde{M}_\nu(T), \tilde{D}(T)$ & $\tilde{A}(T)$ of $S_\nu(T), M_\nu(T), D(T)$ & $A(T)$ respectively. They are used to get for every day the residuals of the zero filtered number

$$\Delta u_0(T) = u_0(T) - \tilde{S}_0(T) - \tilde{M}_0(T) - \tilde{D}(T) - \tilde{A}(T) \qquad (4)$$

where we expect to find particular anomalies as signals, which can be studied as potential earthquake precursors.

4. The tidal signal $S_\nu(T)$.

With respect to the tidal signal $S_\nu(T)$, the common solution of (3), including the equations for $u_0(T)$, does not create particular problems. As said above, it is necessary to include an LP group MF, as it is done by (Ducarme et al., 2004).

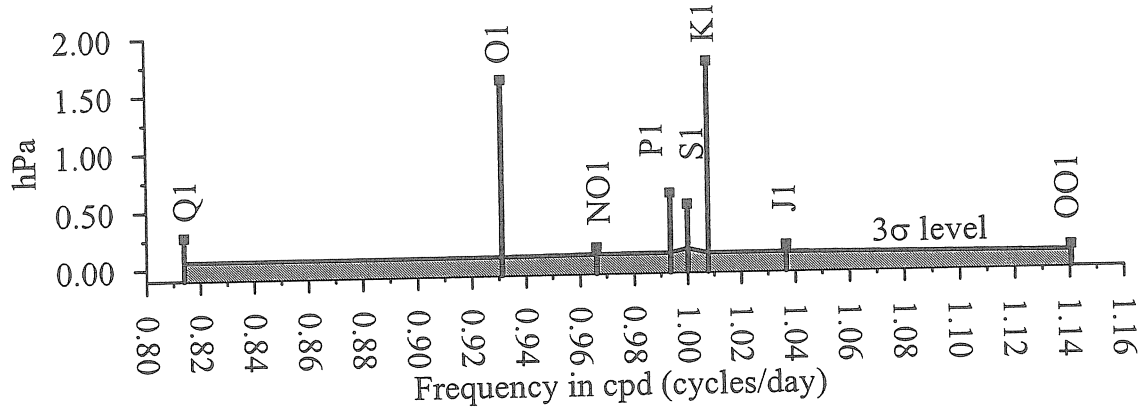

Figure 4. Estimated amplitudes of the main D tides with the 3σ confidence level, where σ denotes RMS (root mean square error) of the corresponding amplitudes.

Figures 4 & 5 show the estimated D and SD amplitudes of the main tides. The comparison with the 3σ level, which is a rather high level, shows that all amplitudes are certainly statistically significant. Thus we dispose by rather satisfactory results, which testify for a good quality of the data.

The result, obtained for the amplitude of the MF tide is 0.406 ± 0.124 hPa, i.e. even for the LP tides we get statistically significant result with confidence probability higher than 95%.

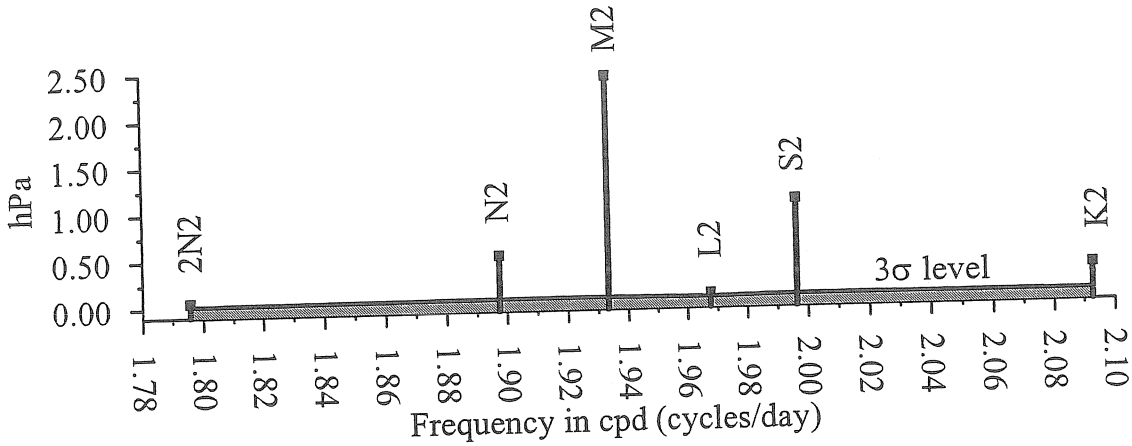

Figure 5. Estimated amplitudes of the main SD tides with the 3σ confidence level.

Figure 6 shows the data $u_0(T)$ reduced by the estimated effect of the tidal signal $S(T)$, i.e. the non-tidal component of the data, usually considered as the drift of the data.

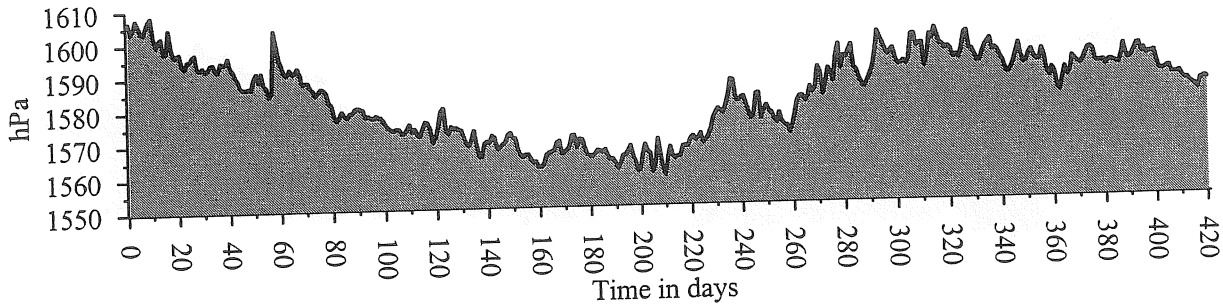

Figure 6. The non-tidal component of the data as partial residual $u_0(T) - \tilde{S}_0(T)$

4. The effect of the air-pressure $M_0(T)$.

The model used for $M_0(T)$ is the following. We set up

$$M_0(T) = R_p p(T - \Delta T) \tag{5}$$

where $p(T-\Delta T)$ is the air-pressure at time $T-\Delta T$, ΔT is unknown time lag, positive for retardation and R_p is unknown regression coefficient.

The problem of using this model in (3) is that the unknown ΔT enters non-linearly in the equations, i.e. it cannot be estimated by the LS. This problem has been solved by solving the system (3) for a set of values of ΔT and thus obtaining $R_p = R_p(\Delta T)$ as a function of ΔT, looking for the minimum of this function. As shown by Figure 6, the minimum has been found at $\Delta T = -2^h$, i.e. for 2 hours of advance. Once fixed the value $\Delta T = -2^h$, there were no more problems for solving (3) by the LS.

The estimate of the regression coefficient obtained is

$$R_p = -0.466 \pm 0.022 \text{ (hPa in water)/ hPa air-pressure at the surface)} \quad (6)$$

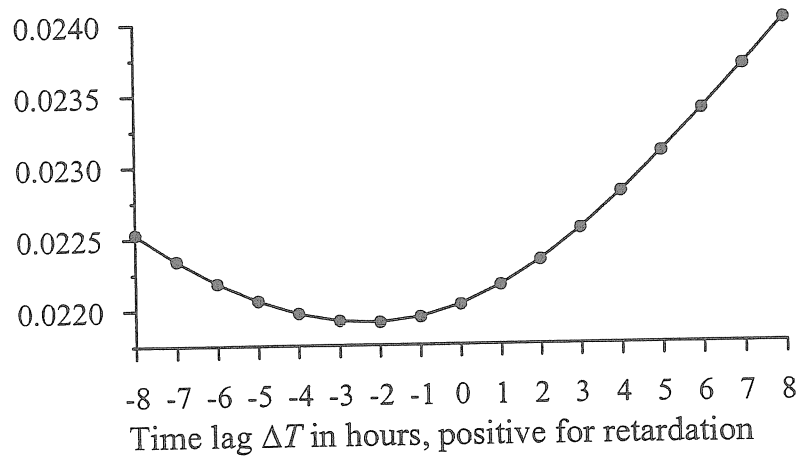

Figure 7. RMS of the regression coefficient $R_p = R_p(\Delta T)$ as a function of ΔT.

In the next Figure 8, the data $u_0(T)$ are reduced by the tidal signal, as well as by the effect of the air-pressure $M_0(T)$.

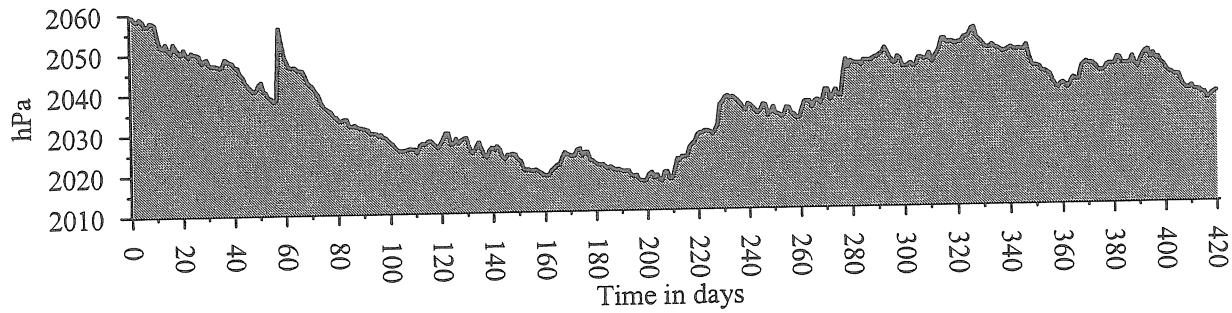

Figure 8. Partial residuals $u_0(T) - \tilde{S}_0(T) - \tilde{M}_0(T)$.

The comparison between Figure 6 and Figure 8 show that the inclusion of $M_0(T)$ is efficient, because we get a better smoothed curve, in which a lot of small anomalies, which could be misleading, are suppressed.

5. Polynomial component and annual component.

For the polynomial component $D(T)$ we have chosen the simple model

$$D(T) = b_0 + b_1 T + b_2 T^2 \quad (7)$$

with unknown coefficients b_j. Using higher powers of (7) appeared to be not suitable, first, in order to observe the principle of the parsimony and second, because they interfere with the annual component. Namely, when high powers are used, we start getting unreasonably great amplitudes of the annual component.

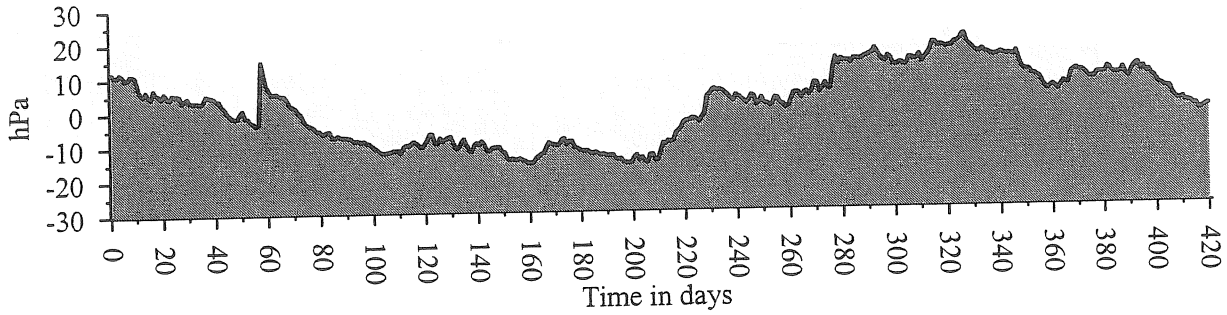

Figure 9. Partial residuals $u_0(T) - \tilde{S}_0(T) - \tilde{M}_0(T) - \tilde{D}(T)$.

Figure 9 shows the effect of $D(T)$, which is mainly a reduction of the curve to the horizontal zero line.

For the annual component $A(T)$, by having in mind the length of the data (421 days), as well as that $A(T)$ is designed to represent some meteorological phenomena, mainly the temperature variations, we have used a Fourier series with basic period one year. An optimum has been obtained to go till order 4, i.e. we have applied

$$A(T) = \sum_{k=1}^{4} \left(\alpha_k \cos \omega_k T + \beta_k \sin \omega_k T \right), \quad \omega_k = 2\pi k / 365.25 \tag{8}$$

with unknowns α_k & β_k and the time T expressed in days.

Figure 10 shows the final result of the reduction of the data, after $A(T)$ had joint the other reduced components. The comparison with Figures 6, 7 and 8 shows that $A(T)$ has a rather important effect.

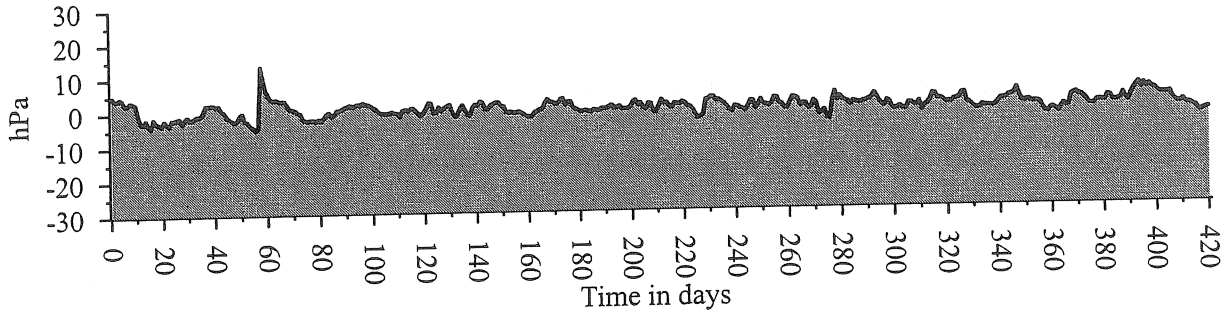

Figure 10. Finally obtained residuals $\Delta u_0(T) = u_0(T) - \tilde{S}_0(T) - \tilde{M}_0(T) - \tilde{D}(T) - \tilde{A}(T)$ after the LS solution of the system (3).

6. Final representation and conclusions.

Figure 11 uses an elementary way to better visualize the residuals, namely by plotting their absolute values. This is possible can because when we are studying the anomalies, it makes no difference whether they are positive or negative.

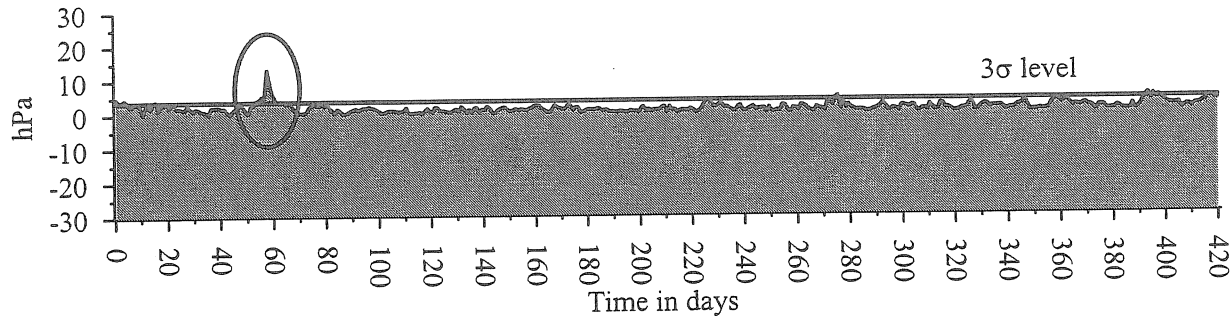

Figure 11. Absolute residuals $|\Delta u_0(T)| = |u_0(T) - \tilde{S}_0(T) - \tilde{M}_0(T) - \tilde{D}(T) - \tilde{A}(T)|$ and a 3σ threshold level.

More essential is that in such cases we have to use statistical criteria. In Figure 11 the criterion used is the 3σ level, where σ is computed as

$$\sigma = \sqrt{\sum_T \Delta u_0^2(T) / n_{\Delta u}} \tag{9}$$

where $n_{\Delta u}$ is the number of the residuals.

When given $\Delta u_0(T)$ exceeds this level we can firmly believe that it is an anomalous residual with a high enough confidence probability.

Thus Figure 11 allowed us to clearly distinguish an anomaly, surrounded by a circle.

The aims of the paper are to show one way for a careful analysis of the data, when their purpose is the difficult problem for finding earthquake precursors. At the first place we need high quality of data from which we can obtain reliable tidal signal, in order to eliminate it. Further we have to carefully create regression models for other components, like here for the air-pressure, polynomial component and annual terms.

We would like to emphasis that the use of one and the same program for the solution of the purely tidal and non-tidal tasks is corresponding to a fundamental LS principle. According to the LS principle it is necessary to include simultaneously in one common system of equations, like (3), all models and get in parallel the estimate of all unknowns.

In practice very often this LS principle is violated by estimating and subtracting consecutively and independently the components, whose effect has to be reduced.

The series of data here used is experimental and very short for checking whether the anomaly in Figure 11 is really related to an earthquake or not. Such conclusion needs much larger experimental material and sophisticated statistics, studying the relation between a great number of anomalies and seismic events.

References.

1. Ducarme B., Venedikov A.P., Arnoso J., Vieira R., 2004. Determination of the long period tidal waves in the GGP superconducting gravity data. *Journal of Geodynamics*, 38, 307-324.

2. Ducarme B., Van Ruymbeke M., Venedikov A.P., Arnoso J., Vieira R., 2005. Polar motion and non-tidal signals in the superconducting gravimeter observations in Brussels. *Bulletin d'Informations des Marées Terrestres*, 140, 11153-11171.

3. Ducarme B., Venedikov A.P., Arnoso J., Chen X.D., Sun H.P., Vieira R., 2006. Global analysis of the GGP superconducting gravimeters network for the estimation of the polar motion effect on the gravity variations. *Journal of Geodynamics*, 41, 334-344.

4. Venedikov A.P., Vieira R., 2004. Guidebook for the practical use of the computer program VAV – version 2003. *Bulletin d'Informations des Marées Terrestres*, 139, 11037-11102.

Strain data and seismicity

Varga Péter,Mentes Gyula

Geodetic and Geophysical Research Institute
H-9401, Sopron POB 5, Hungary
(E-mails: varga@seismology.hu, mentes@seismology.hu)

1.Introduction

The study of the displacement fields of the Earth surface can be useful in the study of the properties of the past and future potential earthquakes. With the use of Kostrov equation (*1974*) the possible sum of seismic moments can be estimated for a given source zone, if its area is described with the use of geodetic measurements. The possible displacement fields connected with seismo-tectonic activity should be estimated with the use of model calculations. The necessity of such a theoretical work is connected with the very long return period of destroying events (M≥ 6.5).

2. Some problems of the seismicity of the Earth

Since the birth of modern instrumental seismology at the end of XIXth century elapsed a little more than a century. In the same time the return period of characteristic seismic events even in case of most active seismic sources is well above hundred year. This circumstance makes extremely complicated to make predictions concerning future seismic events. To illustrate the deficiency of our knowledge serves as an example a comparison of seismicity of two seismic zones. (Table 1). It can be seen that the seismicity data concerning the Tangshan region just before the most destroying earthquake of XXth century (28 July !976, M=7.8) were very similar to those in Komarom with medium seismicity region of the Pannonian basin.

Table 1. Earthquakes in Tangshan and Komarom prior 1976.

Tangshan				Komárom			
Year	Epicentral intensity	M	Energy (Joule)	Year	Epicentral intensity	M	Energy (Joule)
1527	VII	5.5	$1.10\cdot10^{13}$	1599	VIII	5.6	$1.58\cdot10^{13}$
1567	VI	4.8	$8.41\cdot10^{11}$	1754	V	3.8	$3.16\cdot10^{10}$
1624	VII	6.3	$1.50\cdot10^{14}$	1759	V	3.8	$3.16\cdot10^{10}$
1795	VI-VII	5.3	$4.73\cdot10^{12}$	1763	IX	6.2	$1.26\cdot10^{14}$
1805	VII	5.5	$1.12\cdot10^{13}$	1783	VIII	5.3	$5.62\cdot10^{12}$
1880	VI	5.0	$2.00\cdot10^{12}$	1806	VII	5.0	$2.00\cdot10^{12}$
1934	VI	5.0	$2.00\cdot10^{12}$	1822	VI-VII	4.7	$7.08\cdot10^{11}$
1935	VI	5.0	$2.00\cdot10^{12}$	1822	VI	4.4	$2.51\cdot10^{11}$
1945	VIII	6.3	$1.50\cdot10^{14}$	1851	VII	5.0	$2.00\cdot10^{12}$
1974	V-VI	4.8	$1.00\cdot10^{12}$	1857	V	3.8	$3.16\cdot10^{10}$
1974	V-VI	4.8	$1.00\cdot10^{12}$	1923	V	3.8	$3.16\cdot10^{10}$

It can be concluded that between the first half of XVIth century and 1976 the number of the earthquakes with epicentral intensity ≥V was the same in case of both seismic sources and the energy released during this time interval was also similar ($3.35 \cdot 10^{14}$ and $1.52 \cdot 10^{14}$ Joule respectively).

From the five largest known earthquakes (M≥9) ever observed four was connected to the Pacific region and only one occurred outside from this area:

Chile (1960,*M*=9.5)
Alaska (1964,*M*=9.2)
Alaska (1957,*M*=9.1)
Kamchatka (1952,*M*=9.0)
Sumatra (2004,M=9.0)

It is remarkable that the four greatest seismic events of the Pacific region occurred in twelve years

The most of the seismic energy is released by the biggest earthquakes:92% of the seismic energy is connected to seismic events M≥7 (Table 2).

Table 2. Annual number and energy released by earthquakes of different magnitude classes.

Magnitudes	Annual average number	Contribution to the annual seismic energy
M≥8	1	49%
7.9≤*M*≥7	10	43%
6.9≤*M*≥6	10^2	4%
5.9≤*M*≥5	10^3	3%
4.9≤*M*≥4	10^4	1%

When the annual seismicity is discussed one should keep in mind that our knowledge globally is still not complete for the seismic events M≤ 5.0 (Fig.1). If the seismicity of the whole XXth century is considered it can be concluded that our earthquake catalogue is complete only for the seismic events above M=7, what means that we are able to describe the temporal distribution of 92 % of seismic energy only.

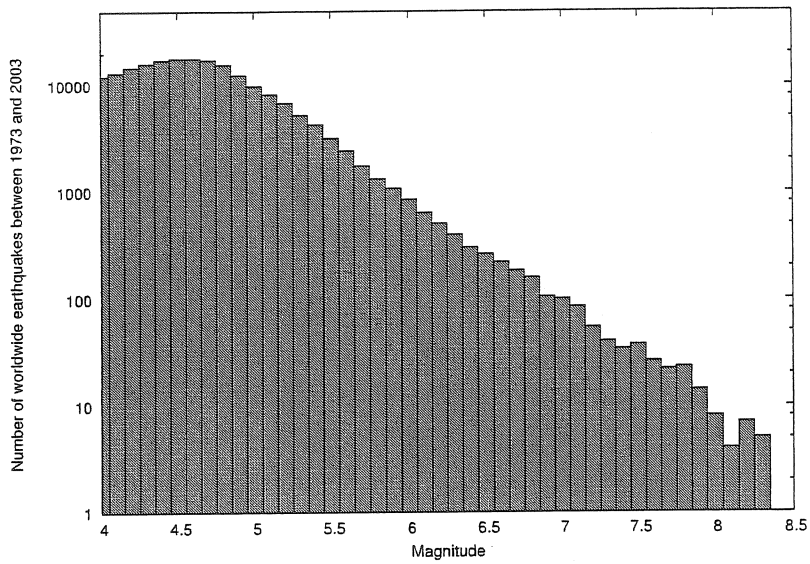

Fig.1 Histogram of earthquakes of the world for 1973-2004

In Section 4 we shall try to determine the volume of the earthquake source. For this purpose the determination of the aftershock area *A* is needed, which can be obtained with the use of the equation (*Kasahara, 1981*)

$$Lg\ A = 6.0 + 1.02 \cdot M \qquad (1)$$

(*A* is expressed in cm^2)

A short study of Eq.1 shows that in case of

M= 6.0 we have $A=1.3 \cdot 10^2$ km^2
M= 7.0 $A=1.4 \cdot 10^3$ km^2
M= 8.0 $A=1.4 \cdot 10^4$ km^2
M= 9.0 $A= 1.5 \cdot 10^5$ km^2
M= 9.5 $A= 4.9 \cdot 10^5$ km^2
M=10.0 $A= 1.6 \cdot 10^6$ km^2
M=10.5 $A= 5.1 \cdot 10^6$ km^2

From what follows that probably there is no possibility for generation earthquakes significantly bigger than M=10, because there is not seismic source zone on the Earth with area is big enough to generate such a giant seismic event.

3. Strain rates and their determination with the use of seismological data.

In geodesy the strain is determined as the ratio of the length variation to the total length $\varepsilon=\Delta L/L$ and the strain rate is $\frac{d\varepsilon}{dt} \approx \frac{\varepsilon}{\Delta T}$. Of course the strain has no units while the strain rate is usually expressed in $year^{-1}$.

It is worth to mention here that the seismic strain is $\Delta\varepsilon = \frac{D}{L^F}$ (*D* - dislocation, L^F - fault length). Approximately $\Delta\varepsilon \approx DA^{-1/2}$. Here *A* is the contact area expressed in the same units like *D*. Kasahara (*1981*) has found that the maximal share rate is

$$\frac{d\varepsilon}{dt} = \frac{p}{\mu \cdot \Delta t} \qquad (2)$$

In above expression p is the tensional strength ($p \leq 10^7$ Nm^{-2}), μ serves for the shear modulus ($\approx 3 \cdot 10^{10}$ Nm^{-2}) and Δt is the time-interval between the characteristic earthquakes.

The individual fault or system of faults have a preferred magnitude (*Huang et al., 1998*), an earthquake at which exhausts the seismic storage potential of the system, which must then recovered over a period of some time. An event of this magnitude is called characteristic earthquake. With the use of equation (2) if

$$\frac{d\varepsilon}{dt} \approx 10^{-6} \text{ then } \quad \Delta t \approx 10^2 \text{ year}$$

$$\frac{d\varepsilon}{dt} \approx 10^{-7} \quad \Delta t \approx 10^3 \text{ year}$$

$$\frac{d\varepsilon}{dt} \approx 10^{-8} \quad \Delta t \approx 10^4 \text{ year}$$

The statistical mean of the strain rates determined with strainmeters worldwide is (*Varga, 1984*):

$$\frac{d\varepsilon}{dt} = 2.1 \cdot 10^{-6} \text{ year}^{-}$$

The seismic strain rate according to Kostrov (*1974*) can be related to the sum of the seismic moment tensors of the earthquakes occurring in a volume ΔV during a time-interval Δt :

$$\frac{d\varepsilon}{dt} = \frac{\sum_{n=1}^{N} M_{0ni}}{2\mu \Delta t \Delta V} \qquad (3)$$

If the orientation of the seismic sources is replaced by their average the seismic moment M_0 can be introduced in equation (3) instead of M_{0ni}

$$\frac{d\varepsilon}{dt} \approx \frac{\sum_{n=1}^{N} M_{0n}}{2\mu \Delta t \Delta V} \qquad (4)$$

The value of the seismic moment M_0 can be derived from the value of momentum magnitude M_W (*Hanks and Kanamori 1979*)

$$\mathrm{Lg}M_0 = 1.50 M_W + 10.70$$

4. Strain rates derived from earthquake data and their connection to the return period of characteristic earthquakes.

Let us consider that in equation (4) Δt=250 year. The surface of the source volume can be estimated with the use of equation (1) and its thickness one can obtain if it is supposed that the focal depth is in the middle of the layer in which the stress accumulation takes place. In Table 3 the strain rates obtained with the use of equation(4) are listed for the case of the five greatest earthquake observed until now.

Table 3. Seismic strain rate values obtained for the earthquakes $M_W \geq 9.0$.

Place	Year	Mw	M_0 10^{22} Nm	Aftershock area (calc.) 10^5 km^2	Aftershock area (obs.) 10^5 km^2	Volume 10^6 km^3	dε/dt
Kamchatka	1952	9.0	3.9	1.5		3.0	$8.6 \cdot 10^{-7}$
Alaska	1957	9.1	5.6	1.9		3.8	$9.8 \cdot 10^{-7}$
Chile	1960	9.5	22.1	4.9		9.8	$1.5 \cdot 10^{-6}$
Alaska	1964	9.2	7.9	2.4	2.0	4.8	$1.1 \cdot 10^{-6}$
North Sumatra	2004	9.0	3.5	1.5	1.8	3.0	$8.6 \cdot 10^{-7}$

In Table 3 the observed aftershock areas Alaska (1964) and the North Sumatra (2004) earthquakes are compared with the results obtained with the use of Eq. 1. It can be concluded that the calculated and the observed aftershock areas show good agreement.

Table 4 shows seismic strain rates of some arbitrary selected significant and medium earthquakes. The two last examples are the most significant seismic events of the Pannonian basin (*Zsíros, 2000*). The case of the Dunaharaszti earthquake demonstrates that the estimation with equation (1) is in a good agreement with observations of the aftershock area is in case of medium size earthquakes too.

Both in the case of giant ($M_W \geq 9.0$) and smaller earthquakes listed in Table 4 it was supposed that the sum in the r.h.s. of equation (4) is determined by the most significant seismic event of the source area,. what is - as it was shown in *Varga et al., 2004* - a rather good estimation of the reality.

Table 4. Seismic strain rate values obtained for great and medium earthquakes.

Place	Year	Mw	M_0 1019 Nm	Aftershock area (calc.) 10^2 km^2	Aftershock area (obs.) 10^5 km^2	Volume 10^3km^3	dε/dt
Gujarat	2001	7.6	32.2	95.52		95.84	$5.0 \cdot 10^{-4}$
Kobe	1995	6.9	2.8	11.05		22.10	$3.3 \cdot 10^{-5}$
Boumerdes	2003	6.8	2.0	8.63		17.26	$2.8 \cdot 10^{-5}$
Komárom	1763	6.3	0.4	4.27		5.97	$1.2 \cdot 10^{-5}$
Dunaharaszti	2004	5.6	0.04	7.58	7.96	0.15	$2.3 \cdot 10^{-6}$

The seismic rates $\frac{d\varepsilon}{dt}$ obtained in case of great and medium seismic events are relatively big. It is probable that in these cases $\Delta t=250$ year is unrealistic and a much bigger time-interval should be considered.

It can be concluded from calculation results of Tables 3 and 4 that the timei-nterval between the characteristic earthquakes of a seismic zone can be estimated on the basis of accurate geodetic observations. For this purpose however in case of GPS measurements 10^{-8} relative accuracy is needed on the base of 30-40 km what is not possible at present. In case of strainmeter observations this accuracy is waranted on the base less then 100 m, but the strain rate values of these records are suffering because of local tectonical, meteorological and hydrological influences. Nevertheless the strainmeter observation provide realistic estimates of $\frac{d\varepsilon}{dt}$ (*Latynina and Karamaleeva1978, Varga,1984, Mentes1994, 1995*).

5. Conclusions.

The study of strain rates of great and medium seismic events shows, because the unrealistically high $\frac{d\varepsilon}{dt}$ values, that probably in case of their source zones the typical return period of characteristic earthquakes should be well above $\Delta t=250year$ (around $\Delta t=1000\ year$). For "giant" earthquakes ($M_W \geq 9.0$) (Table 3) the $\Delta t=250year$ return period seems to be satisfactory.

Presently the prediction of return periods is based on statistical analysis of regional earthquake catalogues. In case of improvement of strain measurement techniques the return periods can be obtained with the use of these geodetic techniques too. For this purpose the accuracy of GPS measurements should be increased or/and the local influences on strainmeter observations should be excluded more accurately.

Acknowledgements.

This paper was completed in the frame of the project supported by the Hungarian Scientific Research Found OTKA (Project: K60394).

References

Hanks T.C., Kanamori H., 1979,A moment magnitude scale , J.Geophys.Res., 84, B5, 2348-2350.

Huang Y.,Saleur H., Sammis C., Somette D.,1998,Precursors,aftershocks,critically and self organised critically. Europhysics Letters,41,43-48.

Kasahara K.,1981,Earthquake mechanics, Cambridge University Press

Kostrov B.V., 1974,Seismic moment and energy of earthquakes and seismic flow of rock. Izv. Acad. Sci USSR, Phys. Solid Earth,1,23-40.

Latynina L.A., Karamaleeva R.M., 1978, Deformographic measurements. Nauka, Moscow

Mentes Gy.,1994, Instruments for precise determination of horizontal deformations in the Pannonian basin, Acta Geod. Geoph. Hung.,29, 1-2, 161-177.

Mentes Gy., 1995, In-situ calibration of quartz tube extensometers, Marees Terrestres Bulletin d'Informations,121, 9070-9075.

Varga, P., 1984, Long-term variations recorded by extensometers. Journal of Geophysics, 55, 68-70.

Zsíros T., 2000,Seismicity and seismic risk of the Hungarian Basin: The Hungarian earthquake catalogue. Budapest, GGKI

The importance of instrument location on barometric pressure-induced noise

Holger Steffen*
Institute of Geological Sciences, FU Berlin
Malteserstr. 74-100, Haus D
D-12249 Berlin / Germany

Abstract

Barometric pressure-induced noise in records of broadband seismometers, strainmeters and tiltmeters is one of the major limiting factors in analyzing the data for studies of the Earth's interior structure and properties. Even the instruments at the Black Forest Observatory (BFO), installed in a depth of 170 m in a mountain behind an air-lock door, are influenced. We investigate the physical transfer mechanisms for pressure-induced noise with the help of a Finite Element model of the BFO, emphasizing the effect of pressure changes on the horizontal components at different locations inside a vault, e. g. on piers and in niches. The results show noise amplification factors of up to 37 within a distance of 1 m, and changes in the direction of the measured components. Each component is influenced differently, which makes it difficult to determine the best location to place. In addition, former results can be confirmed and suggestions for a correction can be drawn.

1 Introduction

The data of seismometers, strainmeters, and tiltmeters have been successfully used for studies of the Earth's interior. Unfortunately, extracting more detailed information is limited due to barometric pressure-induced noise, which is superimposed on the signals of interest, e. g. longperiod seismometer and strainmeter records (e. g. Sorrels, 1971; Sorrels et al., 1971; Beauduin et al., 1996; Zürn, 2002; Kroner et al., 2005; Zürn & Wielandt, 2006). The removal or likewise reduction of the disturbing signals is difficult, because the physical transfer mechanisms for pressure–induced noise especially in horizontal components are not well understood. Hence, in the last years many studies have been dedicated to barometric pressure-induced noise and its removal in

*E-Mail: hsteffen@zedat.fu-berlin.de

records of longperiod horizontal components (e. g. Fischer, 2002; Zürn, 2002; Zürn & Neumann, 2002; Kroner et al., 2005; Lambotte et al., 2006; Steffen et al., 2006; Zürn et al., 2006).

The Black Forest Observatory Schiltach (BFO; 48.33° N, 8.33° E; see Emter et al., 1999, for more information), located in a former mine, is characterised by a low noise level (Beauduin et al., 1996; Freybourger et al., 1997). Still, the instruments in 170 m depth behind an air-lock door (Fig.1) are affected by barometric-pressure changes, which implies the existence of transfer mechanisms related to the local setting. These mechanisms can be studied using the Finite Element (FE) approach. Thus, a FE model of the BFO is developed, including the main topographic structures and the gallery, and allowing the investigation of different loading scenarios. A detailed description of the first results can be found in Steffen et al. (2006). These results do not include the effects on different locations inside a vault, which will be the aim of this paper.

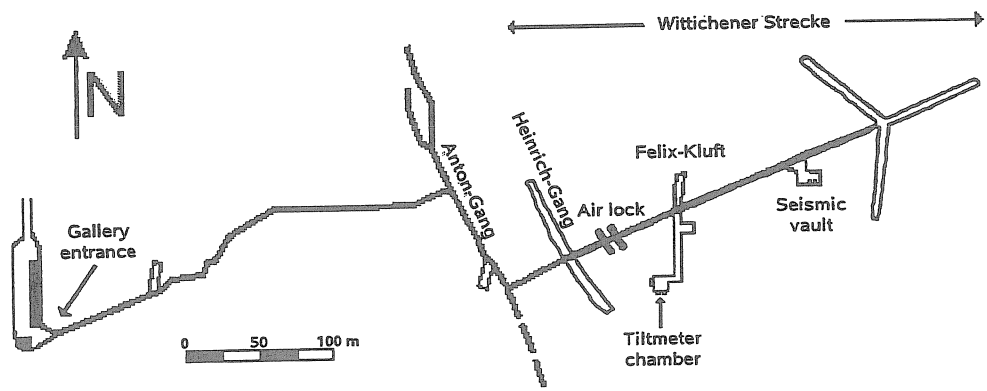

Figure 1: Sketch of the BFO. The "Felix-Kluft" with the tiltmeter chamber and the seismic vault with the long–period STS–1 seismometer can be found along the Wittichener Strecke behind the air lock.

2 Finite Element Modelling

The BFO model with its dimension is shown in Figure 2a. It is based on the model "litho" from Steffen et al. (2006) and includes new features: the "Felix-Kluft" with the tiltmeter chamber and piers in the seismic vault (Figs. 1 and 2b). The "Felix-Kluft", a smaller cavity than the "Heinrich-Gang", is located around 90 m west of the seismic vault. At its southwestern end the tiltmeter chamber can be found. Here, three niches are modelled, two in the southern and one in the western wall (Fig. 3b). The seismic vault is revised including three concrete piers of 1 m width, one at the northern wall with a height of 70 cm and a length of 5 m and two at the southern wall with a height

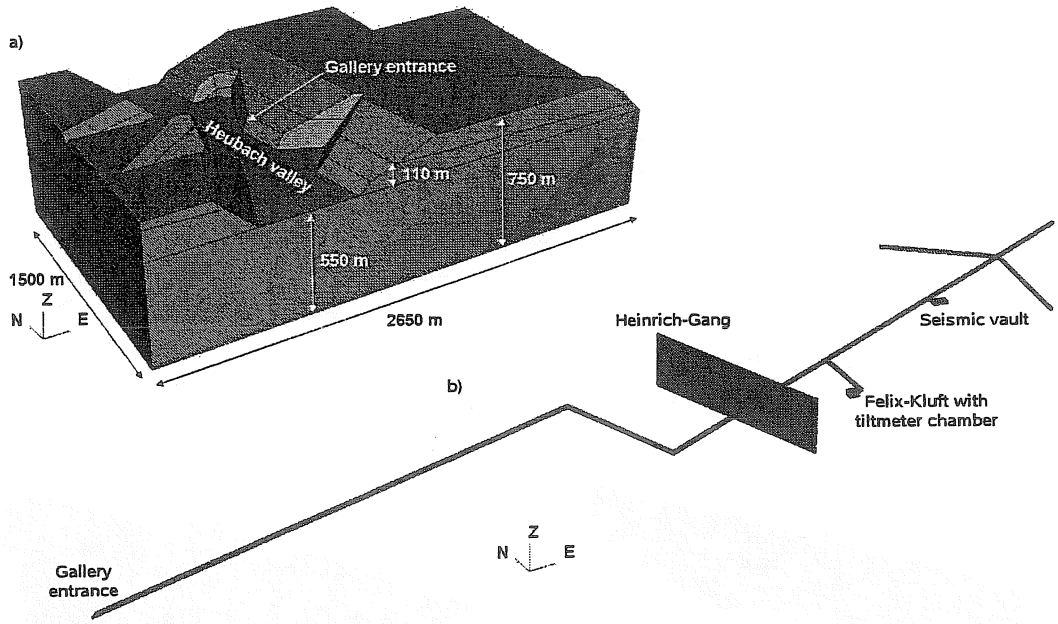

Figure 2: a) Perspective view of the BFO FE model "litho" (Steffen et al., 2006) from the southwest. b) Perspective view of the modelled gallery from the southwest.

of 25 cm and a length of 1.44 m, respectively (Fig. 3a). Between the southern piers a gap of 5 cm exists, allowing to study the tidal effects (Zürn et al., 1991).

The model is meshed with 165 000 elements (hexa– and tetrahedra), resulting in interior resolution of 0.12 cm side length in the gallery and the included cavities, and outside resolution at the top of 100 m. The model is parameterised with properties of granite and sandstone (for values see Steffen et al., 2006) for which a linear, elastic rheology is used. The gallery interior as well as the cavities are parameterised as air.

Three principle load cases are studied:

1. a uniform barometric pressure load on the model surface (valleys and mountains),
2. dynamic pressure acting on the eastern hill flank simulating wind-induced effects, and
3. the passage of pressure fronts.

Since an elastic rheology is used, the effects can be scaled and superimposed. From the loading scenarios, resulting tilts are calculated directly from nodes closest to the locations of the instruments. Special nodes were set directly at the required positions.

3 Results

Figures 4 and 5 summarise the results for the tilt induced from different load cases at 12 different locations. Four points are selected in the middle of the northern pier in the seismic vault, reflecting reasonable instrument positions. The distance in between is 1 m. They are numbered in ascending order from W to E, starting with P1 (Fig. 3a). On the southern piers also four points are chosen, two on each pier in the center with a distance in between of 48 cm. As for the northern wall, they are numbered from W to E but starting with P5. In the tiltmeter chamber two points (P9 and P10, P9 north of P10) are taken for the tilt calculation in the western niche (Fig. 3b). In the southern niches one point is selected within each niche. P11 is in the southwestern niche, P12 in the southeastern.

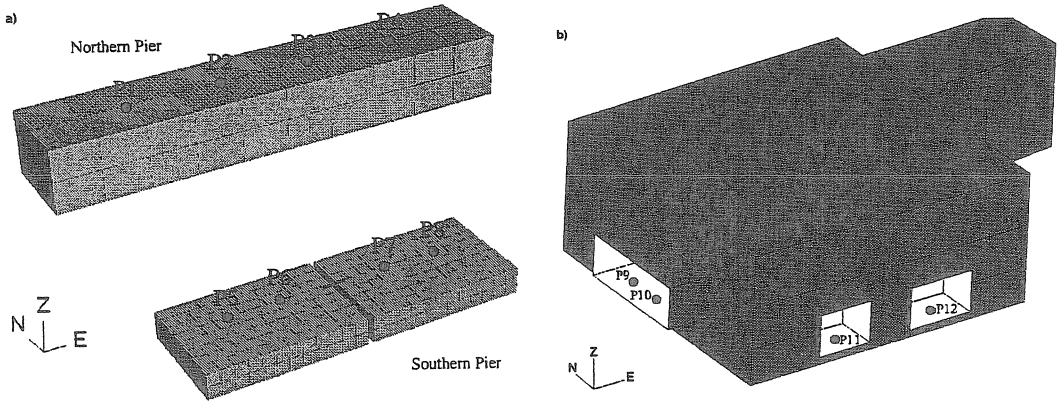

Figure 3: a) Perspective view of the piers in the seismic vaults from the southwest. b) Perspective view of the tiltmeter chamber with its niches from the southwest.

3.1 Uniform pressure and wind

Northern pier. On the northern pier for point P1 the uniform pressure load induces a tilt to E of more than 2 nrad/hPa and a tilt to N of about 1 nrad/hPa. For the other points on this pier the effect in the EW-component is reduced by a factor of up to 37 and reverse directed. In contrast to this, the NS–component only shows slight differences (around 7%) between all four points. The wind–induced effect in the EW–directions is directed westwards, where the source of pressure can be found. Surprisingly, a behaviour as for the uniform-pressure load cannot be found. In this case, the effect is around -0.2 nrad/hPa. Compared to the results of the uniform pressure, for the NS–component a reduction by a factor of 50 can be determined and the direction has changed. Thus, compared to the uniform pressure-load effect the influence of wind on the northern pier is negligible.

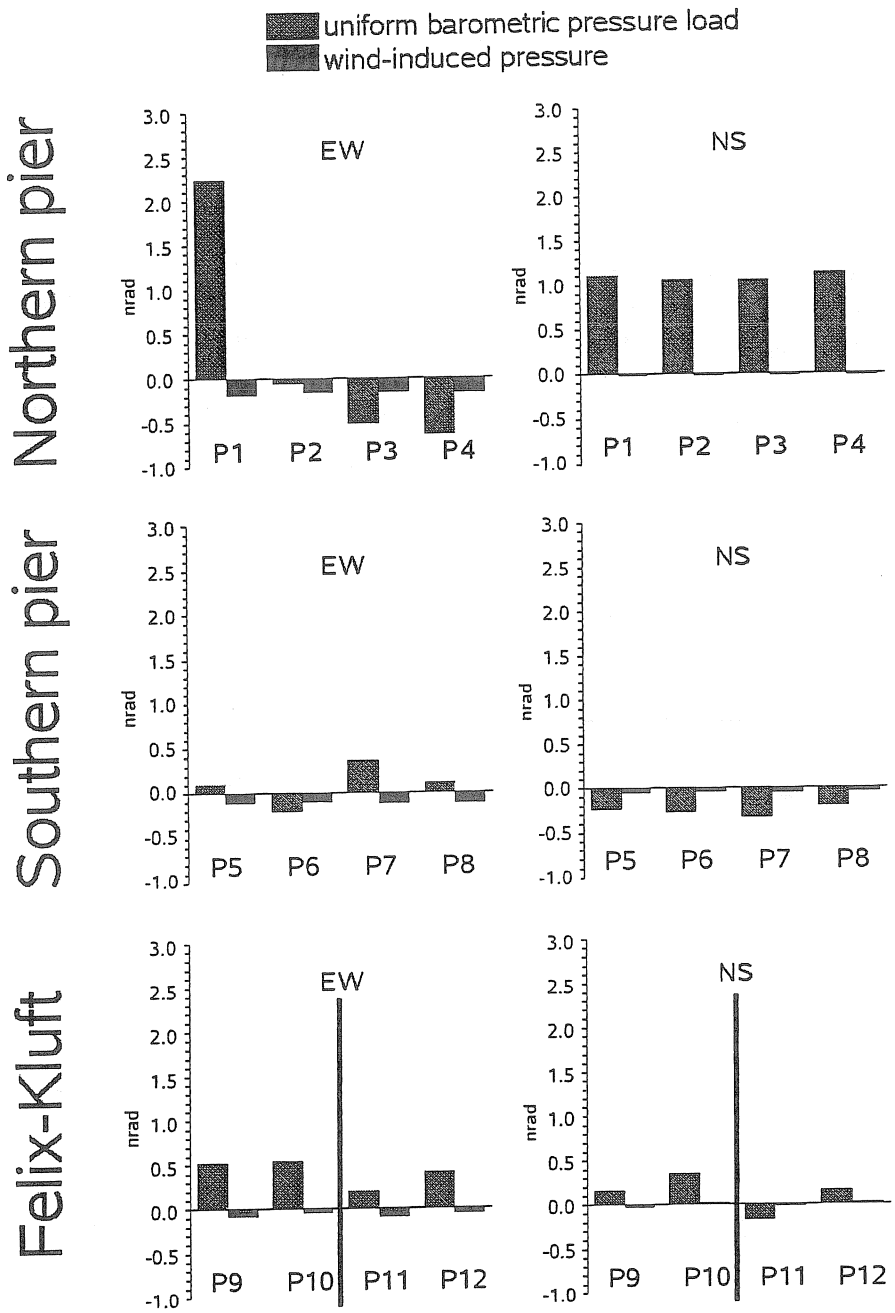

Figure 4: Tilts obtained for uniform and wind–induced pressure load normalised to 1 hPa for different locations. Top: northern pier in the seismic vault. Middle: southern piers in the seismic vault. Bottom: Niches in the Felix-Kluft. Tilt eastward, northward positive.

Southern piers. In general, the averaged tilt effects on the southern piers are smaller than the tilt effects on the northern pier, e. g. for the EW–component and the wind case, the tilt is decreased by a third. However, a comparison has to be done carefully as there are two smaller piers on the southern wall. In the uniform pressure-load case, the effects in the EW–component at P5 and P6 are reverse directed within a distance of 48 cm. For P7 and P8 a tilt eastward yields with a 3 times larger effect for P7. In contrast to the uniform pressure load, the wind affects each point with a tilt westwards of around 0.1 nrad/hPa. In the NS–component uniform pressure and wind load lead to tilts to S with nearly identically values of around 0.25 nrad/hPa and 0.05 nrad/hPa, respectively. The largest difference can be found between P7 and P8 with around 0.1 nrad/hPa.

Niches in the Felix-Kluft. The tilt for a uniform pressure load in the western niche (P9 and P10) of the tiltmeter chamber yields in a direction to E and N, while the wind induces tilts to W for both points, S for P9 and N for P10. The values are comparable with the ones from the southern pier in the seismic vault. The tilt calculated for the southern niches shows for the uniform pressure load a tilt to E in both niches. For the NS–component reverse tilts are resolved. The wind–induced effects are smaller and for the EW–component directed to W. The NS–component shows the same direction as for the uniform pressure load.

Generally, the wind-induced effects are directed to W, where the pressure is applied and are smaller than effects induced by uniform pressure. In the NS–component a tilt to S with values around and much less than 0.1 nrad/hPa is found, except for two points in the Felix-Kluft, but this might be due to local cavity effects in the niches.

3.2 Passing pressure fronts

Fig. 5 shows the tilt effects at different locations for a passing pressure front from W to E. Significant effects in both components can be found, strongly dependent on the direction of the pressure front. In the EW–component, directed in moving direction of the front, one can clearly see two peaks at all locations. The first peak is obtained when the front reaches the gallery area and is directed to W, to the source of pressure. The second peak is directed to E and confirms the tilting to the source of pressure, as in this case the end of the pressure front is above the gallery area. The tilt amplitudes of the first and second peak are different, which is caused by the topography of the mountain. This confirms earlier findings of Kroner et al. (2005) for Moxa. In the NS–component for the seismic vault a perfect example for the cavity effect can be seen (Fig. 6). On the northern pier a tilt northwards for all points and on the southern pier a tilt southwards for all points can be established. The load on the top decreases the vertical distance, which in turn leads to an increase of the NS–distance. As the piers are connected to the walls, they dip into the direction where the wall is located. In the tiltmeter chamber of the Felix-Kluft this behaviour is not observed, which is due to the more complicated structure of the chamber with three niches. In addition, the chamber is closer to the large Heinrich-Gang, which strongly influences the tilt (Steffen et al., 2006).

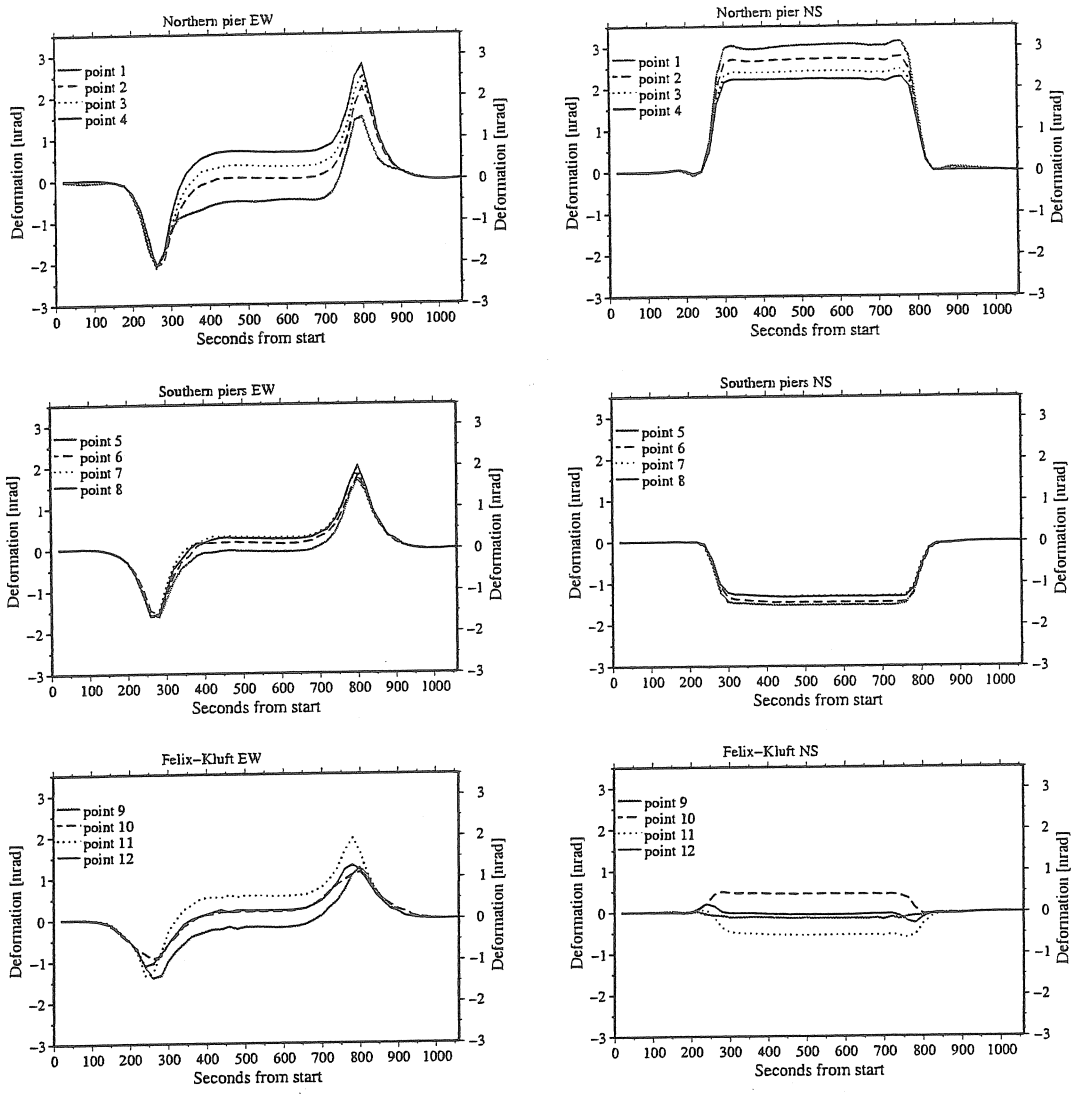

Figure 5: Tilts obtained for the traverse in time of a pressure area normalised to 1 hPa for different locations. The front is moving over the model having a velocity of 5 m/s and the model length of 2650 m. The model is loaded until the uniform pressure case is reached and afterwards unloaded. Thus, the pressure front has to cover a distance of 5300 m in 1060 s. Top: northern pier in the seismic vault. Middle: southern piers in the seismic vault. Bottom: Niches in Felix-Kluft. Tilt eastward, northward positive.

Northern pier. In the EW–component two interesting results can be found. First, the amplitudes for the first peak (tilt to W) for all points are nearly the same, while for the second peak (tilt to E) differences of more than 1 nrad/hPa result. Second, the smallest effects can be obtained for P2 and P3 when the gallery area is loaded as for the uniform pressure load. In the NS-component the difference of 1 nrad/hPa yields

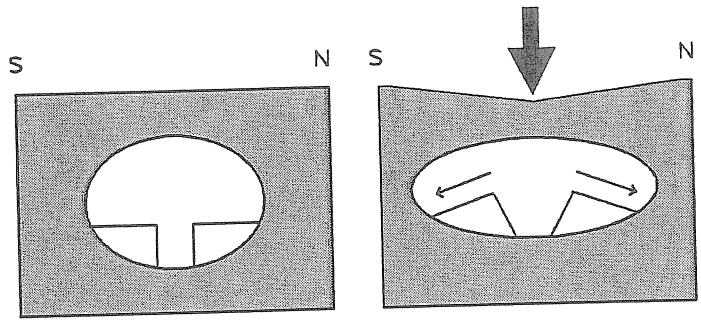

Figure 6: Sketch of the cavity effect in the seismic vault.

again, but all points are influenced by a constant value over a large load period. The difference in the amplitude between the peaks is a result of the topography, while the difference between the tilt of the points is due to the location on the pier.

Southern piers. In both components all points show nearly the same tilting. Compared to the northern pier, the amplitudes in both components are smaller with up to 1 nrad/hPa. In the EW–component, the amplitudes of the first peak are smaller by around 0.5 nrad/hPa than the amplitudes of the second peak, which is as mentioned before due to the topography. In the case of a pressure front, the instrument's position on the southern piers seems to be negligible. This might be due to the smaller height compared to the northern pier and/or the gap between the piers.

Niches in the Felix-Kluft. At first, the effects in western niche will be discussed. The EW–component for both points shows the already discussed tilting over time dependent on the pressure front. Interestingly, P9 is more affected with larger tilts in the first peak and in the time of continous load over the gallery. In the NS–component P9 is slightly influenced, while P10 is more affected with a tilt northwards. The largest effects in the EW–component of all points in the tiltmeter chamber can be found for P11 in the southwestern niche. Point P12 in the southeastern niche shows effects like P10. A tilt southwards can be observed for P11 in the NS–component. In contrast to this, only small tilts with eye-catching peaks can be established for P12. They behave like the EW–component reverse directed arising from the geometry of the chamber and the niches.

4 Conclusions

A FE model was used in this work to understand barometric pressure-induced signals in horizontal seismometer and tiltmeter records. Here, the influence of an uniform pressure load, the effect of wind–induced pressure and the influence by a passage of a pressure front were investigated and compared for different instrument sites at the BFO. Significant tilts affecting the records can be found for all load cases. We have shown that the location of an instrument is of importance. Resulting effects at the

BFO can differ in the direction and the amplitude within less than 50 cm. Furthermore, differences of up to a factor of 37 within 1 m distance are found. The biggest effects can be found on the northern pier in the seismic vault. Wind–induced pressure applied in the valley west of the observatory leads to effects with bigger magnitudes in EW–component, directed westwards to the source of the pressure, while the NS–component, which is directed perpendicular to the pressure source, shows only small effects. It is also shown that tilt effects are dependent on the direction of a passing barometric pressure event, which confirms earlier findings from Kroner et al. (2005) for Moxa.

Steffen et al. (2006) suggested three important conclusions for a correction. Regarding the results of Kroner et al. (2005), Steffen et al. (2006) and this work one contribution to point 3 has to be added. Thus, for a correction the three important conclusions are:

1. Each observatory requires a correction for barometric pressure effects adapted to its local conditions.
2. Each component requires its own correction.
3. A barometric pressure correction should take into account at least contributions by
   - a uniform, constant pressure load, and
   - wind-related pressure on the flanks of the observatory surroundings, and
   - passing pressure fronts.

Acknowledgments

The author wants to thank Walter Zürn, Corinna Kroner, Thomas Jahr, Sonja Kuhlmann and Kasper D. Fischer for many fruitful discussions. Georg Kaufmann is thanked for helpful comments on an earlier version of this paper. The FE modelling is carried out with the software ABAQUS.

References

Beauduin, R., Lognonne, P., Montagner, J. – P., Cacho, S., Karczewski, J. F. & Morand, M. 1996. The effects of the atmospheric pressure changes on seismic signals or how to improve the quality of a station. *BSSA* **86**, pp. 1760–1769.

Emter, D., Wenzel, H.-G. & Zürn, W. 1999. Das Observatorium Schiltach. *Mittlg. d. DGG* 3/1999: pp. 2-15.

Fischer, K. D. 2002. Sources and transfer mechanism of seismic noise: Preliminary results from FEM models. *Bull. d'Inf. Marees Terr.* **137**, 10881–10886.

Freybourger, M., Hinderer, J. & Trampert, J. 1997. Comparative study of superconducting gravimeters and broadband seismometers STS–1/Z in seismic and subseismic frequency bands. *Phys. Earth planet. Inter.* **101**: pp. 203-217.

Kroner, C., Jahr, Th., Kuhlmann, S. & Fischer, K. D. 2005. Pressure–induced noise on horizontal seismometer and strainmeter records evaluated by finite element modelling. *Geophys. J. Int.* **161**: pp. 167–178, doi:10.1111/j.1365-246X.2005.02576.x.

Lambotte, S., Rivera, L., & Hinderer, J. 2006. Vertical and horizontal seismometric observations of tides. *J. Geodyn.* 41(1-3), pp. 39–58.

Sorrels, G. G. 1971. A preliminary investigation into the relationship between long–period seismic noise and local fluctuations in the atmospheric pressure field. *Geophys. J. R. Astr. Soc.* **26**, pp. 71–82.

Sorrels, G. G., McDonald, J. A., Der, Z. A. & Herrin, E. 1971. Earth motion caused by local atmospheric pressure changes. *Geophys. J. R. Astr. Soc.* **26**, pp. 83–98.

Steffen, H., Kuhlmann, S., Jahr, Th. & Kroner, C. 2006. Numerical modelling of the barometric pressure-induced noise in horizontal components for the observatories Moxa and Schiltach. *J. Geodyn.* **41**, pp. 242–252, doi:10.1016/j.jog.2005.08.011.

Zürn, W. 2002. Simplistic models of vertical noise above 0.1 mHz derived from local barometric pressure. *Bull. d'Inf. Mareés Terr.* **137**, pp. 10867–10874.

Zürn, W. & Neumann, U. 2002. Simplistic models of atmospheric signals in horizontal seismograms. *Bull. d'Inf. Marees Terr.* **137**, pp. 10875–10880.

Zürn, W. & Wielandt, E. 2006. On the minimum of vertical seismic noise near 3 mHz. *Geophys. J. Int.*, submitted.

Zürn, W., Emter, D. & Otto, H. 1991. Ultra-short strainmeters: Tides are in the smallest cracks. *Bull. d'Inf. Mareés Terr.* **109**, pp. 7912–7921.

Zürn, W., Exss, J., Kroner, C., Jahr, T., Steffen, H. & Westerhaus, M. 2006. On the reduction of long period horizontal seismic noise using local barometric pressure. *Geophys. J. Int.*, in prep.

An attempt to improve the estimation accuracy of the atmospheric pressure effect

T. Sato, S. Rosat, Y. Tamura, and K. Matsumoto
National Astronomical Observatory of Japan

As a cooperative observation of GGP-Japan, we are conducting the SG (Superconducting Gravimeter) observation at Kamioka from October 22 in 2004. Kamioka site (36.423056N, 137.31083E, 350m in altitude) is located at about 80 km west of the Matsushiro SG site. One of the main scientific targets of this cooperative observation is to increase the reliability of the detection of such weak signals originating from the Earth's core as the core under tone, Slichiter triplets and the time variation in the tidal factor related to the free core resonance. As well known, a problem in the analysis of these weak signals is how we accurately estimate and correct the atmospheric pressure (A.P.) effects. Usually (or conventionally) the A.P. effects are corrected by using the local pressure data obtained at the observation site. However, for example, as shown in the works by Boy et al. (1998), Petrov & Boy (2004), it is not adequate only using the local pressure data to realize the correction at the accuracy better than 1 microGal.

To improve the estimation accuracy of the A.P. effect, we have done a test computation using a fine pressure data (spatial resolution: 10 km by 10 km), which are provided by JMA (Japan Meteorological Agency) for the region around Japanese (i.e. the area of 21.9N to 44.1N in latitude and 107.5E to 150.8E in longitude) so called as JMA-MANAL (Meso-scale Analysis) data. This assimilation model gives the time variations in the geopotential heights of the pressure levels of 20 in number (up-to 10 hPa) and the temperature at each height. Computation for the gravity effect, especially in its attraction part, is sensitive to the accuracy of the surface pressure and the 3-dimensional air mass distribution. We computed the vertical profile of air mass distribution at each grid point based on the equation of state of gas. To represent these as possible as precisely, we introduce two kinds of topographic digital elevation map (DEM). One is ETOPO2 of 2' in resolution and other is a DEM of 0.5' by 0.75' provided by Geographical Survey Institute of Japan. For the distant places more than about 6 deg in the angular distance from the observation site, we used a global air model called JMA GANAL (Global Analysis) model of the spatial resolution of 1.25 deg by 1.25 deg and of 23 layers (up-to the pressure level of 0.4 hPa). The time resolution is 6 hours for both the MANAL and GANAL data.

From the present study, we have confirmed the efficiency of using such fine pressure data as the JMA MANAL to improve the accuracy of the estimation of A.P. effects. From the comparison between the gravity residuals obtained by BAYTAP-analysis only taking into account the local pressure variations and those obtained by correcting the tidal components and the A.P. effects estimated using the meteorological data; we find, in the case of Kamioka, the correction only using the local pressure data does not well represent the effect of the pressure variations more than a few days in the period (i.e. the variations more than a few 100 km in the spatial scale). A remaining problem is how we include the frequency dependency of the IB response of the ocean into the convolution integral, as well as how we accurately interpolate the model data in the time-space domain, when we apply the correction values estimated using the model data to the analysis of high frequency phenomena shorter than 1 hour in period.